UCRL-ID-132246 Rev. 2

QA: N/A

Large Block Test Final Report

Wunan Lin
Stephen C. Blair

Dale Wilder, Steve Carlson, Jeff Wagoner, Laura DeLoach, George Danko (University of Nevada, Reno), Abelardo L. Ramirez, and Ken Lee

December 2001

U.S. Department of Energy
Lawrence Livermore National Laboratory

DISCLAIMER

This work was performed under the auspices of the U. S. Department of Energy by the University of California, Lawrence Livermore National Laboratory under Contract No. W-7405-Eng-48.

QUALITY ASSURANCE INFORMATION

This document was prepared under the Technical Work Plan for Nearfield Environment Thermal Analyses and Testing, TWP-NBS-TH-000001 REV 00 (CRWMS M&O 2000d). The Large Block Test was conducted under the control document of Activity Plan, AP-LBT-01 (Lin 1994). This technical report was prepared in accordance with procedure AP 3.11Q, REV 2. In accordance with the Activity Evaluation for Work Package #4301213NML, the Large Block Test Final Report is subject to the requirements of the Quality Assurance Requirements and Description Document (QARD). The specific requirements that apply to the report are described in OCRWM Administrative Procedure AP-3.11Q, Technical Products, and procedures referenced therein.

THIS PAGE INTENTIONALLY LEFT BLANK

ACKNOWLEDGMENTS

The authors gratefully acknowledge the assistance of Geoffrey S. Siemering, Marion Capobianco, Gina V. Kaiper and the Technical Productions Group of NAI in editing and preparing the manuscript, and of Paul Harding and Treva Carey for creation and preparation of the graphics. The following persons played important roles at various phases of the Large Block Test: Jim Blink, Tom Buscheck, Patricia Berge, Eric Carlberg, Richard Carlson, Joanne Horn, Annemarie Meike, Mark Owens, Ron Pletcher, Jeff Roberts, Dave Ruddle, Don Watwood, and Troy Williams. Bob Glass of Sandia National Laboratories conducted the fracture flow visualization test during the excavation phase of the LBT. Joe Wang of Lawrence Berkeley National Laboratory conducted pre-heating cross-hole air permeability measurements and tracer tests in the block. Work performed under the auspices of the U.S. Department of Energy by University of California, Lawrence Livermore National Laboratory, under contract No. W-7405-Eng-48.

THIS PAGE INTENTIONALLY LEFT BLANK

EXECUTIVE SUMMARY

The Large Block Test (LBT) was one of the thermal field tests conducted by the Yucca Mountain Site Characterization Project (YMP) to support confidence in the building and testing of the coupled process models used in analysis of the feasibility of Yucca Mountain as a potential repository site of high-level nuclear waste. The main objective of the LBT was to conduct a controlled, one-dimensionally-heated thermal test so that its results could be readily modeled. Through the comparison with model calculations, the results of the LBT help build confidence in the models of the coupled thermal-hydrological-mechanical-chemical (THMC) processes. The LBT was also used to test the use of optical multiple-point borehole extensometers and to evaluate the measurement of in-situ thermal conductivity and thermal diffusivity through the use of a Rapid Estimation of K and Alpha (REKA) probe. The LBT was also used to test the survivability and migration of local microbes in a heated partially saturated rock mass. The goal of the LBT was to heat the block from within so that a dryout zone was created and so that the thermal-hydrological (TH) processes associated with the heating, including moisture movement and condensate refluxing, could be monitored.

Pre-test scoping calculations indicated that a 3×3×4.5-m block of Topopah Spring tuff would be required to serve the purpose of the test. The pre-test scoping calculations also determined that a minimum bulk permeability of 10^{-15} m^2 and a minimum initial water saturation of about 50% would be required. Fracture mapping, air permeability measured by single-hole injection, and moisture content measured by neutron logging determined that the non-lithophysal Topopah Spring tuff outcrop at Fran Ridge, Nevada, would provide a test block suitable for the purpose.

After vertical boreholes were drilled and the boundary of a 3×3-m column was cut by a belt saw, neutron logging was used to confirm that the cutting did not change the moisture content in the block significantly. The block was retained horizontally by 10.2-cm-wide trucker straps and wooden blocking. The rock adjacent to the block was excavated using a hydraulic jackhammer. Some of the small blocks were selected, labeled, and stored for future tests in the laboratory. The fractures in the block were then mapped on the exposed five surfaces, and horizontal instrument boreholes were drilled. The rock core from each hole was preserved and managed by the Sample Management Facility. A video log of each hole was obtained, and the fractures in the holes were mapped from those video logs. Fracture characterization in the block was performed by combining results of fracture mapping on the block surfaces with analysis of fractures in the boreholes.

Instruments were installed in the boreholes and on the block surfaces. One electrical resistance heater was installed in each of the five heater holes. The vertical block surfaces were covered with 0.5-cm-thick Ultratemp insulation panels with embedded temperature monitors to determine heat flux out of the block. The trucker straps and wooden blocking were then reinstalled. A weatherproof cover was installed over the outside of the entire block assembly. During the test, additional insulation was blown in between the Ultratemp and outer cover, thereby filling voids between the trucker straps and wooden blocks. Thus, the block surface was insulated with three layers of materials with blown-in insulation between the wooden blocks. The first layer was the 5-cm-thick Ultratemp layer. Next, there was a 7.5-cm-thick layer of fiberglass. Finally the block was wrapped with a layer of Reflectix. Construction activities are detailed in Section 3.

The five heater holes formed a heater plane about 2.74 m from the top of the block. The power output from each heater was about 450 W.

Temperatures at the top of the block were maintained at about 60°C by circulating fluid through a heat exchanger. Heat loss from the sides was maintained by the insulation. Temperature was measured within the block in two vertical holes (TT1 and TT2), four horizontal holes from the north face (NT1–NT4), and three horizontal holes from the west face (WT1–WT3). In each of these holes, electrical resistance temperature devices (RTD) were used to measure temperatures every 20 cm. Temperatures at three locations in each of the five heater holes were measured by RTDs. The temperature holes were sealed with cement grout. The five heater holes were left open with a plug at the collar, so that the heaters could be replaced if necessary. The temperature on top of the block was measured by five RTDs mounted on an aluminum plate, and these measurements were used to control the heat exchanger to maintain the temperature at about 60°C on the top. On the vertical faces, the temperature was measured at 32 locations on the block surface and on both sides of the 1.2-cm-thick Ultratemp sheet insulation. The rock surface and Ultratemp surface temperatures were used to calculate the heat flux from the block.

Moisture content was measured along holes using neutron logging and in planes using electrical resistance tomography (ERT). There were 15 neutron holes: five vertical holes (TN1–TN5), six horizontal holes from the north face (NN1–NN6), and four horizontal holes from the west face (WN1–WN4). Each of the neutron holes were kept open with a Teflon liner. The annular space between the liner and the borehole wall was sealed with cement grout. ERT electrodes were mounted in the block and on the block surface such that two vertical and two horizontal imaging planes were formed. The two vertical planes dissected the block faces and intersected at the center of the block. The two horizontal ERT planes were located at 1.74 and 4.35 m from the block top, thus defining planes 1 m above and 1.61 m below the plane of the heaters.

Hydrological parameters (relative humidity, gas pressure, and temperature) were measured in four hydrological holes (one vertical [TH1], and three horizontal [NH1, WH1, and WH2]). Packers were used to seal the hydrological holes, and the sensors were mounted between the packers. The block deformation was monitored in boreholes and on the surface. Multiple-point borehole extensometers (MPBX), including an experimental optical extensometer, were used to monitor the block deformation in eight holes (two vertical ones [TM1, TM2] and six horizontal ones [NM1–NM3 and WM1–WM3]). Fracture gauges were used to monitor the deformation of specifically selected fractures on the block surface. A REKA probe was used to measure in-situ thermal conductivity and thermal diffusivity in three holes (TR1, WR1, and WR2).

The heaters were energized to their full power on February 28, 1997. The heating phase lasted more than one year, until March 10, 1998. The block was allowed to cool naturally without removing the insulation materials, from March 10, 1998, until the end of monitoring on September 30, 1998, when data acquisition ceased. Post-test drilling was conducted in 1999 to core selected portions of the block and to over-core one of the heater holes.

The discussion of temperature, thermal conductivity, and thermal diffusivity measurements is presented in Section 5. The greatest temperature measured in the block reached about 142°C at TT1–14. This RTD was about 5 cm below the heater plane. In general, a one-dimensional temperature distribution was achieved within the block. However, heterogeneity was evident. For

example, TT1–14 showed that the temperature rose through the boiling point of water without showing the evidence of boiling, but TT2–14 showed a significant effect of boiling/rapid evaporation on the temperature. This is probably due to the combination of edge effects (deviation from one-dimensional heating) and heterogeneous hydrologic properties. The measured temperatures in those two vertical temperature holes showed the effects of TH process. Two such events were recorded: one on June 13, 1997, and the other on September 2, 1997. In both events, many of the measured temperatures appear to have been affected by flowing water along the holes. The temperatures tended to converge to the boiling point of water and remained at that level for an extended period of time, followed by high-frequency fluctuations attributed to condensate refluxing. There was evidence that the September 2, 1997, event was triggered by a heavy rainstorm, but there was no clear evidence that the June 13, 1997, event was associated with rain. The temperature variations in those two events were sufficiently different to attribute the June 13, 1997, event to a sudden release of overheated water in the rock rather than to rainfall infiltration. In-situ thermal conductivity and thermal diffusivity, as measured by REKA probes, were consistent with the expected values for this rock, but no correlation between the thermal properties measured by a REKA probe and the TH processes indicated by the two TH events could be established. The measured temperatures in the block agreed well with that calculated by dual-permeability models using NUFT codes.

Section 6 presents the variation of the moisture content in the block as measured by neutron logging and ERT. Neutron logging provided accurate measurement of the moisture content along a borehole within a region of about 12 cm in radius around the borehole. ERT provided less accurate imaging of the moisture content but in cross sections of the entire block. Both measurements showed that a dry-out region about 1 m in thickness developed at the heater plane. As was the case with temperatures, the drying of the block was approximately one-dimensional, but deviation from the uniform one-dimensional drying was evident. The deviation was probably caused by the fractures. The rock in the dry-out zone was not totally dried. The neutron results showed residue moisture content of about 1% fraction volume. There was no significant re-wetting in the block during the cool-down phase. The moisture might have left the rock top as steam/vapor, drained through the bottom, and/or been held in pores in the condensate zone. The measured moisture content agreed well with that calculated by dual-permeability models using NUFT codes.

As presented in Section 7, borehole extensometers and fracture gauges were used to monitor the deformation of the block. The results showed that fractures had significant effect on the deformation. The upper two-thirds of the block deformed differently than the lower one-third, likely reflecting the lack of rigid lateral restraint. The discrete element model of the LBT more accurately predicts the deformation behavior than does the continuum model. Not all fractures were active; the deformation was controlled by a subset of 6–10 major fractures. A coefficient of thermal expansion value of 5.27×10^{-6}/°C is appropriate for the LBT. This is consistent with the value determined for the Single Heater Test and with preliminary analysis of the Drift-Scale Test data. The transient response of the deformation is correlated more closely with temperature of the heaters than with temperature at the measurement point. This indicates that a mechanism translating force at a distance is active. Fracture gauge monitoring showed that fractures moved in association with the major thermal-hydrological events that occurred in the LBT. As also indicated in Section 7, there was no change between the pre-heat and the post-test mechanical

properties. The assessment of the chemical process in the LBT depended on the comparison of the mineralogical composition of the pre-test cores and the post-test cores.

Section 8 shows that the mineralogical composition of the matrix of the block was not altered by the heating and the associated TH processes. This finding is consistent with that of the mechanical property, as shown in Section 7. There were no significant alterations in the minerals on the fracture surface either.

Section 9 presents the results of other measurements. Those include the observations in boreholes near the bottom of the block designated as observation holes (EO3, NO1, NO2, and WO5); measurements of relative humidity, temperature, and gas pressures in the packer holes (TH1, NH1, WH1, and WH2); and microbial survivability and migration. Observations conducted in the observation holes were considered scoping in nature and therefore should be treated as non-Q. The observations indicated that moisture moved downward from the heaters. The water left some discrete markers on the observation assemblies, but the marks were not sufficiently definitive to distinguish between fracture flow and condensation dripping. Microbe migration indicates that at least a portion of the water was from fracture flow. The gas pressure measurements did not produce consistent results. The temperature measured by Humicaps agreed well with that measured by RTDs. The variations in relative humidity measured by Humicaps were in agreement with the variation of moisture measured in the rock. None of those measurements registered the TH events shown by the temperature measurements by the RTDs. Local microbes were labeled to be double-drug-resistant and emplaced in the heater holes before the start of the heating. Samples collected in the observation holes, which were about 1.5 m below the heater plane, showed that the microbes had survived the heating and had migrated, by being transported by water flow fractures, at least to that distance.

Section 10 presents conclusions and summary of some specific findings of the LBT. The LBT met its objectives and provided adequate testing of coupled process models. The drying of the block and the movement of water by the heat agreed well with the conceptual model of one-dimensional heating in a partially saturated rock mass. The measured temperature and moisture content in the LBT agreed well with model calculations. The LBT showed that condensate can reflux under the idealized conditions imposed on the block, as predicted. The LBT also indicates that the condensate could penetrate the boiling zone. Under conditions represented by the block, it has not been determined whether this conclusion would apply to the potential repository, where high percolation flux events would be moderated by the non-welded tuff above and where a much larger zone of heated rock might be present. TH models identify this as a possibility. There was no significant rewetting during the cool-down phase. The LBT found that the effect of fractures on the THM process was significant. The test seemed have no effect on the matrix of the rock mass.

CONTENTS

Page

EXECUTIVE SUMMARY vii

ACRONYMS AND ABBREVIATIONS xxvii

1. INTRODUCTION 1–1

2. BACKGROUND 2–1

2.1 THE TESTING STRATEGY 2–1

2.2. TEST SCALES 2–2

3. TEST DESCRIPTION 3–1

3.1 OBJECTIVES OF THE LARGE-BLOCK TEST 3–1
3.1.1 Overall Objectives 3–1
3.1.2 Specific LBT Design and Implementation Objectives 3–2

3.2 CONFIGURATION OF THE LBT 3–4

3.3 INSTRUMENTATION, MONITORING AND CHARACTERIZATION 3–6
3.3.1 Installation of Instrumentation and Data Collection Systems 3–8

3.4 MEASUREMENTS 3–9
3.4.1 Thermal Monitoring 3–9
3.4.1.1 Temperature 3–9
3.4.1.2 In-situ Thermal Conductivity and Thermal Diffusivity 3–9
3.4.1.2.1 REKA Measurement and Evaluation Principles 3–9
3.4.1.2.2 The Measurement Arrangement 3–10
3.4.2 Hydrological Monitoring 3–10
3.4.3 Mechanical Monitoring 3–11
3.4.4 Microbial Monitoring 3–11
3.4.5 Assessment of Rock-Water Interaction 3–11
3.4.6 Other Monitoring 3–11

3.5 OVERVIEW OF CHRONOLOGICAL ACTIVITIES 3–12
3.5.1 Block Preparation and Pre-test Characterization 3–12
3.5.1.1 Site Selection 3–12
3.5.1.2 Block Preparation 3–12
3.5.1.3 Block Characterization 3–13
3.5.1.3.1 Laboratory-Determined Water Permeability of the Matrix 3–14
3.5.1.3.2 Moisture Retention Curves 3–15
3.5.1.3.3 The Porosity and Micro-Pore Structure 3–17
3.5.1.3.4 Visualization of Fracture Flow Versus Matrix Imbibition Using X-ray Radiography 3–17
3.5.2 Pre-Heat Thermal-Hydrologic Calculations 3–22
3.5.2.1 Homogeneous and Heterogeneous Cases 3–22
3.5.2.2 Thermal-Hydrologic Discrete Fracture Model 3–22
3.5.3 Pre-Heat Thermal-Mechanical Modeling 3–23
3.5.3.1 Description of Problem 3–23
3.5.3.2 Description of Models 3–23
3.5.3.2.1 FLAC Models 3–24
3.5.3.2.1.1 Grid Formulation 3–24
3.5.3.2.1.2 Initial and Boundary Conditions 3–25
3.5.3.2.1.3 Heaters 3–26

3.5.3.2.1.4 Rock Properties 3–26
3.5.3.2.2 ABAQUS™ Models 3–28
3.5.3.2.2.1 Time Steps 3–28
3.5.3.2.2.2 Grids, Nodes, and Elements 3–28
3.5.3.2.2.3 Material Properties 3–28
3.5.3.2.2.4 Initial and Boundary Conditions 3–29
3.5.3.2.2.5 Output 3–29
3.5.3.3 Results 3–29
3.5.3.3.1 FLAC Modeling Results 3–29
3.5.3.3.1.1 FLAC Thermal Results 3–30
3.5.3.3.1.2 FLAC Mechanical Results 3–31
3.5.3.3.2 ABAQUS™ Modeling Results 3–33
3.5.3.4 Discussion 3–33
3.5.3.4.1 Comparison of 2-D and 3-D Simulations 3–34
3.5.3.4.2 Conclusions 3–34
3.5.4 Post-test Characterization 3–35
3.5.4.1 Boreholes for Post-test Characterization 3–35

4. DOCUMENTATION AND ANALYSIS OF FRACTURES IN THE LARGE BLOCK TEST 4–1

5. THERMAL MEASUREMENTS 5–1

5.1 LOCATION OF INSTRUMENTS 5–1

5.2 BASELINE DATA COLLECTION AND HEATER TURN-ON 5–1

5.3 THE POWER OUTPUT FROM THE HEATERS 5–1

5.4 TEMPERATURE OBSERVATIONS 5–1
5.4.1 The Temperature History in the Block 5–2
5.4.2 The Spatial Temperature Distribution in the Block 5–3
5.4.3 Temperature as an Indicator of Thermal-Hydrological Events 5–3
5.4.4 Heat Flux on the Block Surface 5–5

5.5 THERMAL CONDUCTIVITY AND THERMAL DIFFUSIVITY 5–6

5.6 THERMAL-HYDROLOGICAL MODEL ANALYSES OF THE TEMPERATURE DATA 5–7
5.6.1 Numerical Model 5–7
5.6.2 Rock Property Data Sets 5–7
5.6.3 Drift-scale Simulation Results Versus Field Data 5–8
5.6.4 Summary 5–10

6. THERMAL HYDROLOGIC MEASUREMENTS AND ANALYSIS 6-1

6.1 THERMAL HYDROLOGIC MEASUREMENTS 6-1
6.1.1 Bulk Air Permeability and Flow Path Measurements 6-1
6.1.1.1 Pre-heating Permeability Measurements 6-1
6.1.1.1.1 LLNL Single Hole Permeability Test 6-1
6.1.1.1.2 Lawrence Berkeley National Laboratory Cross Hole 6-1
6.1.1.1.3 Lawrence Berkeley National Laboratory Trace Test 6-2
6.1.1.2 Post-Heating Air Permeability Measurement 6-2
6.1.2 Moisture Content Measurements 6-3
6.1.2.1 Electrical Resistance Tomography 6-3
6.1.2.1.1 ERT Methodology 6-3
6.1.2.1.2 Changes in Moisture Content 6-4
6.1.2.1.3 ERT Results 6-7
6.1.2.1.3.1 Horizontal Planes 6-8

6.1.2.1.3.2 Vertical Planes 6-9
6.1.2.1.4 Comparison of ERT with Other Data Sets 6-10
6.1.2.1.4.1 Comparison of ERT and Fracture Distribution 6-10
6.1.2.1.4.2 Comparison of ERT and Neutron Logs 6-10
6.1.2.1.5 Summary and Discussion 6-11
6.1.2.2 Neutron Logging 6-13
6.1.2.2.1 Pre-Cut and Post-Cut Moisture Contents 6-13
6.1.2.2.2 Pre-Heat Baseline Moisture Content 6-13
6.1.2.2.3. Heating Phase and Cooling Phase Moisture Content 6-14

6.2 THERMAL-HYDROLOGICAL ANALYSIS 6-17
6.2.1 In-Test Thermal-Hydrological Model 6-17
6.2.2 Post-Test Analysis 6-18
6.2.2.1 Purpose 6-18
6.2.2.2 Numerical Model 6-18
6.2.2.3 Rock Property Data Sets 6-18
6.2.2.4 Drift-scale Simulation Results Versus Field Data 6-19
6.2.2.6 Drift-scale Versus Mountain-scale Simulation Results 6-19
6.2.3 Summary 6-20

7. GEOMECHANICS OF THE LBT 7-1

7.1 DEFORMATION MEASUREMENTS 7-1
7.1.1 Introduction 7-1
7.1.1.1 The First 100 Days 7-1
7.1.1.2 Day 100 to Day 375 7-5
7.1.1.3 Cool-down 7-6
7.1.2 Large Block Thermal Expansion 7-7
7.1.2.1 Introduction 7-7
7.1.2.2 Data Reduction 7-7
7.1.2.3 Results 7-8
7.1.2.4 Discussion 7-9
7.1.3 Fracture Monitors 7-9
7.1.3.1 Deformation on Vertical Fractures 7-10
7.1.3.2 Deformation of Horizontal Fractures 7-12
7.1.3.3 Summary of Fracture Monitor Results 7-14
7.1.4 Discussion and Summary 7-14

7.2 SIMULATIONS 7-15
7.2.1 Distinct Element Analysis 7-15
7.2.1.1 Model Development 7-15
7.2.1.2 Boundary Conditions 7-15
7.2.1.3 Temperature Field and Calculation Times 7-16
7.2.1.4 Material Properties 7-16
7.2.1.5 Simulations 7-19
7.2.1.6 Results 7-19

7.3 POST-TEST ANALYSIS 7-22
7.3.1 Introduction 7-22
7.3.2 Methods 7-22
7.3.2.1 Sample Selection and Preparation 7-22
7.3.2.2. Ultrasonic Velocity Measurements 7-23
7.3.2.3 Compressive Strength Tests 7-24
7.3.3 Results 7-25
7.3.4 Discussion 7-27
7.3.5 Conclusions 7-28

8. ROCK-WATER INTERACTION IN THE LBT 8–1

8.1 INTRODUCTION 8–1
8.1.1 Fracture Mineralogy in the Tptp 8–1
8.1.2 Test-Induced Geochemical Processes in the Large Block 8–2

8.2 EVALUATION OF ALTERATION IN THE THERMAL TEST BLOCK 8–2
8.2.1 Large Block Mineralogical Characterization 8–2
8.2.2 Sample Selection and Preparation 8–3
8.2.2.1 SEM and EDX Sample Preparation 8–3
8.2.2.2 SEM and EDX Results 8–4
8.2.3 X-Ray Diffraction Analyses 8–5
8.2.3.1 Introduction 8–5
8.2.3.2 Measurements 8–5

9. OTHER MEASUREMENTS AND OBSERVATIONS 9-1

9.1 OBSERVATION HOLES 9-1
9.1.1 Construction of the Observation Assembly 9-1
9.1.2 Observations 9-2
9.1.3 Conclusions 9-4

9.2 RELATIVE HUMIDITY AND TEMPERATURE RESULTS FROM HYDROLOGY BOREHOLES 9-5

9.3 MICROBIAL SURVIVABILITY AND MIGRATION 9-7

10. LARGE BLOCK TEST CONCLUSION AND FINDINGS 10–1

10.1 GENERAL CONCLUSION 10–1

10.2 SPECIFIC FINDINGS 10–1

11. REFERENCES 11–1

APPENDIX A: BOREHOLE LISTING AND INSTRUMENT TYPE BY BLOCK SURFACE A-1

APPENDIX B: THE X-Y-Z COORDINATES (IN CM), WITH RESPECT TO THE SOUTHWESTERN CORNER ON TOP OF THE BLOCK, OF THE COLLAR (THE FIRST LINE) AND THE TOTAL DEPTH (THE SECOND LINE) OF ALL OF THE HOLES IN THE LBT. THE HOLE I.D. IN PARENTHESES IS THE CORRESPONDING INSTRUMENTATION HOLE AS LISTED IN APPENDIX A B-1

APPENDIX C: STRUCTURES DOCUMENTED IN THE BOREHOLE VIDEOS C-1

FIGURES

Page

Figure 2-1. Location of the Yucca Mountain Site 2–4
Figure 3-1. The Topopah Spring Tuff Block of the LBT 3–37
Figure 3-2. Fractures on the North Face of the Block 3–38
Figure 3-3. Fractures on the East Face of the Block 3–39
Figure 3-4. A Diagram Showing All Holes in the Block of the Large Block Test 3–40
Figure 3-5. Fractures on the South Face of the Block 3–41
Figure 3-6. Fractures on the West Face of the Block 3–42
Figure 3-7. Instrument Holes on Top of the Block 3–43
Figure 3-8. Instrument Holes on the North Face of the Block 3–44
Figure 3-9. Instrument Holes on the East Face of the Block 3–45
Figure 3-10. Instrument Holes on the West Face of the Block 3–46
Figure 3-11. Three REKA Probe Locations in the Large Heated Block 3–47
Figure 3-12. Measurement Flow Chart for One Probe 3–48
Figure 3-13. The MPBX Holes in the LBT 3–49
Figure 3-14. Initial Fracture Mapping at Fran Ridge 3–50
Figure 3-15. Excavation of Level Surface 3–51
Figure 3-16. Slots for Block Isolation 3–51
Figure 3-17. Partial Excavation of the Block 3–52
Figure 3-18. Drilling Rig Mounted on a Steel Platform to Drill Horizontal Boreholes 3–53
Figure 3-19. Percent Saturation as a Function of Suction Potential at 20°C for Nine Topopah Spring Tuff Samples During Wetting Phase 3–54
Figure 3-20. Percent Saturation as a Function of Suction Potential at 70°C for Six Topopah Spring Tuff Samples During Drying Phase 3–55
Figure 3-21. Percent Saturation as a Function of Suction Potential at 70°C for Three Topopah Spring Tuff Samples During Wetting Phase 3–56
Figure 3-22. Percent Saturation as a Function of Suction Potential at 20°C for Three Topopah Spring Tuff Samples During Drying Phase 3–57
Figure 3-23. Schematic Diagram Showing the Set-up of Using X-ray Radiography to Investigate Fracture Flow and Matrix Imbibition 3–58
Figure 3-24. Difference Images of Experiment 5 (a) and 6 (b) at 7.2 and 0.67 Hours Respectively After Flow Was Initiated 3–59
Figure 3-25. Schematic of Large Block Showing Locations of Fractures and Heater Boreholes 3–60
Figure 3-26. Predicted Temperature and Water Saturation Profiles Along a Vertical Line Through the Matrix at One-year Heating 3–61
Figure 3-27. Grid of the FLAC LBT Model 3–62
Figure 3-28. Temperature Contours in a Vertical Cross Section of the LBT After (a) 1 Day, (b) 10 Days, (c) 25 Days, (d) 50 Days, and (e) 75 Days of Heating, Calculated by FLAC Model 3–64
Figure 3-29. Temperature Profiles for (a) the Top and (b) Heater of the LBT, Calculated by FLAC Model 3–65
Figure 3-30. Temperature Near the Heater Horizon of the LBT Calculated by V-TOUGH Continuum Model (Lee 1995a) 3–66

Figure 3-31. Displacements and Stresses Predicted by the First FLAC Model at 75 Days of Heating, for (a) Horizontal, x, Displacement; (b) Vertical, y, Displacement; (c) σ_{xx} Stress; (d) σ_{yy} Stress; and (e) σ_{xy} Stress 3–68
Figure 3-32. Model Configuration of the Third FLAC Model with One Horizontal Fracture and One Vertical Fracture 3–69
Figure 3-33. Displacements and Stresses Predicted by the Third FLAC Model of the LBT at 75 Days of Heating, (a) Horizontal, x, Displacement; (b) Vertical, y, Displacement; (c) σ_{xx} Stress; (d) σ_{yy} Stress; and (e) σ_{xy} Stress. 3–71
Figure 3-34. The (a) σ_{xx} and (b) σ_{yy} Contours in the LBT Predicted by the Fourth FLAC Model at 75 Days of Heating 3–72
Figure 3-35. Temperature and Normal Stress Contours Predicted by ABAQUS Model at (a) 10, (b) 20, and (c) 60 Days of Heating 3–74
Figure 3-36. Displacements in the LBT Predicted by the ABAQUS Model at (a) 10, (b) 20, and (c) 60 Days of Heating 3–76
Figure 3-37. Post-test Coring Holes Drilled from the West Face of the Block 3–77
Figure 3-38. Post-test Coring Holes Drilled from the North Face of the Block 3–78
Figure 4-1. Mapped Surface Fractures on the Large Block 4–5
Figure 4-2. All Boreholes Drilled in the Large Block, Viewed at Various Angles 4–6
Figure 4-3. Equal-Area Diagram of Pole to the Major Fractures in the Large Block 4–7
Figure 4-4. 3-D Depiction of the Major Mappable Fractures Cutting the Large Block 4–8
Figure 4-5. Fracture System #1 Contains Three Fractures That Strike N50E and Dip 40–45° Northwest 4–9
Figure 4-6. Fracture System #2 Contains Two Fractures That Strike N30–40W and Dip 60–80° Northeast 4–10
Figure 4-7. Fracture System #3 Contains Six Subhorizontal Fractures 4–11
Figure 4-8. Fracture System #4 Contains 13 Mapped Fractures and Is the Dominant System in the Block 4–12
Figure 4-9. Fracture System #5 Contains Four Approximately Vertical Fractures That Strike East–West 4–13
Figure 4-10. Fracture System #6 Contains Two Mappable Fractures That Strike Northeast and Dip to the Southeast 4–14
Figure 4-11. Equal-area Net of Poles to the Major Fractures Mapped on Top of the Block 4–15
Figure 4-12. Equal-Area Contour Diagram of Poles to 90 Fractures Mapped in the Climax Stock Granite 4–16
Figure 4-13. Fractures Mapped at the Fran Ridge Site Prior to Construction of the LBT (Square) 4–17
Figure 4-14. Mapped Fractures on Top of the LBT 4–18
Figure 4-15. Mapped Fractures on the West Face of the LBT 4–19
Figure 4-16. Mapped Fractures on the South Face of the LBT 4–20
Figure 4-17. Mapped Fractures on the North Face of the LBT 4–21
Figure 4-18. Mapped Fractures on the East Face of the LBT 4–22
Figure 5-1. The Power Output of the Heater in EH1 as a Function of Time 5–11
Figure 5-2. The Power Output of the Heater in EH2 as a Function of Time 5–11
Figure 5-3. The Power Output of the Heater in EH3 as a Function of Time 5–12
Figure 5-4. The Power Output of the Heater in EH4 as a Function of Time 5–12
Figure 5-5. The Power Output of the Heater in EH5 as a Function of Time 5–13

Figure 5-6. Temperature at TT1-14 as a Function of Time 5–13
Figure 5-7. Temperature at TT2-14 as a Function of Time 5–14
Figure 5-8. Quarterly Temperature Snapshots in TT1 to Show the Spatial Temperature Variation 5–15
Figure 5-9. Quarterly Temperature Snapshots in TT2 to Show the Spatial Temperature Variation 5–16
Figure 5-10. Quarterly Temperature Snapshots in NT1 to Show the Spatial Temperature Variation 5–17
Figure 5-11. Quarterly Temperature Snapshots in NT2 5–18
Figure 5-12. Quarterly Temperature Snapshots in NT3 to Show the Spatial Temperature Variation 5–19
Figure 5-13. Quarterly Temperature Snapshots in NT4 to Show the Spatial Temperature Variation 5–20
Figure 5-14. Quarterly Temperature Snapshots in WT1 to Show the Spatial Temperature Variation 5–21
Figure 5-15. Quarterly Temperature Snapshots in WT2 to Show the Spatial Temperature Variation 5–22
Figure 5-16. Quarterly Temperature Snapshots in WT3 to Show the Spatial Temperature Variation 5–23
Figure 5-17. The Vertical Cross Section Along TT1 of the 3-D Temperature Field in the Block on March 10, 1998 5–24
Figure 5-18. The Temperature at TT1-7 to TT1-11, Showing the Effect of the TH event on June 13, 1997 (105.2 Day) 5–25
Figure 5-19. The Temperature at TT1-12 to TT1-17, Showing the Effect of the TH Event on June 13, 1997 (105.2 Day) 5–26
Figure 5-20. The Temperature at TT1-18 to TT1-23, Showing the Effect of the TH Event on June 13, 1997 (105.2 Day) 5–27
Figure 5-21. Temperature at TT1-24 to TT1-28, Showing the Effect of the TH Event on June 13, 1997 (105.2 Day) 5–28
Figure 5-22. The Temperature at TT1-7 to TT1-11 as a Function of Time, Showing the Effect of the TH Event on September 2, 1997 (186.5 Day) 5–29
Figure 5-23. The Temperature at TT1-12 to TT1-17 as a Function of Time, Showing the TH Event on September 2, 1997 (186.5 Day) 5–30
Figure 5-24. The Temperature at TT1-18 to TT1-23, Showing the Effect of the TH Event on September 2, 1997 (186.5 Day) 5–31
Figure 5-25. The Temperature at TT1-24 to TT1-28, Showing the Effect of the TH event on September 2, 1997 (186.5 Day) 5–32
Figure 5-26. The Heat Flux per Unit Area in Zone 1 (z = –3.2 to –4.42 m) of the Block as a Function of Time from February 18, 1998, to February 25, 1998 5–33
Figure 5-27. The Heat Flux per Unit Area in Zone 2 (z = –1.981 to –3.2 m) of the Block as a Function of Time from February 18, 1998, to February 25, 1998 5–34
Figure 5-28. The Heat Flux per Unit Area in Zone 3 (z = –0.762 to –1.981 m) of the Block as a Function of Time from February 18, 1998, to February 25, 1998 5–35
Figure 5-29. The Heat Flux per Unit Area in Zone 4 (z = 0 to –0.762 m) of the Block as a Function of Time from February 18, 1998, to February 25, 1998 5–36
Figure 5-30. Rock Thermal Conductivity, K [W/(mK)], Diffusivity, Alpha [m^2/s], and Temperature [^oC] with Time [Days] for the Horizontal REKA Probe 1 Installed 0.584 m Below the Large Block's Horizontal Heater Layer 5–37

Figure 5-31. Rock Thermal Conductivity, K [W/(mK)], Diffusivity, Alpha [m^2/s], and Temperature [°C] with Time [Days] for the Horizontal REKA Probe 2 Installed 0.889 m Below the Large Block's Horizontal Heater Layer 5–38
Figure 5-32. Rock Thermal Conductivity, K [W/(mK)], Diffusivity, Alpha [m^2/s], and Temperature [°C] with Time [Days] for the Horizontal REKA Probe 3 Installed 1.38 m Below the Large Block's Horizontal Heater Layer 5–39
Figure 5-33. The Measured Temperatures in the LBT in TT1 Compared with Model Calculation Using NUFT 5–40
Figure 5-34. Comparison of the Measured Temperature at TT1-14 and TT1-19 with the Model Calculation Using the Drift-Scale Property Set 5–41
Figure 5-35. Predicted Temperature Profiles Along Hole #TT1 of the LBT Using the DS and MS Property Sets, Compared with the Measured Temperature 5–42
Figure 6-1. Air Permeability Measured in a Single Hole Before Cutting (D) and After Cutting (B) the Block as a Function of Depth 6-21
Figure 6-2. Air Permeability Variations Along Five Heater Boreholes at the LBT Site 6-21
Figure 6-3. Air Permeability Variations Along Three Horizontal, Hydrologic, Monitoring Boreholes at the LBT Site 6-22
Figure 6-4. Tracer Breakthrough Curves from Heater Borehole Intervals to a Hydrologic, Monitoring Borehole WH1 at the LBT Site 6-22
Figure 6-5. Air Permeability Measured by Single-hole Injection Along Hole TH1 in the Block Before Heating (Cold) and During Heating (Hot) 6-23
Figure 6-6. Layout of ERT Electrodes for the Large Block Test 6-24
Figure 6-7. Changes in the Distribution of Moisture Content in Two Horizontal Image Planes 6-25
Figure 6-8. Changes in the Distribution of Moisture Content in Two Vertical Image Planes 6-26
Figure 6-9. Interpolated Temperature Isotherms (°C) Superimposed on ERT-Derived Images of Volumetric Water Change in the West-to-East Plane 6-27
Figure 6-10. Comparison of Neutron Log and ERT Measurements of Changes in Moisture Content 6-27
Figure 6-11. Pre-Cut and Post-Cut Water Saturation as a Function of Depth 6-28
Figure 6-12. The Baseline Moisture Content Measured in Hole TN1 6-29
Figure 6-13. The Baseline Moisture Measured in Hole TN2 6-30
Figure 6-14. The Baseline Moisture Content Measured in Hole TN3 6-31
Figure 6-15. The Baseline Moisture Content Measured in Hole TN4 6-32
Figure 6-16. The Baseline Moisture Content Measured in Hole TN1 6-33
Figure 6-17. The Baseline Moisture Content Measured in Hole NN1 6-34
Figure 6-18. The Baseline Moisture Content Measured in Hole NN2 6-35
Figure 6-19. The Baseline Moisture Content Measured in Hole NN3 6-36
Figure 6-20. The Baseline Moisture Content Measured in Hole NN4 6-37
Figure 6-21. The Baseline Moisture Content Measured in Hole NN5 6-38
Figure 6-22. The Baseline Moisture Content Measured in Hole NN6 6-39
Figure 6-23. The Baseline Moisture Content Measured in Hole WN1 6-40
Figure 6-24. The Baseline Moisture Content Measured in Hole WN2 6-41
Figure 6-25. The Baseline Moisture Content Measured in Hole WN3 6-42
Figure 6-26. The Baseline Moisture Content Measured in Hole WN4 as a Function of Depth from the West Face of the Block 6-43

Figure 6-27. Difference Fraction Volume Water in Hole TN1 from March 11, 1997, to June 11, 1997 6-44
Figure 6-28. Difference Fraction Volume Water, Between the In-heat and the Baseline, in Hole TN1 as a Function of Depth from Top of the Block, from June 8, 1997, to September 15, 1998. 6-45
Figure 6-29. Difference Fraction Volume Water, Between the In-heat and the Baseline, in Hole TN2 as a Function of Depth from Top of the Block, from March 11, 1997, to June 11, 1997 .6-46
Figure 6-30. Difference Fraction Volume Water, Between the In-heat and the Baseline, in Hole TN2 as a Function of Depth from Top of the Block, from July 8, 1997, to September 15, 1998 6-47
Figure 6-31. Difference Fraction Volume Water, Between the In-heat and the Baseline, in Hole TN3 as a Function of Depth from Top of the Block, from March 11, 1997, to June 11, 1997 .6-48
Figure 6-32. Difference Fraction Volume Water, Between the In-heat and the Baseline, in Hole TN3 as a Function of Depth from Top of the Block, from July 8, 1997, to September 15, 1998 6-49
Figure 6-33. Difference Fraction Volume Water, Between the In-heat and the Baseline, in Hole TN4 as a Function of Depth from Top of the Block, from March 11, 1997, to June 11, 1997 .6-50
Figure 6-34. Difference Fraction Volume Water, Between the In-heat and the Baseline, in Hole TN4 as a Function of Depth from Top of the Block, from July 8, 1997, to September 15, 1998 6-51
Figure 6-35. Difference Fraction Volume Water, Between the In-heat and the Baseline, in Hole TN5 as a Function of Depth from Top of the Block, from March 11, 1997 to June 11, 1997 ..6-52
Figure 6-36. Difference Fraction Volume Water, Between the In-heat and the Baseline, in Hole TN5 as a Function of Depth from Top of the Block, from July 8, 1997, to September 15, 1998 6-53
Figure 6-37. Difference Fraction Volume Water, Between the In-heat and the Baseline, in Hole NN1 as a Function of Depth from the North Face of the Block, from March 11, 1997, to July 8, 1997 6-54
Figure 6-38. Difference Fraction Volume Water, Between the In-heat and the Baseline, in Hole NN1 as a Function of Depth from the North Face of the Block, from July 22, 1997, September 15, 1998 6-55
Figure 6-39. Difference Fraction Volume Water, Between the In-heat and the Baseline, in Hole NN2 as a Function of Depth from the North Face of the Block, from March 11, 1997, to July 8, 1997 6-56
Figure 6-40. Difference Fraction Volume Water, Between the In-heat and the Baseline, in Hole NN2 as a Function of Depth from the North Face of the Block, from July 22, 1997, to September 15, 1998 6-57
Figure 6-41. Difference Fraction Volume Water, Between the In-heat and the Baseline, in Hole NN3 as a Function of Depth from the North Face of the Block, from March 11, 1997, to July 8, 1997 6-58
Figure 6-42. Difference Fraction Volume Water, Between the In-heat and the Baseline, in Hole NN3 as a Function of Depth from the North Face of the Block, from November 6, 1997, to September 15, 1998 6-59
Figure 6-43. Difference Fraction Volume Water, Between the In-heat and the Baseline, in Hole NN4 as a Function of Depth from the North Face of the Block, from March 11, 1997, to July 8, 1997 6-60

Figure 6-44. Difference Fraction Volume Water, Between the In-heat and the Baseline, in Hole NN4 as a Function of Depth from the North Face of the Block, from July 22, 1997, to September 15, 1998 6-61
Figure 6-45. Difference Fraction Volume Water, Between the In-heat and the Baseline, in Hole NN5 as a Function of Depth from the North Face of the Block, from March 11, 1997, to July 8, 1997 6-62
Figure 6-46. Difference Fraction Volume Water, Between the In-heat and the Baseline, in Hole NN5 as a Function of Depth from the North Face of the Block, from January 29, 1998, to September 15, 1998 6-63
Figure 6-47. Difference Fraction Volume Water, Between the In-test and the Baseline as a Function of Depth from the North face of the Block, in Hole NN6 from March 11, 1997, to November 6, 1997 6-64
Figure 6-48. Difference Fraction Volume Water, Between the In-heat and the Baseline, in Hole NN6 as a Function of Depth from the North Face of the Block, from January 29, 1998, to September 15, 1998 6-65
Figure 6-49. Difference Fraction Volume Water, Between the In-heat and the Baseline, in Hole WN1 as a Function of Depth from the West Face of the Block, from March 11, 1998, to July 8, 1997 6-66
Figure 6-50. Difference Fraction Volume Water, Between the In-heat and the Baseline, in Hole WN1 as a Function of Depth from the West Face of the Block, from January 22, 1998, to September 15, 1998 6-67
Figure 6-51. Difference Fraction Volume Water, Between the In-heat and the Baseline, in Hole WN2 as a Function of Depth from the West Face of the Block, from March 11, 1997, to July 8, 1997 6-68
Figure 6-52. Difference Fracture Volume Water, Between the In-heat and the Baseline, in Hole WN2 as a Function of Depth from the West Face of the Block, from January 22, 1998, to September 15, 1998 6-69
Figure 6-53. Difference Fraction Volume Water, Between the In-heat and the Baseline, in Hole WN3 as a Function of Depth from the West Face of the Block, from March 11, 1997, to July 8, 1997 6-70
Figure 6-54. Difference Fraction Volume Water, Between the In-heat and the Baseline, in Hole WN3 as a Function of Depth from the West Face of the Block, from November 5, 1997, to September 15, 1998 6-71
Figure 6-55. Difference Fraction Volume Water, Between the In-heat and the Baseline, in Hole WN4 as a Function of Depth from the West Face of the Block, from March 11, 1997, to July 8, 1997 6-72
Figure 6-56. Difference Fraction Volume Water, Between the In-heat and the Baseline, in Hole WN4 as a Function of Depth from the West Face of the Block, from January 29, 1998, to September 15, 1998 6-73
Figure 6-57. Pre-test Temperature and Liquid Saturation Calculated in Model Case A 6-74
Figure 6-58. The Moisture Content Measured by Neutron in Hole TN3 Compared with the Model Calculations Using DS Property Set 6-75
Figure 6-59. Comparison of Calculated Liquid Saturation of the LBT Along Hole TN3 Using MS Property Set and DS Property Set 6-76
Figure 7-1. Multiple-Point Borehole Extensometer (MPBX) 7-29
Figure 7-2. MPBX Borehole Locations, Viewed from the South Face 7-29

Figure 7-3. Extensometer NM-1 Collar and Invar Rod Installation 7-30
Figure 7-4. Invar Rod Corrosion 7-31
Figure 7-5. Horizontal Displacements During the First Two Weeks of the Large Block Test 7-32
Figure 7-6. Displacement Rates for the Horizontal Extensometers During the First 40 Days of the LBT 7-33
Figure 7-7. East-West Anchor Displacements During the First 100 Days for WM-1 7-34
Figure 7-8. North-South Anchor Displacements During the First 100 Days for NM-1 7-35
Figure 7-9. North-South Anchor Displacements During the First 100 Days for NM-2 7-36
Figure 7-10. East-West Anchor Displacements During the First 100 Days for WM-2 7-37
Figure 7-11. North-South Anchor Displacements During the First 100 Days for NM-3 7-38
Figure 7-12. Vertical Anchor Displacements During the First 100 Days for TM-1 7-39
Figure 7-13. Anchor 4 Strains for Each Extensometer During the First 100 Days 7-40
Figure 7-14. East-West Displacement for WM-1 Anchor 4 and Temperature at 4-m Depth 7-41
Figure 7-15. East-West Displacement for WM-2 Anchor 4 and Temperature at 1.2-m Depth 7-41
Figure 7-16. North-South Displacement for NM-3-m Anchor 4 and Temperature at 1.2-m Depth .. 7-42
Figure 7-17. WM-2 Anchor Displacements and Borehole TT1 Temperature Near the Heater Plane 7-43
Figure 7-18. WM-2 Anchor 4 Displacements and Temperatures at 1.2 m Depth Around Day 105 . 7-44
Figure 7-19. WM-2 and NM-3 Anchor Displacements and Borehole TT1 Temperature Near the Heater Plane 7-45
Figure 7-20. WM-1East-West Anchor Di 7-46
Figure 7-21. NM-1North-South Anchor Displacements During Cool Down 7-47
Figure 7-22. WM-2 East-West Anchor Displacements During Cool-Down 7-48
Figure 7-23. NM-3 North-South Anchor Displacements During Cool-Down 7-49
Figure 7-24. TM-1 Vertical Anchor Displacements During Cool-Down 7-50
Figure 7-25. Anchor 4 Strains During Cool-Down 7-51
Figure 7-26. Strain Histories for Horizontal Extensometers 7-52
Figure 7-27. Strains, Calculated from MPBX Displacements, Regressed Against Temperature Changes 7-53
Figure 7-28. Linear Coefficients of Thermal Expansion with Depth into the Large Block 7-54
Figure 7-29. Cutaway View of LBT Surface Fracture Monitors 7-55
Figure 7-30. Fracture Monitor Locations on the East Side of the Large Block 7-56
Figure 7-31. Fracture Monitor Locations on the North Side of the Large Block 7-57
Figure 7-32. Fracture Monitor Locations on the West Side of the Large Block 7-58
Figure 7-33. Fracture Monitor Locations on the South Side of the Large Block 7-59
Figure 7-34. Photo of LBT with Fracture Monitor Grooves 7-60
Figure 7-35. Photo of Installed Fracture Monitor 7-61
Figure 7-36. Fracture Aperture Data for All Vertical Fracture Monitors and Temperature Near the Heater Plane 7-62
Figure 7-37. Fracture Aperture Data Between Days 100 and 140 for All Vertical Fracture Monitors and Temperature Near the Heater Plane 7-63
Figure 7-38. Fracture Slip for All Vertical Fractures and Temperature Near the Heater Plane 7-64
Figure 7-39. Aperture Change for Vertical Fractures 7-65
Figure 7-40. Slip Along Vertical Fractures 7-66
Figure 7-41. Fracture Aperture Data for All Horizontal Fracture Monitors and Temperature Near the Heater Plane 7-67

Figure 7-42. Temperature and Fracture Aperture Data for All Horizontal Fracture Monitors Between Day 100 and Day 140 7-68
Figure 7-43. Fracture Slip for All Horizontal Fractures and Temperature Near the Heater Plane 7-69
Figure 7-44. Fracture Slip for All Horizontal Fractures and Temperature Near the Heater Plane, Day 100 to Day 140 7-70
Figure 7-45. Deformation Across Horizontal Fractures 7-71
Figure 7-46. Slip Along Horizontal Fractures 7-72
Figure 7-47. General Block Movement 7-73
Figure 7-48. Anchor 4 Strains for Each Extensometer During the First 100 Days 7-74
Figure 7-49. Fracture Aperture Data for All Vertical Fracture Monitors 7-75
Figure 7-50. Large Block Test TM Model Domains 7-76
Figure 7-51. TM1 Anchor 4 Displacements and Model Results for the First 100 Days 7-77
Figure 7-52. TM1 Anchor 4 Displacements and Model Results for the Cool-Down 7-78
Figure 7-53. NM1 Anchor 4 Displacements and Model Results for the First 100 Days 7-79
Figure 7-54. NM1 Anchor 4 Displacements and Model Results for the Cool-Down 7-80
Figure 7-55. WM1 Anchor 4 Displacements and Model Results for the First 100 Days 7-81
Figure 7-56. WM1 Anchor 4 Displacements and Model Results for the Cool-Down 7-82
Figure 7-57. NM2 Anchor 4 Displacements and Model Results for the First 100 Days 7-83
Figure 7-58. WM2 Anchor 4 Displacements and Model Results for the Entire Test 7-84
Figure 7-59. NM3 Anchor 4 Displacements and Model Results for the Entire Test 7-85
Figure 7-60. WM2 Anchor 4 Displacements, Heater Plane (TT1-14) and WM2-Level (TT1-22) Temperatures and Results of Models 3 and 4 for the First 100 Days 7-86
Figure 7-61. Post-Test Core Drilling Activities, Overview 7-87
Figure 7-62. Post-Test Core Drilling Activities, Detail 7-88
Figure 7-63. Representative Stress-Strain Plots for (a) Pre-test Core HC_076_61 and (b) Post-test Core OC_874B_01 7-89
Figure 7-64. Compressional Velocities for (a) Pre-test and (b) Post-test Specimens 7-90
Figure 7-65. Shear Velocities for (a) Pre-test and (b) Post-test Specimens 7-91
Figure 7-66. Compressive Strength for (a) Pre-test and (b) Post-test Specimens 7-92
Figure 7-67. Static Young's Modulus for (a) Pre-test and (b) Post-test Specimens 7-94
Figure 7-68. Uniaxial Compressive Strength for Topopah Spring Tuff 7-94
Figure 7-69. Static Young's Modulus for Topopah Spring Tuff 7-95
Figure 8-1. Sample SPC0039799: Pre-Test Fracture of a Crusty-Coating of Al, Mn-rich Composition. The Grain Appearance and Analysis (Figure 8-2) Are Consistent with the Layer-Structure Mn-oxides Lithiophorite. 8-7
Figure 8-2. EDX Spectrum Corresponding to Area Shown in Figure 8-1 (Presumably the Reported Mineral Is Lithiophorite, Where Li Is Too Light for EDX Detection) 8-8
Figure 8-3. Sample SPC0039806: Pre-test Fracture Sample Exhibits Well-developed Crystalline Morphology. The Blocky Crystals Are Consistent with Calcite. Small Rounded Mounds, Lighter in Color and Scattered Around the Bases of the Calcite Are Determined to Be Silica Polymorph (See Figures 8-5 and 8-6) 8-9
Figure 8-4. EDX Spectrum, Generally Corresponding to Area Photographed in Figure 8-3. The Spectrum Is Likely a Composite from Two Phases: a Calcium Carbonate and a Silica Polymorph 8-10

Figure 8-5. Sample SPC0039806: Pre-Test Fracture, Magnified View of Rounded Masses Similar to Those Shown in Figure 8-3 (Bases of Blocky Crystals). EDX Is Consistent with a Silica Polymorph 8-11
Figure 8-6. EDX of Rounded Nodular Crystal Mass. Spectrum Is That of an Sio_2 Phase 8-12
Figure 8-7. Sample SPC0039806: Strand Lying on the Surface of Other Minerals. The Morphology and Relative Chemistry Suggest a Clay Mineral 8-13
Figure 8-8. EDX Spectrum for Strand Shown in Figure 8-7, Possibly a Clay, Such as Smectite 8-14
Figure 8-9. Sample SPC0039799 Pre-Test Sample with Calcite Grain (EDX Not Shown) Showing Pronounced Dissolution 8-15
Figure 8-10. Sample SPC02015843 Post-Test Sample with Significant Dissolution of a K-Rich Feldspar (EDX Not Shown) 8-16
Figure 8-11. Sample SPC02015843 Post-Test Sample (Different Area Than Imaged in Figure 8-10): Chevron Features are Sub-Micron Sized, Appear to Be Further Evidence of Dissolution (Grain Not Identified by EDX) 8-17
Figure 8-12. Sample SPC02015679 Post-Test Sample: an Abundance of the Matted Fibrous Material Covers Surfaces of Different Grains, Appears to Have a Morphology and Chemistry Consistent with a Clay 8-18
Figure 8-13. Sample SPC039806 Pre-Test Sample: the Same Fibrous Mineral Is Observed Coating Minerals of Fracture Surfaces Before Thermal Testing 8-19
Figure 8-14. Sample SPC02015679 Post-Test Sample: Overview of Post-Test Mineral Surface Exhibits Several Minerals—the Fibrous Matted Mineral, the Spherical Silica Polymorphs, Possibly Ribbons of Pore-Bridging Illite 8-20
Figure 9-1. Temperature Measured by the Humicap in Hole NH-1 as a Function of Time 9-9
Figure 9-2. Relative Humidity Measured by the Humicap in Hole NH-1 as a Function of Time 9-10
Figure 9-3. Temperature Measured by the Humicap in Hole WH-2 as a Function of Time 9-11
Figure 9-4. Relative Humidity Measured by the Humicap in Hole WH-2 as a Function of Time 9-12
Figure 9-5. Temperature Measured by the Humicap in Hole WH-1 as a Function of Time 9-13
Figure 9-6. Relative Humidity Measured by the Humicap in Hole WH-1 as a Function of Time 9-14
Figure 9-7. Temperature Measured by the Humicap in the Third Zone of Hole TH-1 as a Function of Time 9-15
Figure 9-8. Relative Humidity Measured by the Humicap in the Third Zone of Hole TH-1 as a Function of Time 9-16

THIS PAGE INTENTIONALLY LEFT BLANK

TABLES

Table 1-1. LBT Data Tracking Numbers 1–1
Table 3-1. LBT Fracture Systems 3–5
Table 3-2. Borehole and Instrument Listing by Instrument Type 3–7
Table 3-3. Permeability Measurements on Intact Core Sample SPC00504573.4 3–15
Table 3-4. The Porosity of LBT Samples Determined by Gravimetric Method 3–18
Table 3-5. Pore Size Distribution of the LBT Samples Determined by Mercury Injection Porosimetry Method 3–19
Table 3-6. Sample Descriptions–Fracture Flow Versus Matrix Imbibition Test 3–19
Table 3-7. Rock Property Values Used for Modeling of the LBT 3–27
Table 3-8. The xyz Coordinates (with Respect to the Southwestern Corner on Top of the Block) of the Collar, and Other Characteristics of the Post-test Holes 3–36
Table 4-1. Number of Fractures Per Each Length Interval and the Percentage of Fractures Occurring in Each Interval 4–2
Table 4-2. All Major Fracture Planes That Have Been Modeled for the LBT 4–3
Table 5-1. The DS and MS Rock Properties and the Thermal Properties of the Insulation Material Used in the TH Modeling of the LBT. (Source: Table 7 of CRWMS M&O 2000c). 5–8
Table 5-2. RMSD and MD for Temperature Profile Along TT1 Using Drift-scale Data Set 5–9
Table 5-3. RMSD and MD for Temperature Profile Along TT1 Using Drift-scale and Mountain-scale Property Sets 5–10
Table 6-1. X-Y-Z Coordinates of the Collar of the Neutron Holes 6-15
Table 6-2. Hydraulic and Thermal Properties of Rock Units 6-18
Table 7-1. MPBX Extensometer Collar and Anchor Coordinates. The Origin of the Coordinates Is the Southwestern Corner on Top of the Block 7-2
Table 7-2. MPBX Orientations, Baseline Lengths, and Number of Anchors 7-2
Table 7-3. Interpolated Average Temperatures for Horizontal MPBX Extensometers 7-8
Table 7-4. Thermal Expansion Coefficients (CTE) and Fitting Statistics 7-9
Table 7-5. Maximum and Residual Fracture Slip and Aperture 7-12
Table 7-6. Input Parameters and Data Tracking Numbers 7-17
Table 7-7. Calculated or Assumed Model Parameters 7-17
Table 7-8. Summary of LBT TM Simulations 7-19
Table 7-9 Pre-test Specimen Densities, Velocities, and Dynamic Moduli 7-25
Table 7-10 Post-test Specimen Densities, Velocities, and Dynamic Moduli 7-25
Table 7-11 Pre-test Specimen Strain Rates and Static Mechanical Properties 7-26
Table 7-12. Post-test Specimen Strain Rates and Static Mechanical Properties 7-26
Table 8-1. Samples Selected for SEM Imaging and Analysis 8–4
Table 8-2. Qualitative Results for the 19 Solid Samples from the Large Block Test Resulting from Analyses using Jade Software Package. 8–6
Table 9-1, X-Y-Z Coordinates of the Collar, C, and Bottom, TD, of the Observation Holes of the LBT 9-1
Table 9-2. The Location of Humicap in the Hydrology Holes 9-5

THIS PAGE INTENTIONALLY LEFT BLANK

ACRONYMS AND ABBREVIATIONS

2-D	Two-dimensional
3-D	Three-dimensional
AMR	Analysis Model Report
ASTM	American Society for Testing and Materials
AZ	Altered Zone
CD	Compact Disk
CD-ROM	Compact Disk - Read Only Memory
CTE	Coefficient of Thermal Expansion
DAS	Data acquisition system
DOE	Department of Energy
DS	Drift-scale
DST	Drift Scale Test
DTN	Data tracking number
EBS	Engineered Barrier System
ECM	Equivalent continuum model
EDX	Energy Dispersive X-ray
ERT	Electrical resistance tomography
ESF	Exploratory Studies Facility
FLAC	Fast Lagrangian Analysis of Continua
FM	Fracture monitor
HHL	Horizontal heater layer
HP	Hewlett Packard
KI	Potassium iodide
LANL	Los Alamos National Laboratory
LBNL	Lawrence Berkeley National Laboratory
LBT	Large Block Test
LLNL	Lawrence Livermore National Laboratory
LVDT	Linear Variable Differential Transformer
MD	Mean difference
MPBX	Multiple point borehole extensometer
MS	Mountain-scale
NF	Near Field
NFE	Near Field Environment
NI	National Instruments
NIST	National Institute of Standards and Testing
OCRWMS	Office of Civilian Radioactive Waste Management System

PVC	Polyvinyl chloride
QA	Quality Assurance
REKA	Rapid Evaluation of K and Alpha
RH	Relative humidity
RIB	Reference Information Base
RMS	Root-mean-square
RMSD	Root-mean-squared difference
RTD	Resistance temperature device
RTV	Room temperature vulcanized rubber
SEM	Scanning Electron Microscope
SHT	Single Heater Test
SMF	Sample Management Facility
TC	Thermal-chemical
TCO	Test Coordination Office
TDMS	Technical Data Management System
TH	Thermal-hydrological
THC	Thermal-hydrological-chemical
THM	Thermal-hydrological-mechanical
THMC	Thermal-hydrological-mechanical-chemical
TM	Thermal-mechanical
TSPA	Total System Performance Assessment
Tptp	Topapah Spring tuff
Tptpmn	Topopah Spring tuff, middle nonlithophysical
TSw2	Topopah Spring tuff thermal-mechanical unit
USGS	United States Geological Survey
UZ	Unsaturated Zone
W	Watt
WF	Waste Form
WP	Waste package
XRD	X-ray diffraction
YM	Yucca Mountain
YMP	Yucca Mountain Site Characterization Program

1. INTRODUCTION

This report documents the Large-Block Test (LBT) conducted at Fran Ridge near Yucca Mountain, Nevada. The LBT was a thermal test conducted on an exposed block of middle non-lithophysal Topopah Spring tuff (Tptpmn) and was designed to assist in understanding the thermal-hydrological-mechanical-chemical (THMC) processes associated with heating and then cooling a partially saturated fractured rock mass. The LBT was unique in that it was a large ($3 \times 3 \times 4.5$ m) block with top and sides exposed. Because the block was exposed at the surface, boundary conditions on five of the six sides of the block were relatively well known and controlled, making this test both easier to model and easier to monitor. This report presents a detailed description of the test as well as analyses of the data and conclusions drawn from the test. The rock block that was tested during the LBT was exposed by excavation and removal of the surrounding rock. The block was characterized and instrumented, and the sides were sealed and insulated to inhibit moisture and heat loss. Temperature on the top of the block was also controlled. The block was heated for 13 months, during which time temperature, moisture distribution, and deformation were monitored. After the test was completed and the block cooled down, a series of boreholes were drilled, and one of the heater holes was over-cored to collect samples for post-test characterization of mineralogy and mechanical properties.

Section 2 provides background on the test. Section 3 lists the test objectives and describes the block site, the site configuration, and measurements made during the test. Section 3 also presents a chronology of events associated with the LBT, characterization of the block, and the pre-heat analyses of the test. Section 4 describes the fracture network contained in the block. Section 5 describes the heating/cooling system used to control the temperature in the block and presents the thermal history of the block during the test. Sections 5 through 9 report the measurements made on the block during the preheating, heating, and cooling phases. These measurements include temperature, thermal conductivity and diffusivity, hydrological measurements (electrical resistivity, neutron logging, gas pressure, and relative humidity), geomechanics, selected chemical analyses, and microbial activity. These sections also include analyses and simulations of the block behavior.

Finally, conclusions are presented in Section 10. Complete data sets were submitted during the time the test was conducted. The data tracking numbers (DTNs) of all of the data are presented in Table 1-1.

Table 1-1. LBT Data Tracking Numbers

Description	Status	Data Tracking Number
Effect of Rock–Water Interaction on Permeability	QA	LL950916504242.018
Relative Humidity, Saturation, Lab Tests	QA	LL960100604244.007
Fracture Map of East Face	QA	LL960400404244.012
Fracture Map of South Face	QA	LL960400504244.013
Fracture Map of West Face	QA	LL960400604244.014
Fracture Map of North Face	QA	LL960400704244.015

Permeability, Lab Tests on Core	QA	LL960905204244.022
Geomechanical Properties, Small Blocks	QA	LL970407204243.011
Geomechanical Properties, Small Blocks	QA	LL970407304243.012
Temperature	QA	LL970803004244.036
Rock Displacement, MPBX	QA	LL970803104244.037
Relative Humidity	QA	LL970803204244.038
Moisture Content	QA	LL970803404244.040
Thermal Conductivity, Thermal Diffusivity	QA	LL970803504244.041
Neutron Log Data, Water Content	QA	LL971204304244.047
Geomechanical Properties, Small Blocks	QA	LL980204504243.016
Geomechanical Properties, Small Blocks	QA	LL980207304243.018
Geomechanical Properties, Small Blocks	QA	LL980208104243.019
Air Permeability	QA	LL980706604244.063
Electrical Resistivity, Saturation, ERT	QA	LL980913304244.072
Thermal Gradient, X-ray Diffraction	QA	LL980916004242.055
Heater Power, Temperature Profiles	QA	LL980918904244.074
Neutron Logs, Water Content	QA	LL980919304244.075
Rock and Fracture Displacements	QA	LL980919404244.076
Electrical Resistivity, Saturation, ERT	QA	LL981001604244.079
Rock and Fracture Displacements	QA	LL981004604243.024
Air Permeability	QA	LL981106204244.083
Thermal Expansion	QA	LL981202104243.028
Permeability	QA	LL981202904242.079
Geomechanical Properties, Small Blocks	QA	LL981204004243.030
Compressive Strength, Modulus, Effect of Radiation	QA	LL981208504243.031
Fracture Frequency, Location	QA	LL981211004244.093
Compressive Strength, Modulus, Effect of Radiation	QA	LL990205304243.032
Fracture Attitude, Frequency, Gradient	QA	LL990707004244.101
Compressive Strength, Modulus, Lab Tests	QA	LL000209404243.036
Permeability, NUFT	QA	LL000314304242.094
Barometric Pressure	QA	LL000317504244.108
Permeability, NUFT	QA	LL000321204242.092
Invar Rod Thermal Expansion Coefficients	QA	SNL22100196001.003
Drift-Scale Hydraulic and Thermal Properties	NQ	LB990861233129.001
Mountain-Scale Hydraulic and Thermal Properties	NQ	LB997141233129.001
Insulation Properties	NQ	LL940800104244.000
Hydrologic Prop., Effect of Thermal Gradient, Lab Tests	NQ	LL940800504242.000
Hydrologic Prop., Effect of Thermal Gradient, Lab Tests	NQ	LL940800704242.002
Preliminary Characterization	NQ	LL940800804244.001
Gas Permeability, Temperature, Lab Tests	NQ	LL940909304242.007

Moisture Content, Permeability, Porosity	NQ	LL950102904244.003
Lab Geomechanical Tests, Load, Strain, Temperature	NQ	LL950803104243.001
Electrical Resistivity	NQ	LL950812304244.006
Rock Strain, Small Blocks	NQ	LL950812404243.002
Porosity, Density, Drying and Re-Wetting Tests	NQ	LL950812704242.017
Relative Humidity, Lab Tests	NQ	LL960201304244.010
Electrical Resistivity. Lab Tests	NQ	LL960201404244.011
Water Imbibition	NQ	LL971204204242.025
Electrical Resistivity, Saturation, ERT	NQ	LL980916704244.073
Water Content, Air Perm., Displacement, Resistivity	NQ	LL981110604244.084
Fracture Frequency, Saturation, Temperature	NQ	LL981110804244.086
Bacterial Types, Abundance, Growth Rates	NQ	LL981202305912.004
Hydro. Prop., Effect of Thermal Gradient, Lab Tests	NQ	LL981203004242.078
Rock Strength, Small Blocks	NQ	LL981203504243.029
Rock Physical Properties, FLAC Model	NQ	LL990201804243.031

THIS PAGE INTENTIONALLY LEFT BLANK

2. BACKGROUND

The U.S. Department of Energy (DOE) is investigating the suitability of Yucca Mountain (YM) as a potential site for the nation's first high-level nuclear waste repository. As shown in Figure 2-1, the site is located about 120 km northwest of Las Vegas, Nevada.

Favorable aspects of YM as a potential repository site include its arid environment and the sorptive properties of the rock materials. The arid environment results in unsaturated conditions at the potential emplacement horizon, which is the Topopah Spring tuff (Tptp) of the Paintbrush Group. The major advantages of unsaturated conditions are that waste package material corrosion, waste-form leaching, and radionuclide-transport mechanisms are minimized because of the lack of water in the waste package environment.

Regulations require that a repository must isolate radioactive wastes for long periods of time. Specifically, evaluation must be made of the repository system's isolation potential, composed of both natural and engineered components, for a minimum of 10,000 years and up to one million years.

Direct testing of the processes and performance of a repository can only be conducted in limited regions for a very short time. Therefore, analyses based on conceptual models using computer codes to evaluate or predict the performance will be the basis for determining the potential for the repository to properly function (that is, to provide isolation) over the long times required. Such an analysis entails more than merely achieving a scientifically acceptable view of the repository. It must provide sufficient rigor in evaluation of the models and assumptions to be useful in a regulatory process wherein the analyses will be subject to challenge by the regulatory agency, the supervisory agencies, and the interveners. Thus, the models need to be tested and verified to the greatest extent possible.

Among the processes considered in the LBT were thermally driven hydrologic processes in unsaturated fractured porous rock, plus coupling to mechanical and chemical responses.

2.1 THE TESTING STRATEGY

The testing strategy developed to address coupled processes is designed to evaluate these processes by accelerating portions of the testing to address different segments of the time frames of interest and to look at the functional relationships of different geometric scales. The LBT was designed to be one of a series of tests performed at different scales and conditions that assist in defining the physical processes that need to be considered in models of a potential repository in Yucca Mountain and to provide real-world testing of the conceptualizations and model approaches used to evaluate the behavior or development of the environment that interacts with the waste components and other elements of the engineered system. A more detailed discussion of the processes that are considered to be important in terms of testing is contained in Volume 1 of the *Near-Field and Altered-Zone Environment Report* (Wilder 1997, pp. 1–109) and in the *Near Field Environment Process Model Report* (CRWMS 2000b). Planning for field testing that includes the basis for the LBT is documented in Buscheck and Nitao (1995, p. 11).

Because no single test can address all of the issues that must be studied for a potential repository, several different test approaches are being used to assess the models. The types of tests, identified in order from the smallest geometric scale to the largest, and generally from the shortest duration to the longest, fall into the following categories:

- Laboratory tests of core-size samples
- Laboratory tests of ~1-m scale block samples (small-block tests)
- Large block test
- In-situ tests, such as the Single Heater Test (CRWMS M&O 1999a), the Drift Scale Test (CRWMS M&O 1997), and the possible Cross Drift Thermal Test
- Performance confirmation tests

2.2. TEST SCALES

Laboratory testing on core-sized samples has been used to measure properties and processes of intact samples and intact core samples containing one single fracture. The duration of such tests tends to be short, usually a few days or months.

The next scale of tests includes those performed in the laboratory on block samples that are as large as 1 m on a side. These samples are large enough to allow testing of fractures or discontinuities and even some multiple-fracture responses and interactions. To distinguish the larger scale represented by the LBT from the 1-m-scale block tests, these latter tests are sometimes designated as the small-block tests (although their dimensions are not small). The small-block tests measure block properties, including fractures. They provide an understanding of the processes and properties of a fractured rock mass and help develop a functional relationship in terms of the influence of scale of testing on properties and processes.

The next scale of testing is represented by the LBT, which is unique in both size and test conditions. The LBT is a critical test because it is of sufficient size to incorporate a fracture system that is representative of the distribution of fracture dimensions and characteristics that would likely be present in a repository—with the possible exception of major geologic structures, such as faults. The LBT location was chosen to include large, through-going fractures as well as small, healed fractures that are of limited extent. The LBT location also includes a variety of fracture sizes, connectivities, and characteristics that fall between the bounds of the large and the very small test dimensions. The LBT allows for boundary controls and monitoring that are somewhat similar to those typical of laboratory studies, and it allows for three-dimensional characterization and monitoring. The unique combination of size with boundary controls of the LBT allows processes to be evaluated and models to be tested more completely than in tests of any other scale. The focus of the LBT is, thus, to evaluate and test process understandings, conceptualizations, and models. This test is not intended to characterize YM or to measure responses of potential repository horizon rock mass. Rather, its purpose is to provide

testing and data related to the conceptual understanding of processes and to build confidence in models by testing against appropriately sized rock-mass responses.

The next in scale of the planned tests are in-situ tests such as the Single Heater Test (SHT) and the Drift Scale Test (DST). These are relatively large tests that involve hundreds of cubic meters and extend for many months or years. They incorporate sufficient volumes of rock mass to be representative of total rock-mass responses (with the caveat that fracture domains can vary, and faulting is a localized phenomena that might not be well represented in field studies). These tests have boundary conditions that are less controlled than those of the LBT. Thus, they are focused more on hypotheses-testing for processes that are scale-dependent (thus cannot be tested at the LBT) and on characterization of repository rock-mass behavior. The in-situ tests focus on testing of the actual repository rock mass under conditions of stress, and so forth, that are more representative of the repository.

Although the in-situ tests last several years, they are nonetheless highly accelerated compared with the rates and other processes that will be typified by an actual repository. In a repository, processes such as heating, moisture redistribution, and rock–water interaction will occur at time scales of hundreds to thousands of years. The final type or scale of tests are performance confirmation tests, wherein the rock mass is monitored for the processes and parameters that are associated with the actual emplacement waste.

Confirmation testing does not involve issues of scale because the actual repository and its associated process rates will be monitored. Thus, one of the primary purposes of such testing is to confirm that the testing performed at partial repository scales and abbreviated time frames accurately reflects or predicts the behavior of the system. However, even this type of testing or monitoring will not address all of the issues related to the coupled thermal-hydrological-mechanical-chemical (THMC) response (Buscheck and Nitao 1995, p. 3) of the rock mass to waste emplacement because only very early heating phase responses can be monitored (100 to 200 years as opposed to 10,000 to 1,000,000 years).

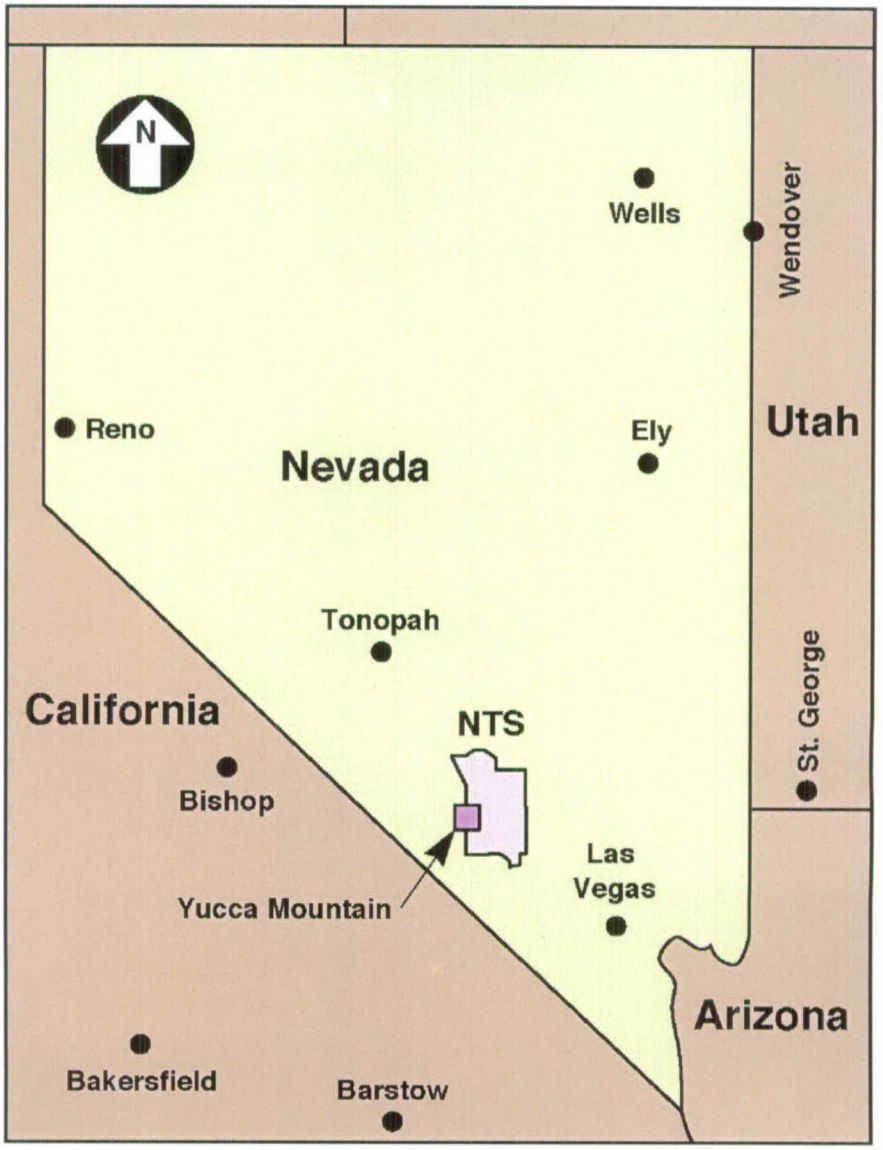

Figure 2-1. Location of the Yucca Mountain Site

3. TEST DESCRIPTION

3.1 OBJECTIVES OF THE LARGE-BLOCK TEST

3.1.1 Overall Objectives

The main determinant of how the Near Field Environment (NFE) evolves is the coupling of heat from the radioactive decay of the waste to the geologic materials and water present within those materials. As noted in Volume I of the Near-Field and Altered-Zone Environment Report (Wilder et al. 1997, pp. 1–109), many coupled processes must be understood to determine the environmental conditions that interact with the waste and other components of the potential repository system.

The LBT was one of a series of tests intended to assist in defining the physical processes that must be considered in models of the evolution of the environmental conditions of a potential repository at Yucca Mountain. As such, it provided real-world testing of the conceptualizations and model approaches used to evaluate the behavior or development of the environment that interacts with the waste and engineered components, called the Engineered Barrier System (EBS). The LBT focused on the in-rock processes of what has been defined as the NFE. The primary objective of the LBT was to provide observations of the coupled THMC processes that took place within a fractured rock mass, representative of the potential repository rock mass, in response to imposition of one-dimensional heating. One-dimensional heating was chosen so that the test data could be readily usable for testing processes predicted by one-dimensional models, which will eventually be incorporated into three-dimensional models for predicting the processes in a potential repository. Thus, its purpose was to assist in identifying of the processes that must be incorporated in the models and to provide real-world testing of the conceptualizations and model approaches used to evaluate the behavior or development of the environment that interacts with the EBS.

The LBT was not intended to characterize properties or even processes that are unique to the waste emplacement horizon in the YM potential repository. Rather, its purpose was to test conceptualizations in a representative rock mass so that the tools used for the characterization and analyses of YM are appropriate, and so that models are sufficiently valid (Section 1.4 of Wilder et al. 1997). This is in contrast to the important role of the in-situ thermal tests identified by Hardin (1998, Section 3.4.1) in the calibration of thermohydrologic properties that are required by models supporting the Total System Performance Analysis for Viability Assessment (TSPA–VA) (CRWMS M&O 1998) and the Total System Performance Analysis (TSPA) for Site Recommendation and License Application (CRWMS M&O 1999b).

The question of how best to build confidence in models has been the focus of considerable discussion over the years. Validation of models was discussed frequently in the Yucca Mountain Site Characterization Plan (DOE 1988, Section 8.3.5.20.), and considerable debate developed over how to validate models (see, for example, Buscheck and Nitao [1995, p. 9]). The concept of testing to build confidence in models replaced the concept of validation, and this was the objective of the LBT. As noted by Konikow and Bredehoeft (1992), models "...provide a means to organize our thinking, test ideas for their reasonableness, and indicate which are the sensitive

parameters. They point the way for further investigation. They help formulate critical experiments with which to test hypotheses."

Buscheck and Nitao (1995, p. 9) note that no individual model is itself a "valid" representation. However, the combined use of suites of model calculations provides a means to identify critical dependencies, evaluate worst-case scenarios, and develop fundamental hypotheses that can be addressed by subsequent analysis and testing. Buscheck and Nitao (1995, p. 9) identified a list of major hypotheses, based on model analyses, that should be tested in field tests. Buscheck noted in Volume II of Wilder (1996, Section 1.9.2, p. 1.9–4) that field tests—such as the LBT—performed at Fran Ridge and the in-situ thermal tests—such as SHT and DST—at the Exploratory Studies Facility (ESF) will provide the most conclusive means of evaluating issues associated with thermal loading, including resolution of the major hypotheses.

The objectives of the LBT, as stated in the activity plan, AP-LBT-01, (Lin 1994), are to:

- Assist in understanding the processes that are expected to occur within the NF and the Altered Zone (AZ).
- Provide a test of the models and conceptualizations.
- Allow evaluation of techniques and equipment that will be used in subsequent in-situ tests. (This objective is less applicable because the LBT did not start early enough to provide these data prior to fielding of the in-situ tests.)

3.1.2 Specific LBT Design and Implementation Objectives

As noted, the objectives of the LBT were to build confidence in the models used in assessing the evolution of the NFE. Understanding the coupled THMC processes was one of the primary objectives of the LBT. Developing a proper understanding of that coupling required that the test be conducted within a rock mass with characteristics as similar as possible to those of the potential repository horizon. Therefore, specific objectives were developed to determine the selection of the test location and the specific rock units that would be tested, the size and configuration of the test, and the basic operation and layout of the test.

Location and rock unit selection were based on the following criteria:

- Rock unit would be representative of that of the potential repository horizon. On this basis, the middle non-lithophysal zone of the Topopah Spring welded unit was selected as the target. This was consistent with the unit that would be used for underground testing.
- The bulk air permeability in the block be greater than 0.1 md (10–16 m^2).
- The initial water saturation in the block should be at least 50%.

- Fracture sets should be similar to those of the potential repository. It was judged that the majority of fractures would be high-angle fractures with fracture density of ~40 fractures/m^3.

- Block size should be sufficient to include major and minor fractures. It had been noted that the majority of flow in fracture-dominated flow systems occurs only within a small percentage of the fractures (5–10% at most). Therefore, to increase the potential to measure the effect of fracture on flow, an objective was to include sufficient number of fractures within the rock volume so that at least a few major fractures would be present. Thus, the block should be of sufficient size to contain about 100 fractures. Based on 40 fractures/m^3 (mostly high-angle fractures so that there would be approximately 30 fractures/m^2 along a horizontal plane), a block with 3.5 m^2 in the horizontal plane would be the minimum size.

- Three-dimensional characterization and monitoring would be provided. This objective was achieved by exposing the block on all sides and on the top. The fractures in the block could be characterized from the five exposed surfaces and the boreholes. This fracture information facilitated the analysis of the test results and a better understanding of the completed processes.

- A zone of dryout sufficient to mobilize water and to support a reflux zone would be developed. A dryout zone of approximately 0.75–1 m was desired.

Detailed site-selection processes are presented in Section 3.5.1.1.

To build confidence in the models, the LBT needed to be designed to properly monitor the processes that would be included in the models. Therefore, one of the specific objectives for the LBT was to focus the design of the test on those coupled processes of concern identified by model analyses. Thus, the LBT design was based on numerical modeling of the important aspects of a potential repository, on previous laboratory and field studies, and on recommendations derived from the results of those studies. The LBT objectives were to address those issues identified by modeling as significant to the evolution of the NFE. The specific objectives were to design a test that could help determine: (1) the dominant heat-transfer mechanism, (2) if there is coincidence of the dryout zone and the boiling-point isotherm, (3) refluxing of condensate water above the heated zone, (4) the change of water chemistry in the condensate zone, (5) the mechanical responses of the block, and (6) the relation between rewetting and cooling of the dryout zone.

One major issue, related to objectives 2 and 3, was to determine the likelihood of refluxing and the conditions under which it can occur—more specifically, to determine whether condensate can build up above the heated zone (and thus the repository drifts) or if it would be transported by shedding to regions below the heated zone. Another issue was to determine if condensate will penetrate the boiling zone, whether dryout can occur, and whether temperatures will be limited to the boiling point.

Although the potential for condensate buildup and shedding is design-specific, another objective was to design the LBT to maximize the potential for observations while reflecting the likely overall repository design. The basic repository feature that was considered in the design objective was a series of parallel emplacement drifts that might develop a horizontal planar region of boiling. This would be the condition that would result in the greatest likelihood of condensate buildup, rather than shedding between drifts. Therefore, a specific objective was to design the LBT to create and monitor one-dimensional heating.

The one-dimensional heating objectives were:

- Fracture permeability in the range of those expected at the potential repository horizon.
- Sufficient vertical extent to allow heat pipe zones to form and to have a large enough zone for geochemical/mineral alteration to be sampled. It was judged that a reflux model analysis of a heat zone of approximately 1 m would be required.

One specific objective of the LBT, in contrast with other field tests, was to provide controlled boundary conditions. This allowed observation and testing of some of the specific coupled THMC processes that could not be controlled or facilitated in a more open system. As an example, the heat loss could be either controlled or monitored. Also, the temperatures at the top could be maintained so that reflux cycles can be provided and monitored.

One of the major advantages of the LBT was that geochemical processes could be evaluated by carefully observing the mineralogy that develops within the block in response to the refluxing, because the refluxing zone can be well identified. The LBT is the only field-scale test that allows for such analysis. Although this was not the only, or even the primary, objective of the test, it was nonetheless a critically important one.

The LBT had as a secondary objective to evaluate the responses of introduced materials—specifically cement and steels typical of waste packages (WPs)—to the potential environmental conditions of the repository. Coupons of certain candidate WP materials placed in the block were examined before and after the test for their response to the environment. Furthermore, the LBT provided an opportunity to evaluate microbial survival and mobility.

3.2 CONFIGURATION OF THE LBT

The test location was selected at Fran Ridge to reflect the specific objectives regarding rock unit, fracture characteristics, and permeability. Detailed discussions of the site selection and characterization can be found in Sections 2.1 and 2.2 of the Large Block Test Status Report (Wilder et al. 1997) and are summarized in Section 3.5 of this report.

To observe coupled THMC behavior, the size of the test was chosen so that the block of rock to be heated was large enough to contain several fractures but still small enough so that boundary conditions and rock heterogeneity could be adequately controlled and/or characterized without undue cost.

A rectangular prism of rock 3 m × 3 m in cross-section and 4.5 m high was exposed from an outcrop of fractured rock at Fran Ridge by excavating the surrounding rock, as shown in Figure 3-1.

In general, two subvertical sets (one dominant) of major fractures and one set of subhorizontal fractures intersect the block (Figures 3-2 and 3-3). The subvertical fracture sets are approximately orthogonal, with spacing of 0.25 to 1 m, and are oriented generally in the NW-SE (dominant set) and NE-SW. Moreover, a major subhorizontal fracture is located approximately 0.5 m below the top surface. This fracture is visible in Figure 3-3. More detailed analyses (Wagoner 1999) identified a total of six fracture systems within the LBT rock mass, which are summarized in Table 3-1. The fracture analysis is presented in Section 4.

Table 3-1. LBT Fracture Systems

System #	Strike and Dip Direction
1	Strike: N50E Dip: 40–45° NW
2	Strike: N30-40W Dip: 60–80° NE
3 (contains the most significant fracture in the LBT)	Strike: generally NW Dip: mainly 20 SW
4 (contains the greatest number of fractures)	Strike: range from N03 to 34W Dip: 77–89° SW
5	Strike: general east-west Dip: near vertical
6	Strike: northeast Dip: near vertical

The heating duration of the test was designed to provide a sufficient length of time for thermal-hydrological-chemical (THC) processes to develop. The heating phase of the LBT began on February 28, 1997, and ended on March 10, 1998, when the heaters were turned off to begin a natural cooling phase. The cooling of the block was monitored until September 30, 1998, when it was determined that the block had returned to ambient temperature and the Data Acquisition System was turned off. During the heating phase the block was heated from within to reach a temperature of about 140°C at the heater horizon, and a heat exchanger was used to keep the top temperature at about 60°C. During the last four months of the heating phase, the heater power was reduced to maintain an almost constant temperature.

The desired thermal regime was determined by scoping TH calculations, as described in Section 3.5.2.1. For ease of thermal modeling, a one-dimensional thermal field within the block was created by line heaters used to simulate a planar heat source located at a height of one-third of the total height of the block (1.75 m from the base of the block). A heat exchanger system was used to maintain a constant temperature on the top surface of the block. This system consisted of an aluminum plate fitted with heating/cooling coils mounted on the top of the block. This plate was connected to a heat exchanger to allow thermal control of the top surface. The sides of the block were insulated. A planar zone of boiling was created by imposing and maintaining this

one-dimensional thermal gradient within the rock mass. Details of the heating/cooling system are given in Section 5.1.

In order to achieve a one-dimensional thermal-hydrological process, a layer of room temperature vulcanized rubber (RTV) and Viton were installed on the block sides to minimize moisture flux. Three layers of thermal insulation materials were installed on the outside of the moisture barrier. All of the instrument holes were sealed by cement grout, packers, or an RTV/Teflon membrane.

3.3 INSTRUMENTATION, MONITORING AND CHARACTERIZATION

Because the primary purpose of the LBT was to provide data to test model conceptualizations and applicability to the near field (NF) analyses for the YMP, the LBT was very thoroughly monitored by instrumentation emplaced in boreholes and on the block surface. These boreholes, as shown in Figure 3-4, also provided core and borehole video images to augment the characterization of the block from the five exposed surfaces. This provided excellent three-dimensional characterization of the fractures within the block, as shown in Figures 3-5 and 3-6, as well as in Figure 3-3.

The instrumentation installed was intended to give data for three principal process models: thermal, hydrological, and mechanical. For purposes of monitoring and discussion of the instrumentation, these process models are considered as single coupled models. In reality, the coupling is much more complex and fully coupled, but for ease of discussion as well as instrumentation design the monitoring considered the single coupling. The models for which monitoring through instrumentation was performed were those that addressed the thermal responses of the rock mass (including fluids) to imposition of heat, simulating that from emplaced waste; secondly, the models used to analyze hydrological coupling to the resulting thermal regime; and third, the mechanical response to the thermal regime. In addition to these primary areas of monitoring, geochemical coupling was considered. However, there were no boreholes or instrumentation provided for active monitoring for geochemistry because there were no chemical sensors available for monitoring unsaturated medium, and sampling procedures would impact the test. Microbial monitoring was also provided for holes drilled for other monitoring purposes.

The boreholes and instrumentation were categorized in accordance to the objectives of that monitoring (e.g., hydrology, temperature, mechanical). The boreholes, with instrumentation types installed and the size of the boreholes, are listed in Table 3-2. The holes listed according to the block faces are shown in Appendix A. The x-y-z coordinates of all of the sensors in the LBT are shown in Appendix B.

Figures 3-7 to 3-10 show the location of instrumentation holes within the block (on top, north, east, and west faces respectively). There is no instrumentation hole in the south face.

Table 3-2. Borehole and Instrument Listing by Instrument Type

Hole or instrument number	Description	Installation method	Borehole size (cm)
Heater holes			
EH1	Power and temperature	Open hole with a plug at the collar	3.81
EH2	(same)	(same)	3.81
EH3	(same)	(same)	3.81
EH4	(same)	(same)	3.81
EH5	(same)	(same)	3.81
Total = 5			
Neutron holes			
TN1	Neutron liner grouted in place	1/16/97, grouted	3.81
TN2	Neutron liner grouted in place	1/16/97, grouted	3.81
TN3	Neutron liner grouted in place	1/16/97, grouted	3.81
TN4	Neutron liner grouted in place	1/16/97, grouted	3.81
TN5	Neutron liner grouted in place	1/16/97, grouted	3.81
NN1	Neutron liner grouted in place	1/16/97, grouted	3.81
NN2	Neutron liner grouted in place	1/16/97, grouted	3.81
NN3	Neutron liner grouted in place	1/16/97, grouted	3.81
NN4	Neutron liner grouted in place	1/16/97, grouted	3.81
NN5	Neutron liner grouted in place	1/16/97, grouted	3.81
NN6	Neutron liner grouted in place	1/16/97, grouted	3.81
WN1	Neutron liner grouted in place	1/16/97, grouted	3.81
WN2	Neutron liner grouted in place	1/16/97, grouted	3.81
WN3	Neutron liner grouted in place	1/16/97, grouted	3.81
WN4	Neutron liner grouted in place	1/16/97, grouted	3.81
Total = 15			
RTD holes			
TT1	RTDs grouted	30-RTD bundle	3.81
TT2	RTDs grouted	30-RTD bundle	3.81
NT1	RTDs grouted	14-RTD bundle	3.81
NT2	RTDs grouted	14 RTDs-larger borehole to grout	7.62
NT3	RTDs grouted	14 RTDs-larger borehole to grout	7.62
NT4	RTDs grouted	14-RTD bundle	3.81
WT1	RTDs grouted	14-RTD bundle	3.81
WT2	RTDs grouted	14-RTD bundle	3.81
WT3	RTDs grouted	14-RTD bundle	3.81
Total = 9			
MPBX holes			
TM1	Mech MPBX grouted in		7.62
NM1	Mech MPBX	Grouted after install	7.62
NM2	Mech MPBX	Grouted after install	7.62
NM3	Mech MPBX	Grouted after install	7.62
WM1	Mech MPBX	Grouted after emplacement	7.62
WM2	Mech MPBX	Grouted after emplacement	7.62
WM3	Mech MPBX	Grouted after emplacement	7.62
Total = 7			

Hole or instrument number	Description	Installation method	Borehole size (cm)
Optical extensometer			
TM2	Optical extensometer with liner		7.62
Total = 1			
ERT hole			
ERT	ERT electrodes	Grouted after installation	3.81
Total = 1			
Hydro packers			
TH1	Hydrol w/ packer	High-temperature packers with gas pressure transducers, humidity sensors, and introduced material coupons	7.62
NH1	Hydrol w/ packer	(Same as above)	7.62
WH1	Hydrol w/ packer	(Same as above)	7.62
WH2	Hydrol w/ packer	(Same as above)	7.62
Total = 4			
Observation			
NO1	Observation hole	Pyrex liner w/crape paper-pvc support	3.81
NO2	Observation hole	Pyrex liner w/crape paper-pvc support	3.81
WO5	Observation hole	Pyrex liner w/crape paper-pvc support	3.81
EO3	Observation hole	Pyrex liner w/crape paper-pvc support	3.81
Total = 4			
TR1 WR1 WR2	REKA (Rapid Evaluation of K and Alpha)	Grouted after install	1.27

3.3.1 Installation of Instrumentation and Data Collection Systems

Monitoring instruments were installed within the block during the period from December 10, 1996, to February 28, 1997. This included RTDs, ERT electrodes, MPBX systems, neutron hole liner, fracture monitors, REKA probes, packers, heaters, and heat-exchange unit.

The block was sealed with thermal and moisture barriers on its four sides. The moisture barrier included a layer of high-temperature RTV silicone sealant overlain with a layer of high-temperature Neoprene rubber sheeting (Viton). The RTV was troweled into the block, with special attention to sealing fractures along the block surface. RTV-sealed surfaces acted as a bind for the Neoprene, which was applied while RTV was still curing. The LBT featured two data acquisition modes: automated data acquisition by a data acquisition system (DAS) and manual data acquisition. The data acquired by the DAS included temperature, gas pressure, displacement, wattage, humidity, and REKA probes. Data being collected manually included neutron logging, ERT, and air permeability. Data from the DAS were transferred to the Test Coordination Office (TCO) for incorporation into their data base and transferred to Lawrence Livermore National Laboratory (LLNL) via compact disks (CDs) to be downloaded to the LLNL database.

3.4 MEASUREMENTS

3.4.1 Thermal Monitoring

3.4.1.1 Temperature

The temperature measurements included the spatial and temporal variation of the temperature in the block and the thermal gradient on the block surfaces. Resistance temperature devices (RTDs) were used to measure temperatures in the block, and temperature was measured in nine RTD holes and five heater holes (see Table 3-2). The RTD holes were instrumented with RTDs at 20-cm spacing. This was accomplished by grouting a bundle of RTDs with cement in each of the temperature holes. In addition, five RTDs were placed in a thin-walled stainless-steel tube so that they could be calibrated or replaced during the test. The stainless-steel tube was grouted along with the RTD bundle in-hole TT1. Three RTDs were placed in each of the five heater holes at about 0.6, 1.5, and 2.4 m from the collar. The thermal gradient to determine heat flux out of the block across the block surface was measured by a pair of RTDs on both sides of a 1.2-cm-thick Ultratemp insulation panel. Ultratemp panels were mounted on the four vertical faces of the block, on the outside of the Viton sheet.

3.4.1.2 In-situ Thermal Conductivity and Thermal Diffusivity

In-situ measurements of the thermal conductivity and thermal diffusivity of the large block were done by using the Rapid Evaluation of K and Alpha (REKA) thermal probe method (Danko and Mousset-Jones 1991). The REKA probe method incorporated the application of three small probes (0.013-m diameter and 0.125-m length) that were cemented in the REKA holes Table 3-2). The probes were heated by built-in heaters of 2 W during the measurement period of 24 hours. When not activated, the probes were not heated.

The temperature fields along the probes were recorded by a Hewlett Packard data acquisition system that was remotely controlled from Reno. The readings were recorded on disks, as well as entered into the YMP TCO database. After the original data disks were brought to Reno, the temperature fields were evaluated against the unknown thermophysical properties, such as heat conductivity (k) and thermal diffusivity (alpha).

The k and alpha values, as well as the undisturbed rock temperatures during the REKA measurements, were plotted versus the time of measurement, measured in days from the start (i.e., day zero) of the main heating of the rock.

3.4.1.2.1 REKA Measurement and Evaluation Principles

The REKA method involves a single borehole probe with a heater and a temperature measurement section. An elliptical temperature field is generated by the heater, and the temperature distribution along the length of the probe is recorded at several locations and at given time intervals for a period of 24 hours. An optimization procedure is used to determine the unknown thermophysical properties by minimizing the root-mean-square (RMS) error between the measured and the calculated temperature fields. The rock mass and its moisture content affect the thermophysical properties, and the values represent effective properties.

The unknown k and alpha are determined by finding the values that satisfy the best least-square-fit between the measured (TM) and predicted (ts) temperature fields using all the temperature stations and measurement readings with respect to time:

$$\sum_{1}^{8}\sum_{1}^{100} (TM - ts)^2 = \min \qquad \text{(Eq. 3-1)}$$

where

$$ts = f(k, alpha, geometry, time) \qquad \text{(Eq. 3-2)}$$

The k and alpha values in Equation 3-2 are systematically varied until the left-hand-side of Equation 3-1 is minimized. These values for the minimum error are the results of the measurement evaluation.

3.4.1.2.2 The Measurement Arrangement

Three permanent REKA probes were grouted into the large rock block at Fran Ridge. The locations of the three probes are given in Figure 3-11. The horizontal REKA Probe 1 (WR2 in Figure 3-10) was installed 0.584 m below the rock block's horizontal heater layer (HHL); the horizontal REKA Probe 2 (WR1 in Figure 3-10) was installed 0.889 m above the HHL; and the vertical REKA Probe 3 (TR1 in Figure 3-7) was installed with its representative sensor location 1.38 m above the HHL. Each probe reading approximately represents a 0.1-m-diameter spherical rock volume. The measurement system, shown in Figure 3-12, consisted of an HP75000 data acquisition unit and a personal computer controller with a phone modem for remote communication. The REKA probe consisted of a linear array of nine thermocouples, centered 0.0125 m apart and systematically arranged around the heater, and a thin-foil heater powered by 2 W using an HP3611A DC power supply. The thermocouples were mounted on a flexible, perforated, Kapton foil for sufficient grout bonding.

3.4.2 Hydrological Monitoring

Spatial distribution and temporal variation of moisture content in the rock were monitored using Electrical Resistance Tomography (ERT) and neutron logging. Relative humidity and gas pressure were measured in the packed hydrological holes. ERT is a geophysical imaging technique that can be used to map subsurface resistivity (Daily and Owen 1991). The ERT measurements consisted of a series of voltage and current measurements from buried electrodes using an automated data collection system. The data were then processed to produce electrical resistivity tomographs. The images of resistivity change can be used, along with the measured temperature field and what is known of initial conditions in the rock mass, to estimate moisture change during heating. ERT electrodes were placed on the surface of the block and in one borehole, as shown in Table 3-2.

Neutron logging was conducted periodically in 15 holes (see Table 3-2). These holes were lined with a Teflon tube liner that was grouted in place. The annular space between the liner and borehole was sealed with cement grout. Neutron logs of these holes were taken approximately once per month during the test.

Relative humidity (RH) and gas pressure were measured in four packed hydrologic holes (TH1, NH1 and WH1, and WH2), as shown in Figures 3-7, 3-8, and 3-10. The results of those measurements are discussed in Section 9.2.

In addition, four horizontally oriented observation boreholes were drilled near the bottom of the block for observing water drainage away from the block (see Table 3-2).

3.4.3 Mechanical Monitoring

The overall three-dimensional geomechanical response of the rock to the heating was monitored using six multiple-point borehole extensometers (MPBX) (Figure 3-13). Three were oriented in the north-south direction, two were oriented in the east-west direction, and one was oriented vertically (see Table 3-3). In addition, deformation of several major fractures that intersect the block sides was monitored using 3-component fracture gauges. These were installed at 17 locations on the surface of the block. The fracture gauges measured movement in directions across the fracture and along the trace of the fracture, both parallel and perpendicular to the face.

A prototype optical extensometer was also deployed in one borehole, TM2, as shown in Table 3-2.

3.4.4 Microbial Monitoring

Microbes were introduced in the block so that their survivability and migration could be studied. The transport of bacteria in the LBT was investigated by first isolating two bacterial species, *Bacillus subtilis* and *Arthrobacter oxydans*, from the local tuff at the block site. Natural mutants that can grow under the simultaneous presence of the two antibiotics, streptomycin and rifampicin, were selected from these species by laboratory procedures. The characteristics of double-drug resistance distinguish the natural mutants from the indigenous species. The mutants were cultured and then injected into the five heater boreholes of the large block hours before heating was initiated.

Bacterial samples were then collected from the observation boreholes that were approximately 1.5 m (5 ft) below the injection (heater) holes. Cells that were possibly present in the heater boreholes were collected when the heaters were removed after the entire LBT experiment was completed. The result of the microbial monitoring is presented in Section 9.3.

3.4.5 Assessment of Rock-Water Interaction

There was no in-situ chemical monitoring in the LBT. There was no plan to sample the water in the block during the test, because no significant amount of water was expected to be collected. Geochemical processes were investigated by comparing the mineralogical composition of the pre-test and post-test rock samples.

3.4.6 Other Monitoring

Coupons of waste package material and manmade material were placed in the packed hydrological boreholes in the block so that they could be examined. The analysis of those coupons has not been performed.

3.5 OVERVIEW OF CHRONOLOGICAL ACTIVITIES

3.5.1 Block Preparation and Pre-test Characterization

3.5.1.1 Site Selection

The work site at Fran Ridge, Nevada Test Site, was selected for the LBT because of its desirable rock type, fracture characteristics, and accessibility. The LBT was first located, in general terms, on the basis of a location that was cleared from an environmental standpoint for development but that was also in the general vicinity of the two U.S. Geological Survey (Sweetkind et al. 1995, p. 36) test pits that provided fracture characterization data and observation access. The location chosen is on a slope on the side of Fran Ridge.

The general location was stripped of vegetation and soil covering to expose the rock. The area was then mapped, noting observed fractures. The mapping was corrected for the slope of the outcrop by use of levels, plumb bob, and tape measures. The results of the mapping are shown in Figure 3-14. Based on this mapping, it was judged that the general site was adequate for the LBT, specifically that the rock fracturing and matrix block sizes were consistent with what was anticipated to exist at YM (Wilder et al. 1997, Section 2.1). Block preparation proceeded by excavating a level surface from which to work (Figure 3-15) and providing a sump to collect and recirculate water that would be used during sawing of the sides of the block. After the surface was leveled, more detailed mapping was performed.

As noted in Section 3.1.2, it was judged that approximately 100 fractures needed to be present to have a few fractures that would be open to flow of the magnitudes of interest. Possible locations for the LBT were then selected where a sufficient number of fractures would be included in the block to account for observed flow in fractured rock wherein less than 10% of the fractures were responsible for 90% of the flow. Pre-test thermal-hydrological (TH) and thermal-mechanical (TM) calculations, documented in Section 3.5.2 of this report, were performed to verify that the block size was suitable. It was deemed important to measure permeabilities to ensure that there were adequate zones for the tests and that the fractures were neither too open, because of being near the surface, nor too plugged by calcite. (The top portion of rock was removed to obtain a level surface and to place the test beneath a possible zone where calcite filled the fractures, as was observed in the two USGS test pits or holes.) A pattern of vertical instrumentation and measurement boreholes was laid out. These holes also served as exploratory boreholes. The pattern was arranged so that the LBT could be centered around one of two different boreholes that would become either the center or the edge of the array of instrument boreholes. Air permeability tests were then conducted to assist in selecting a final location that had sufficient permeability for conducting the LBT.

3.5.1.2 Block Preparation

Once the site for the LBT was selected, numerous vertical instrumentation boreholes were drilled and cored within the block for vertical rock bolts at one midpoint on each side and one in the center of the block as well as numerous instrumentation boreholes. Neutron logging was conducted in a few of those vertical holes to determine the initial moisture content in the rock. (See Section 6.1.2.2.1 for greater details.) The initial water saturation was determined to be about

60–80% (Figure 2–22 of Wilder et al. 1997), which was greater than the required 50%, as stated in Section 3.1.2. Neutron logging was repeated after the cutting of the block was completed to determine the effect of the wet-cutting of the block on the moisture content, and to determine the actual initial moisture content before heating was started. The block was then isolated by cutting slots, as shown in Figure 3-16, along its boundary. A belt saw was used to saw four vertical slots that formed the boundary of the large block. At the completion of cutting of each of these slots, the slots were filled with expanding foam in plastic bags to support the block and to isolate it from the effects of excavation-induced damage (e.g., from vibration). A large hydraulic jack hammer was used to excavate the surrounding rocks in about 2-to-3-ft vertical sections (see Figure 3-17, which shows the partial excavation). After excavation of the upper level (about 1 m) was completed, the top of the block was trimmed to its final surface using a commercial wire saw, and a top cross member (fabricated from welded steel I-beams) was placed on the top and connected to rock bolts on the four sides and center. (The rock bolt holes were N4 to N7 and E4 in Figure 2-7 of Wilder et al. [1997]). Excavation then proceeded in 2-to-3-ft stages with the emplacement of trucker-type straps. Some smaller blocks of rock, about 30 cm in size, were collected within a 1-m region around the large block for laboratory tests. By this excavation process, a block of Topopah Spring tuff measuring 3×3×4.5 m was isolated at Fran Ridge.

After block excavation was completed, a concrete pad was poured around the base of the block. As illustrated in Figure 3-1, all block surfaces were mapped, and horizontal boreholes were located for the emplacement of instrumentation and heaters. The horizontal instrumentation boreholes were drilled using a drill rig mounted on a built-up steel platform (Figure 3-18). The location of boreholes and types of instruments were discussed in Section 3.3. The heater plane consisted of a series of five heater boreholes drilled from the east face approximately 1.8 m (6 ft) above the pad at the base of the block and equally spaced to form a line of horizontal heater boreholes.

3.5.1.3 Block Characterization

Characterization of the test block is very important for helping the understanding of the test observations and results. The characterization of the block was treated as an integral part of the LBT. The characterization began with mapping the fractures on the Topopah Spring tuff outcrop at Fran Ridge, as mentioned in Section 3.5.1.1, and reported in Section 2.1 of the LBT Status Report (Wilder et al. 1997). The characterization of the test block included mapping and analysis of the distribution of fractures, determination of the mechanical and hydrologic properties in the laboratory, the initial moisture content, the bulk air permeability, and the mineralogical composition of the matrix and the fracture coating. The fracture characterization of the block is presented in Section 4.0 of this report. The measurement of the bulk air permeability of the block is presented in Section 6.1.1.1.1 of this report. The determination of the initial moisture content of the block is presented in Section 6.1.2.2.1 as the baseline moisture content of the neutron logging. The determination of the mineralogical composition is presented in Section 8. The pre-test and post-test characterization of the mechanical properties and the ultrasonic wave velocity are presented in Section 7.2. This section presents the laboratory-determined hydrological properties and processes of the LBT samples. Those hydrological properties include porosity, water permeability, and moisture retention curves. The hydrological process investigated was fracture flow and matrix imbibition.

3.5.1.3.1 Laboratory-Determined Water Permeability of the Matrix

Permeability is one of the basic hydrologic properties required for any hydrological modeling. The water permeability of the Topopah Spring tuff samples obtained from Fran Ridge was measured in the laboratory as a function of temperature. The technique of measuring the permeability was the steady-state flow-through method. A detailed description of the methodology and permeability measuring techniques was reported in Lin and Daily (1984). Core samples of about 2.54 cm in diameter and 5.1 cm in length were prepared from small block SPC00504573 collected at Fran Ridge during the excavation of the large block, with core identification numbers SPC00504573.4 and SPC00504573.5. The test sample was first saturated with water. Then the sample was encapsulated in membrane, which separated the sample from the confining pressure fluid. The sample assembly was placed within a pressure vessel with independently controlled confining pressure, pore water pressure, and temperature. The sample was brought to an equilibrium of certain temperature, confining pressure, and pore pressure. A differential pressure across the length of the sample was created to cause a flow. The steady-state flow rate was measured. The permeability was calculated using Darcy's equation, assuming the pore pressure gradient is linear. For water flow along the sample axis,

$$k = \mu \frac{Ql}{A\Delta P} \qquad \text{(Eq. 3-3)}$$

where k is the permeability, μ is the viscosity of water (cp), Q is the flow rate (cm^3/s), A is the area of the sample (cm^2), and l is the sample length (cm). The viscosity of water at each temperature was obtained from Eisenberg and Kauzmann (1969). The permeability has units of m^2 and was converted to the standard unit of permeability, the Darcy, where one Darcy equals 9.87×10^{-13} m^2. The error in the permeability measurement depends on a number of factors and, through the propagation of errors in the above equation (e.g., Bevington and Robinson 1992), is estimated to be less than 3%.

The measurement equipment used in the permeability measurement included a confining pressure transducer, pore pressure transducer, differential pressure transducer, and thermocouple to measure temperature. The flow rate was determined by letting water flow into a container on a balance. The weight of the balance corresponds to the volume of water that has flowed through the sample and is recorded by a computer, along with all the other data such as time, temperature, differential pressure, pore pressures, and confining pressure. Because the flow rate is low, it was necessary to consider the rate of evaporation from the collection bottle. This was found to be linear with time over a period of about one week. The water lost due to evaporation was 4.13 mg/hour. This lost water was added to the balance reading for a specific period of time when calculating permeability.

The water preliminary data are summarized in Table 3-3. The permeability of the intact Topopah Spring tuff sample was less than 10^{-18} m^2. This permeability value is consistent with that measured in cores from Yucca Mountain (Lin and Daily 1984). It is also shown in Table 3-3 that intact sample permeability was not a strong function of temperature. This is also consistent with that reported by Lin and Daily (1984).

Table 3-3. Permeability Measurements on Intact Core Sample SPC00504573.4

Temperature, °C	Confining Pressure, MPa	Differential Pressure, MPa	Permeability, μD
23	5.06	1.92	0.12
25	5.07	2.47	0.14
53	5.06	2.42	0.11
53	5.06	1.91	0.15
91	5.06	2.17	0.14
92	5.06	1.60	0.14
154	5.06	1.61	0.09
130	5.05	1.46	0.13
130	5.05	2.04	0.11
83	5.06	2.02	0.17
26	5.06	2.59	0.67
26	5.06	2.61	0.20

3.5.1.3.2 Moisture Retention Curves

The moisture retention curve of rocks is needed for modeling the hydrological processes in a partially saturated medium. The determination of the moisture retention curves was described in Roberts and Lin (1996a). The moisture retention curve is the relationship between matric potential and water saturation. In tuff we assume that the suction potential is equal to the matric potential. Matric potential is defined by Kelvin's Law as

$$\psi = \frac{\beta RT \ln(e/e_0)}{M} \qquad \text{(Eq. 3-4)}$$

where

ψ = matric potential in MPa
β = density of water at the temperature of interest in g/cm^3
R = universal gas constant (8.314 J/Kmol)
T = temperature in K
e/e_0 = relative humidity, and
M = molecular weight of water (18 g/mole)

Samples from the LBT were sub-cored to a diameter of 19.1 mm and cut into disks approximately 2.5 mm thick. Samples with obvious large cavities and inhomogeneous inclusions were avoided. The average porosity of the 12 samples is 10.4 ± 1.3% and was determined by subtracting the dry density from the saturated density and dividing by the water density. The sample identification and the porosity were listed in Table 1 of Roberts and Lin (1996a), which is also represented as Table 3-4 in this report. To determine the moisture retention curve, samples were placed in the humidity chamber at a specific temperature and ~20% RH. The measurement and test equipment for the measurement of moisture retention curves are RH sensors and balances. Measurements began on dry samples. When the weights

reached a constant value for several days (samples were weighed daily), it was assumed that equilibrium was established. When a stable weight was achieved, the RH was increased and the process repeated at the same temperature. The maximum saturation achieved at the highest RH (~98%) was ~25%. A balance with a sensitivity of 0.01 mg calibrated to a traceable standard was used to weigh the samples. Saturation was calculated by comparing weights with dry weights and taking into account porosity. The process was then repeated for the drying portion of the measurement. This cycle of measurement was then repeated at a different temperature.

One difficulty was the establishment of steady weight values at the highest humidities, particularly at high temperatures. The reasons for this difficulty are that the RH is difficult to control at the highest settings and the weight of the samples is more sensitive to changes in RH at the highest settings. Refinement of the control parameters on the humidity chambers aided in the solution of this problem.

The measurement uncertainty involved in the determination of the moisture retention curves include the measurements of weights, relative humidity, and sample size. The sample dimensions are used to determine sample wet and dry densities. It is estimated that the thickness of the sample can be determined to ± 0.005 mm and diameter to ± 0.05 mm. For the samples used here, this results in an error in sample volume of ~± 0.3%. The uncertainty in dry weight is estimated to be ~0.00002 g and for wet weight ~0.0001 g. The error in the wet weight is higher than that of the dry condition because of the difficulty in achieving and maintaining saturation levels of 100%. These uncertainties result in errors in dry and wet densities of ~0.3%. When propagated through to porosity, the error is ~1.0% porosity, or ~7–11% of the measurement.

When repetitive measurements are made on samples over a period of several days, such as the determination of weights at a specified RH, for example, the uncertainty in the measurement is often less than the statistical uncertainty in the mean of the measured parameter. In such cases, the error is taken as one standard deviation of the mean. The errors in saturation determined at specific temperature and RH vary from ~0.07 to 0.5% water saturation. Thus, the relative uncertainty is between ~1 and 10%, with a 1–2% error most common.

The uncertainty in the relative humidity is approximately ± 2% RH. When propagated through equation 1 to matric potential, the absolute uncertainties are fairly low, but the relative uncertainties are high at the matric potentials closest to zero (as much as 200% at $\psi = -1.36 \pm 2.73$ MPa).

The results of the moisture retention curves of the LBT samples are shown in Figures 3-19 to 3-21. For comparison, the moisture retention curves for the USW H-1 samples at 20°C during the drying phase are presented in Figure 3-22. The USW H-1 was one of the surface-based deep holes drilled very early in the project; therefore, its cores were not Q-cores. The moisture retention curves of the LBT samples were within the range of the USW H-1 cores. The moisture retention curve of those samples seemed to be temperature dependent. The saturation at room temperature was greater than that at 70°C. Hysteresis was observed between the wetting and drying curves, with the drying curve slightly more saturated at any suction than the wetting curve, for the USW H-1 samples at 20°C. However, at 70°C the hysteresis seemed to be insignificant for both the USW H-1 samples and the LBT samples.

3.5.1.3.3 The Porosity and Micro-Pore Structure

The porosity and the pore size distribution of rock are important parameters in the modeling of the hydrological process to determine the variation of water saturation. Carlberg and Roberts (2000) reported the determination of the effective (connected) porosity and the micro-pore structure of the Topopah Spring tuff samples obtained from the LBT site. The porosity was determined by the drying-and-saturation (gravimetric) method (Roberts and Lin 1996a). The porosity was determined by calculating the difference between the dry density and the water-saturated density (assuming that the water density is 1.0 g/cm^3). The micro-pore size distribution was determined by mercury injection porosimetry, another conventional method in the study of the pore structure of rocks. Table 3-4 shows the porosity of the LBT samples. The porosity ranged from 0.08 to 0.14, with a mean of 0.104 for the 36 samples. The results of the mercury injection porosimetry are summarized in Table 3-5. The mean porosity of the 33 samples used in the mercury injection porosimetry ranged from 0.08 to 0.20, with a mean of 0.115, which agreed well with that determined by dry-and-saturation method.

3.5.1.3.4 Visualization of Fracture Flow Versus Matrix Imbibition Using X-ray Radiography

Roberts and Lin (1996b and 1997a) reported using x-ray radiography to investigate and image fracture flow and matrix imbibition in blocks of Topopah Spring tuff with a tensile fracture. Later, Roberts and Kneafsy (in Wildenschild et al. 1998) reported adding video imaging and infrared temperature imaging to x-ray radiography to visualize the fracture flow and matrix imbibition processes. The samples used in those investigations were machined from small blocks obtained at the LBT. The block identification number, sample identification number, and dimensions, of these samples are listed in Table 3-6.

In the earlier work (Roberts and Lin 1996b and 1997a), a vertical tensile fracture was induced in the middle of the sample, oriented so that the plane of the fracture was parallel to the direction of x-ray transmission. X-rays were transmitted through the smallest dimension. Thus, in a typical x-ray radiograph, the fracture was perpendicular to the plane of the image. The sample was dried in a vacuum oven at 35°C until the weight did not change appreciably for several days. The sample was then coated with a latex moisture barrier on all sides, leaving the top and bottom of the sample exposed. A lucite frame was constructed that surrounded the sample on all sides and held the sample together. Approximately 25 in-lb of torque was applied to nylon screws holding the fracture together. At the top and bottom of the sample were chambers for ponding and collection of water.

Figure 3-23 shows a diagram of the sample assembly in the x-ray scanning machine. X-ray radiographs were taken periodically to image water movement into the fracture and rock matrix by translating the sample vertically through the 160 kVp linear x-ray source. Water flowing down the fracture could be imbibed into the matrix on both sides of the fracture. X-rays passing through the sample were converted to a digital signal by a photo-diode linear array detector and stored by a computer. X-ray attenuation contrast was enhanced by adding potassium iodide (KI) to the J-13 water. X-ray linear scans were taken periodically while water flowed along the fracture and imbibed into the matrix.

Table 3-4. The Porosity of LBT Samples Determined by Gravimetric Method

Sample†	Sample ID	Depth, m	Dry wt, g	Wet wt, g	Dry density, g/cm^3	Wet density, g/cm^3	Porosity
N1-6.3	0032079.3	1.92	1.5352	1.6111	2.23	2.35	0.110
N1-6.3A	0032079.3A	1.92	1.7890	1.8680	2.26	2.36	0.0997
N1-6.3B	0032079.3B	1.92	1.6358	1.7098	2.28	2.39	0.103
N1-11.0	0032081.3	3.35	1.6352	1.7181	2.25	2.37	0.114
N1-11.0A	0032081.3A	3.35	1.5920	1.6734	2.26	2.38	0.116
N1-11.0B	0032081.3B	3.35	1.6762	1.7525	2.30	2.41	0.105
N1-13.45	0032082.3	4.10	1.4982	1.5752	2.27	2.39	0.117
N1-13.45A	0032082.3A	4.10	1.7118	1.7951	2.27	2.38	0.110
N1-13.45B	0032082.3B	4.10	1.6954	1.7781	2.26	2.37	0.110
N1-16.9	0032083.3	5.15	1.6499	1.7522	2.20	2.33	0.136
N1-16.9A	0032083.3A	5.15	1.6094	1.6987	2.23	2.35	0.124
N1-16.9B	0032083.3B	5.15	1.6885	1.7670	2.27	2.38	0.106
N1-20.3	0032084.3	6.19	1.5438	1.6133	2.22	2.32	0.0998
N1-20.3A	0032084.3A	6.19	1.5567	1.6244	2.26	2.36	0.0982
N1-20.3B	0032084.3B	6.19	1.5109	1.5849	2.21	2.32	0.108
N4-11.6	0032104.3	3.54	1.5429	1.6036	2.26	2.34	0.0887
N4-11.6A	0032104.3A	3.54	1.6222	1.6864	2.24	2.33	0.0886
N4-11.6B	0032104.3B	3.54	1.6375	1.6969	2.27	2.35	0.0823
N5-4.9	0032107.3	1.49	1.6998	1.7687	2.25	2.34	0.0911
N5-4.9A	0032107.3A	1.49	1.6501	1.7104	2.28	2.37	0.0834
N5-4.9B	0032107.3B	1.49	1.8818	1.9569	2.31	2.40	0.0922
N5-20.4	0032111.3	6.22	1.5230	1.5909	2.22	2.32	0.0992
N5-20.4A	0032111.3A	6.22	1.4883	1.5593	2.21	2.32	0.106
N5-20.4B	0032111.3B	6.22	1.4765	1.5463	2.22	2.32	0.105
N6-4.75	0032112.3	1.43	1.7549	1.8228	2.25	2.33	0.0869
N6-4.75A	0032112.3A	1.43	1.6761	1.7374	2.29	2.37	0.0837
N6-4.75B	0032112.3B	1.43	1.7136	1.7755	2.27	2.35	0.0819
N6-14.2	0032116.3	4.33	1.6590	1.7398	2.26	2.37	0.110
N6-14.2A	0032116.3A	4.33	1.6869	1.7706	2.24	2.35	0.111
N6-14.2B	0032116.3B	4.33	1.6285	1.7137	2.23	2.35	0.117
N7-5.7	0032120.3	1.74	1.6161	1.7003	2.24	2.36	0.117
N7-5.7A	0032120.3A	1.74	1.6320	1.7051	2.29	2.39	0.102
N7-5.7B	0032120.3B	1.74	1.7091	1.7834	2.28	2.38	0.0991
N7-11.0	0032123.3	3.35	1.5850	1.6705	2.25	2.37	0.121
N7-11.0A	0032123.3A	3.35	1.6353	1.7171	2.26	2.38	0.113
N7-11.0B	0032123.3B	3.35	1.6318	1.7112	2.27	2.38	0.110
mean*	36 samples				2.25±0.03	2.36±0.02	0.104±0.013

Source: Roberts and Lin 1996a

NOTE: †Sample name consists of borehole designation followed by depth in feet below the template used to locate vertical boreholes.

*Statistical mean for 36 samples. Errors represent one standard deviation for all samples collectively.

Table 3-5. Pore Size Distribution of the LBT Samples Determined by Mercury Injection Porosimetry Method

Sample†	Total pore area (m^2/g)	Median pore diameter by volume (μm)	Median pore diameter by area (μm)	Average pore diameter by 4V/A (μm)	Bulk density (g/cm^3)	Skeletal density (g/cm^3)	Porosity
N1-5.7 to 6.3	4.6429	0.0932	0.0080	0.0350	2.3372	2.5825	0.0950
N1-10.9 to 11.5	6.9868	0.0611	0.0171	0.0345	2.2427	2.5930	0.1351
N1-11.0	8.8620	0.0303	0.0148	0.0224	2.3089	2.6081	0.1148
N1-13.4a	8.3196	37.8102	0.0180	0.0931	1.7272	2.5948	0.3344
N1-13.4b	9.6257	0.0272	0.152	0.0207	2.3102	2.6113	0.1153
N1-16.9	4.0976	0.2434	0.0116	0.0589	2.2421	2.5927	0.1352
N1-20.3	11.1302	0.0513	0.0063	0.0212	2.2239	2.5595	0.1311
N2-4.0	5.5900	0.1616	0.0071	0.0367	2.2850	2.5883	0.1172
N2-4.3	8.7110	0.0383	0.0070	0.0169	2.2967	2.5088	0.0845
N2-11.1	8.2266	0.0570	0.0075	0.0231	2.2461	2.5150	0.1069
N2-11.25	5.8431	0.1435	0.0073	0.0362	2.2900	2.6057	0.1211
N2-13.9	6.3615	0.2336	0.0071	0.0469	2.1707	2.5894	0.1617
N2-19.2	8.4895	0.0480	0.0085	0.0224	2.2567	2.5277	0.1072
N3-4.5	5.4111	0.2110	0.0068	0.0389	2.2894	2.6029	0.1204
N3-4.75	6.9874	0.0665	0.0081	0.0263	2.2555	2.5167	0.1038
N3-11.0	9.0228	0.0728	0.0073	0.0227	2.3177	2.6305	0.1189
N3-15.2	7.2965	0.1026	0.0074	0.0325	2.2679	2.6196	0.1343
N3-20.4	9.4214	0.0339	0.0087	0.0187	2.2528	2.5019	0.0996
N4-5.3	8.9013	0.0544	0.0059	0.0200	2.2611	2.5135	0.1004
N4-11.6	6.9084	0.0505	0.0084	0.0235	2.2616	2.4903	0.0918
N4-14.5	6.0849	0.1298	0.0075	0.0316	2.3096	2.5983	0.1111
N4-19.0	7.4861	0.0456	0.0125	0.0266	2.2459	2.5281	0.1116
N5-4.9	6.5621	0.0476	0.0085	0.0232	2.3276	2.5534	0.0884
N5-11.15	5.7744	0.0889	0.0082	0.0360	2.2889	2.5981	0.1190
N5-14.8	5.9586	0.0911	0.0087	0.0378	2.2465	2.5717	0.1265
N5-20.1	9.2912	0.0457	0.0076	0.0196	2.2422	2.4963	0.1018
N6-4.8	7.6122	0.0371	0.0078	0.0188	2.3001	2.5065	0.0823
N6-11.0	6.6135	0.0515	0.0106	0.0275	2.2825	2.5464	0.1036
N6-14.5	6.4598	0.1186	0.0065	0.0338	2.2666	2.5861	0.1235
N6-20.2	8.7303	1.0908	0.0062	0.0464	1.9941	2.4982	0.2018
N7-5.0	8.1133	0.0536	0.0071	0.0212	2.2718	2.5177	0.0977
N7-10.9	6.4128	0.0682	0.0105	0.0310	2.3060	2.6045	0.1146
N7-14.3	7.2915	0.0543	0.0146	0.0301	2.2768	2.6013	0.1248
E2-19.5	8.3521	0.0552	0.0086	0.0235	2.2147	2.4850	0.1087
mean*	7.3715 ±1.5795				2.2633 ±0.0596	2.5591 ±0.0456	0.1154 ±0.0228

† Sample name consists of borehole designation followed by depth in feet below the template used to locate vertical boreholes.

* Statistical mean for 33 samples. Errors represent one standard deviation for all samples collectively. Sample N1-13.4a has been excluded from statistical analyses.

Source: Table 4 of Carlberg and Roberts 2000

Table 3-6. Sample Descriptions–Fracture Flow Versus Matrix Imbibition Test

Block Number	Sample Number	Dimensions (cm)
SPC00501631	SPC00501631.1	2.45 x 10.13 x 14.1 block
SPC00504573	SPC00504573.2	2.65 x 15.14 x 29.21 block
SPC00504573	SPC00504573.3	2.62 x 14.94 x 22.96 block

A total of six experiments were reported by Roberts and Lin (1996b and 1997a):

1. Fracture flow at room temperature without shim.

2. Fracture flow at room temperature with 25-μm shims in the fracture.

3. Dehydration of the sample after Experiment #2 with a thermal gradient of ~95°C at the bottom and ~33°C at the top.

4. Fracture flow in shimmed fracture with 3 heaters at the bottom to create a thermal gradient of ~111°C at the bottom and ~28°C at the top, and a water head of ~0.02 m.

5. Fracture flow in shimmed fracture with 3 heaters at the bottom and 4 heaters on sides to create a thermal gradient of ~148°C at the bottom and ~80°C at the top, and a water head of ~0.26 m.

6. Fracture flow in shimmed fracture with 3 heaters at the bottom and 4 heaters on sides to create a thermal gradient of ~148°C at the bottom and ~80°C at the top, and a water head of ~0.46 m.

The result of experiments 1 and 2 showed that, at room temperature, imbibition occurred chiefly through the matrix for the unshimmed fracture, and primarily horizontally from the fracture to the matrix during the shimmed fracture. A roughly v-shaped wetting front was observed for the unshimmed case, and after more than 2017 hours of ponding, water still had not flowed the length of the fracture. During the shimmed fracture experiment, water flowed the fracture length after only ~0.15 hours. Different (lateral) imbibition rates were observed in different regions of the sample, demonstrating the heterogeneous properties of the rock. Enhanced imbibition appeared to be controlled by the presence of lithic fragments that contain small microfractures. A significant difference in the two series of experiments is that water was imbibed laterally into the matrix (from the fracture) at a much higher rate when the fracture was shimmed open. For the shimmed experiment, after 1000 hours a large portion of the sample was highly saturated.

The dehydration experiment (3) began after no more imbibition into the matrix was observed (shimmed experiment, >1200 hours of imbibition). Dryout along the fracture was observed and was most pronounced between 4.5 and 23 hours after heating was initiated. At longer times dryout along the fracture was not apparent, and at times greater than ~215 hours the fracture was highly attenuating. Possible explanations include:

- The fracture increased in saturation at times greater than 215 hours.

- Evaporation of water continuously along the fracture resulted in the crystallization of potassium iodide (KI) salt that attenuated the x-rays.

Another feature was the development of a horizontal band of high attenuation approximately 1.5–2 cm from the bottom of the sample. This band appeared initially at about 0.5 hours after

heating and became more pronounced with time. At about 25 hours after heating, two such bands were observed, again near the bottom of the sample.

Experiment 4 was the first fracture flow under a thermal gradient to be conducted in the series. The temperature in the bottom 2–3 cm of the sample was greater than the boiling point of water. The water head in this experiment was small, only about 1–2 cm, but not zero. The sample was dry to start with. The result of this test showed that water flowed down the fracture quickly but stopped about 13 cm from the top. It seemed that the flow was stopped by a relatively high-porosity clast that was intersected by the fracture. As time progressed, this more porous region became more saturated (attenuating) until flow proceeded around or through the region. During this time, there was significant lateral imbibition into the matrix from the fracture. After flow continued past the more porous region, the shape of the wetting front was less sharp and more rounded. This wetting front stopped about 2.6 cm from the bottom of the sample. A very narrow neck of high attenuation extended from the wetting front to another highly attenuating region at the bottom of the sample. This lower highly attenuating region was probably due to the deposition of the KI salt due to the boiling. In this test, the water never penetrated the entire fracture length. After nine days the heaters were turned off, and water still did not flow through the fracture.

Figure 3-24 shows two images to illustrate the effect of water head on the fracture flow and matrix imbibition. Those are the result of experiments 5 and 6. In those two cases the lower 6–7 cm from the bottom of the sample was the boiling zone. The convention used for the difference images is that darker colors or shades indicate relatively high x-ray attenuation and the presence of water, while the lighter areas correspond to lower attenuation and relatively dry areas. For experiment 5 the water head was about 0.26 m. The water wetted almost the entire fracture first, followed by imbibition into the matrix, as shown in Figure 3-24a. Within 7.2 hours of ponding, the water penetrated about 3 cm into the boiling zone. The difference between this experiment and Experiment 4 above was that flow continued down the length of the fracture after the heaters were turned off. This was probably due either to the increased water head or the lack of sealing of the fracture by the salt deposit. Figure 3-24b shows the result of experiment 6, in which the water head was increased to 0.46 m. The water flowed through the entire length of the fracture within minutes and continued to flow through the boiling region. Not much imbibition into the matrix was observed in this case.

Roberts and Kneafsey (in Wildenschild et al. 1998) added visualization capability to the x-ray radiography. In the later experiments, the fracture was simulated by the interface between a saw-cut tuff surface and a piece of glass. Water was flowed along the interface from the top to bottom of the block. X-ray radiography and video images were taken on the front face of the glass looking into the rock face. Temperatures were measured both within the block, using thermocouples, and on the glass surface, using infrared imaging. The water flow was also under a thermal gradient, similar to the earlier experiments. They concluded that observations in the visualization experiments supported many of the observations and conclusions made for the previous x-ray radiography experiments. For instance, in one of the early experiments, a highly attenuating band was observed above the heated region. The tentative conclusion was that this could be a region of either enhanced saturation or salt crystal formation. The visualization experiments confirmed that both the salt deposit and the condensation halo formed in the region above the boiling zone. The early experiments showed the development of a narrow, highly

attenuating neck in or near the boiling region. The visualization experiments observed similar features. They also concluded that the processes and physical phenomena observed in the tuff tensile fractures also occurred in the tuff saw-cut/glass plate interface.

3.5.2 Pre-Heat Thermal-Hydrologic Calculations

Pre-heat scoping TH calculations were conducted to assist the design of the test. These calculations were reported in Section 3 of the LBT Status Report (Wilder et al. 1997). Those scoping calculations include a series of two-dimensional (2-D) and three-dimensional (3-D) TH calculations using V-TOUGH and NUFT codes and 3-D layer model and fracture model using TOUGH2. The TOUGH2 simulations were mainly for assisting the design of the tracer tests in the block. Only the NUFT simulations are summarized here, because they used input parameters that were more relevant to the LBT. Preliminary 2-D analyses and one 3-D analysis that modeled only thermal conduction were followed by TH 3-D analyses (Lee 1995a, 1995b). Modeling results assumed either a homogeneous block having the dominant bulk permeability as measured by single-borehole air injection, or a heterogeneous block reflecting the permeability profile. The heterogeneous permeability field had a "layer-cake" distribution because the permeability measured at any depth was assumed to be constant for that depth. This does not reflect the dominant vertical attitude of many of the fractures but does represent the horizontal sets.

The pre-test calculations are presented in detail in Section 3 of the LBT Status Report (Wilder et al. 1997).

3.5.2.1 Homogeneous and Heterogeneous Cases

For the homogeneous case, an equivalent continuum model was used. A distinct dryout zone was predicted in and around the heater plane, with well-developed condensation zones above and below the heaters. In contact, the heterogeneous case did not show a well-developed condensation zone above the heaters. A distinct dryout zone was predicted, and a well-developed condensation zone was formed only below the heater plane. For the heterogeneous case, there was clearly a net loss of liquid above the heater plane. The results suggest that the saturation changes might be sensitive to permeability distribution.

Higher gas pressures were generated for the heterogeneous case. Peak gas phase pressure for the homogeneous case was only 97 kPa (14 psia), compared to 157 kPa (23 psia) for the heterogeneous case. The higher pressure is caused by additional confinement of water vapor and air by layers of bulk permeability substantially lower than those for the homogeneous permeability case.

3.5.2.2 Thermal-Hydrologic Discrete Fracture Model

An analysis using the discrete fracture model was performed in which the fracture system was modeled as a series of 200-μm-aperture fractures at a uniform spacing of 30 cm. The fractures were vertical and parallel to the heater borehole axes and to occur midway between two boreholes, as shown in Figure 3-25. It should be noted that the east-west orientation of these assumed fractures is not consistent with predominant fracture orientations, which is NW-SE.

However, the purpose of these calculations was to determine sensitivity to equivalent continuum model (ECM) versus discrete approaches.

In these analyses, distinct dryout and recondensation zones were predicted both above and below the heater plane. The dryout zone was thickest at the fractures and thinnest in the matrix, midway between the fractures (at heaters). Figure 3-26 shows the predicted temperature and liquid saturation profiles along a vertical line through the matrix at one-year heating. Block temperatures were not significantly affected by fracture location. The peak gas pressure in the system was about 177 kPa (26 psig), located in the matrix at the heater level.

3.5.3 Pre-Heat Thermal-Mechanical Modeling

This section presents results of thermal-mechanical (TM) simulations of the LBT. Pre-test continuum simulations were done using two different numerical codes that are commercially available, a 2-D finite difference model (FLAC) and a 3-D finite element model (ABAQUS™).

The goal of the initial numerical modeling was to calculate temperatures, stresses, and displacements in two and three dimensions for a simplified representation of the large block. In reality, numerous joints and fractures complicate the behavior of the large block significantly. Nonetheless, these simulations provide a general understanding of the TM behavior to be expected in the LBT.

3.5.3.1 Description of Problem

The FLAC and ABAQUS™ codes were used to perform TM simulation of the heat-up phase of the LBT. The numerical models are one-way weakly coupled in the sense that the temperature field produces thermal stresses, but mechanical stresses do not in turn influence temperatures. The temperature field is calculated as a function of time from a thermal conduction model. In simulations conducted using each code the sides and top of the block are assumed to be insulated. Also, the ground surface is assumed to be isothermal. The two codes are similar in that the mechanical model in each uses the temperature field at given times to apply thermal loading. For all simulations all of the surface stresses are assumed to be zero. For the 2-D (FLAC) analysis only one half of the block in cross-section is modeled, and for the 3-D case only one-quarter of the block is modeled; therefore, the two symmetry planes are given boundary conditions of zero displacement normal to the plane. The bottom of the model lies several meters below the ground surface, and it is also a zero displacement boundary. Up to 75 days, the temperature effects of the heating extended only a short (<2 m) distance below the block; therefore, the model bottom boundaries have little effect on the TM behavior of the large block itself.

3.5.3.2 Description of Models

This section describes the models used in the simulation of the LBT, including inherent assumptions, configuration, and input parameters. The 2-D FLAC models are described first, followed by the 3-D ABAQUS™ model.

3.5.3.2.1 FLAC Models

FLAC is a time-dependent finite difference code capable of treating both mechanical and thermally induced stresses and deformations. It is a 2-D code in which materials are represented by arbitrarily-shaped, quadrilateral zones and is capable of using several built-in constitutive relations to describe material behavior.

Version 3.22 of the FLAC code was used in this study, and a detailed description of the code can be found in the FLAC User's Manual (Itasca Consulting Group, Inc. 1993). All the FLAC modeling described in this report assumes a 2-D, plane strain geometry. This is equivalent to having infinite thickness in the third dimension, or to being in a symmetry plane (no net strain) in the third dimension. The plane of the 2-D FLAC models is the vertical plane perpendicular to the long axis of the heaters for the LBT. The FLAC models all use linear mechanical and thermal properties where mechanical properties (e.g., elastic moduli) and thermal properties (e.g., thermal expansion coefficient) are independent of stress and temperature. Constitutive relations are either isotropic elastic or else make use of the ubiquitous joint model capability of the FLAC code. The thermal response in all models assumes isotropic heat conduction.

The procedure for running a FLAC model to simulate the LBT is to first create a file that provides information about the grid used in the model as well as the mechanical and thermal properties used to represent the rock, and the mechanical boundary conditions and initial conditions. Next, FLAC is run in the mechanical mode with this file as input, to bring the model to initial mechanical equilibrium. This usually requires several thousand steps. Mechanical steady-state is reached when additional steps do not produce significant additional displacement—e.g., an additional 1000 steps results in less than 1 mm displacement for a model that showed displacements on the order of 1 cm for initial steps. The equilibrium state is saved in a FLAC output file. Then, another input file is created to provide information about the thermal boundary conditions, initial conditions, and heat sources. FLAC is run in the thermal mode with the new input file and the saved file from the previous run for a number of time steps required to follow the desired heating schedule. The resulting temperature field in the model is saved in a new FLAC output file. Note that the size of a time step is set to be slightly smaller than the area of the smallest grid element divided by the thermal diffusivity of the rock, so that heat transfer can be resolved at the scale of the grid and yet the model will not require an excessive amount of computer time for computing the temperature field. Finally, FLAC is run again in the mechanical mode, to compute the displacements and stresses that result from the thermal loading. The mechanical and thermal modeling in FLAC can be described as a one-way weak coupling, with the mechanical state affected by the temperature field but with the thermal state independent of the displacements and the stress field.

3.5.3.2.1.1 Grid Formulation

Several important limitations of FLAC must be considered when developing a grid to represent the configuration of the LBT. According to the FLAC User's Manual, errors in stress and displacement due to edge effects will be small (below 6%) if fixed model boundaries are placed at distances of at least five times the length of the region of interest in the model. For a large

block that is 5 m high, the model must therefore have distant edges at least 23 m below and at least 23 m beyond the block. The model must represent the 2-D 3 m × 4.5 m block while retaining enough small-scale detail to properly represent the 5 cm (2 in.) diameter heater holes. This suggests a grid with more gridlines concentrated in the block region, particularly around the heater holes, and fewer gridlines toward the far edges of the model. According to the FLAC User's Manual, grid elements must have aspect ratios that do not exceed 5:1, and the areas of two adjacent elements should not exceed a 4:1 ratio. The number of elements in the model, N, determines how much computer time is required for a steady-state solution, with run time proportional to $N^{3/2}$. For example, a 1000-element model may require a few minutes to run on a Sun Sparc20 workstation, and a 4000-element model would take eight times as long to run on that same computer.

The gridding used in all of the FLAC models described in this report is almost the same as that used by Lee (1995a) for hydrothermal modeling. The only differences are that one gridline 1 cm below the top of the large block in Lee's model was eliminated to avoid aspect ratio problems, and gridlines near the far edges of the model were moved slightly to prevent areas of adjacent elements from exceeding the 4:1 ratio. There are 26 vertical and 37 horizontal gridlines, for a total of 900 elements. In the FLAC models, the large block is represented as a set of zones 4.5 m high and having a 1.5 m width for half of the block. (Only half of the large block is modeled, since the block is symmetrical for a vertical cross-section.) Grid elements within the block have sizes varying from 5 cm × 5 cm to 10 cm × 20 cm. Below the block, the element sizes increase to a maximum of 16 m × 16 m at the far edges of the model but are smaller than 1 m × 1.5 m within a few meters of the large block. The heaters in the block are represented as 10 cm × 10 cm elements, placed 3 m below the top of the block. These heater elements are larger than the actual heater holes, but the heater power was scaled accordingly, as will be described later in this section. Figure 3-27 shows a detail of the grid for the large block models.

3.5.3.2.1.2 Initial and Boundary Conditions

Initial conditions used in all the FLAC modeling set all initial stresses to zero within all grid elements, and set temperatures initially to 20°C in all elements. The gravitational acceleration is 9.8 m/s^2. A set of boundary conditions was used for all of the FLAC modeling, as follows: The axis of symmetry at the left edge of the model, for the center of the large block, was modeled as an adiabatic boundary fixed in the horizontal direction. The top of the block was also adiabatic and had an applied compressive stress of 0.1 MPa (nominally zero) to simulate atmospheric pressure. The right edge of the block was adiabatic and also had an applied compressive stress of 0.1 MPa. The horizontal boundary representing the ground surface was an isothermal boundary set to a temperature of 20°C with an applied compressive stress of 0.1 MPa. The far right edge and bottom edge of the model were fixed in both the horizontal and vertical directions and were isothermal boundaries fixed at 20°C. These conditions simulate the unconfined LBT with guard heaters to prevent heat flow from the sides of the block. Modeling of the top boundary of the block could be improved by allowing heat flux out until the top reaches a temperature of 60°C, and then converting to an isothermal condition. This is a nontrivial problem in FLAC that will be addressed in future modeling. The present simple adiabatic condition allows the top of the block to reach 60°C too soon but avoids the problem of heat flux downward from the top that would occur if the top boundary were initially set at an isothermal condition at 60°C (e.g., Lee 1995a).

3.5.3.2.1.3 Heaters

All of the FLAC modeling described in this report represented the heat sources as 300-W heaters placed at 60-cm intervals at a level 3 m below the top of the large block. This configuration follows that used by Lee (1995a). Lee used a heating schedule that began with about 75 days of heating at constant power of 1500 W using five heaters, followed by reducing the power to 1200 W and finally achieving a steady-state at about 1050 W at an elapsed time of about 180 days. The FLAC modeling follows the first 75 days of Lee's heating schedule, using a constant power of 1500 W.

Each heater is represented as an internal heat source in the model, specified in units of W per square m of grid element per m in the third (infinite) direction. The actual heater holes in the LBT will each have a radius of 2.5 cm and a length of 2.7 m—i.e., a cross-sectional area of 0.0020 m^2 and a volume of 0.0053 m^3. The ratio of power to volume for the heaters is then about 0.00057 W/m^3 for a 300-W heater. For a 10 cm × 10 cm grid element having an area of 0.010 m^2, this 300-W heater is represented by scaling the value of 0.00057 W/m^3 by the ratio of the heater hole cross-sectional area to the grid element area, to obtain a source of 0.00011 W/m^3 throughout the grid element. It is clear this is an appropriate procedure for representing the LBT heaters in the FLAC modeling, since results described in later sections of this report show temperature fields that are in agreement with the temperature field produced by Lee (1995a) for modeling the LBT.

3.5.3.2.1.4 Rock Properties

Input parameters for physical properties used in the FLAC modeling are given in Table 3-7. All of the FLAC modeling described in this report used the simplest thermal conduction model available in the FLAC code. This isotropic heat conduction modeling required three input parameters: thermal conductivity, specific heat, and the thermal expansion coefficient. FLAC requires that a bulk modulus, a shear modulus, and a density be specified for any mechanical model. This is the complete set of mechanical properties in the elastic case. The ubiquitous joint model is an anisotropic plasticity model that assumes a series of weak planes embedded in a Mohr-Coulomb solid. It requires eight additional parameters to specify where and how yield may occur. A detailed discussion of these parameters and the ubiquitous joint model can be found in the FLAC User's Manual. Four properties of the Mohr-Coulomb solid are the cohesion, dilation angle, tension limit, and angle of internal friction. The joints have four properties, including the angle of the parallel joints embedded in the solid (with respect to the horizontal), the joint cohesion, the joint tension limit, and the joint friction angle. Note that since the joints are ubiquitous plastic slip planes, the ubiquitous joint model does not have a crack density parameter or joint spacing associated with it. The values for the thermal properties listed in Table 3-7 are the same as those used by Lee (1995a). The thermal conductivity and specific heat values for wet tuff are given in the YMP Reference Information Base (RIB) (DOE 1990). Future modeling may use different values as laboratory data become available from tests on 1-m blocks of Topopah Spring tuff.

The bulk modulus and shear modulus values listed in Table 3-7 were determined from elastic wave velocity measurements, both preliminary measurements on small blocks of Topopah

Spring tuff and also velocities reported from the G-tunnel heated block experiment (Zimmerman et al. 1986).

The density for tuff listed in Table 3-7 is from laboratory measurements on Topopah Spring tuff samples from the LBT site (Roberts and Lin 1996a). The tuff had a skeletal density of 2.56 g/cm^3 and a bulk density of 2.27 g/cm^3. The bulk density is appropriate for representing the density of the entire large block.

Values for the ubiquitous joint model parameters were mainly set using information from Arulmoli and St. John (1987). Their finite element TM modeling included ubiquitous joint modeling, and they report the model values they used to represent 80% saturated, devitrified Topopah Spring tuff. In Table 3-7, values for the cohesion of the solid and the internal angle of friction for the solid are those used by Arulmoli and St. John (1987). They used a value of 9.0 MPa for the tension limit of the tuff, but this is probably too high for the highly fractured large block. A value of 6.0 MPa was chosen for the FLAC modeling described in this report. Although Arulmoli and St. John (1987) do not report values for the dilation angle for tuff, the FLAC User's Manual says that values of about 10–15° would be typical for concrete or sand. A value of 10° was chosen for the FLAC modeling described in this report. Preliminary results of fracture mapping for the LBT show that most fractures in the block are subvertical, and there is a

Table 3-7. Rock Property Values Used for Modeling of the LBT

Physical property	Value	Source
Thermal properties		
Thermal conductivity	2.10 W/(m°K)	YMP RIB (1990)
Specific heat	840 J/(kg-°K)	
Thermal expansion coeff	9.1 x 10^{-6}/°K	Estimate
Mechanical properties		
Bulk modulus	2.7 x 10^9 Pa	Zimmerman et al. (1986)
Shear modulus	14 x 10^9 Pa	
Density	2300 kg/m^3	Roberts and Lin (1996a)
Cohesion	22 x 10^6 PA	Arulmoli and St. John (1987)
Dilation angle	10°	FLAC Users's Manual
Tension limit	6 x 10^6 Pa	Estimate
Internal angle of friction	29°	Arulmoli and St. John (1987)
Joint angle (cc from horiz)	10° & 85°	Estimate
Joint cohesion	6 x10^5 Pa	Estimate
Joint tension	5 x10^5 Pa	Estimate
Joint friction angle	31°	Price et al. (1993)

major subhorizontal fracture near the top of the block. A value of about 85° is appropriate for representing the joint angle for subvertical fractures, and a value of 10° is representative of subhorizontal fractures. For the joint cohesion, Arulmoli and St. John (1987) used values of 1.0 MPa and 0.05 MPa. An intermediate value of 0.6 MPa was chosen for the FLAC modeling. Arulmoli and St. John (1987) used a joint friction angle of about 39°. Reported values of the average coefficient of friction for tuff (Price et al. 1993) suggest that a value of 31° is more

appropriate for the joint friction angle, and thus this lower value was used in the FLAC modeling. In FLAC, the tensile strength is limited by cohesion and the friction angle. If the tension limit exceeds the value found by dividing the cohesion by the tangent of the friction angle, the tension limit is reset to that value. Thus the maximum value of the joint tension limit found using a joint cohesion of 0.6 MPa and a joint friction angle of 31° would be about 1 MPa. The default joint tension limit in FLAC is zero, but that would be too small a value. The FLAC modeling used an intermediate value of 0.5 MPa for the joint tension limit.

3.5.3.2.2 ABAQUS™ Models

The second method considered in the pre-test simulations is the 3-D finite element method, and the code ABAQUS™ was used to evaluate this method. ABAQUS™ is a 3-D code with capability for time-dependent analysis of thermal and mechanical behavior.

ABAQUS™ processes input in a batch fashion. The thermal model uses "therm.inp" as an independent input file, which writes a results file of nodal temperatures at specified time steps. The mechanical model uses "mech.inp" to read the results of the thermal model and calculates an equilibrium displacement field. The two models use the same nodes and linear, brick elements. The procedure for running ABAQUS™ is to first create a file that provides information about the grid used, the mechanical and thermal properties of the rock to be simulated, etc. This file is very similar to the input file used for the FLAC code. The following paragraphs discuss the input used for the simulations conducted for this study.

3.5.3.2.2.1 Time Steps

The thermal model in ABAQUS™ is run with one step and 75 increments, where each increment is one day. The mechanical model is run in seven steps. Each step represents 10 days. The mechanical problem is static and hence each step is one increment long. Altogether, the model contained 3912 nodes and 2864 elements. The thermal model took about 50 minutes to execute 75 time steps of one day each on a Sparc10 workstation. The mechanical model was computed every 10 days, and the execution time was about 30 minutes on a Sparc10 workstation. Output files were stored after every time step.

3.5.3.2.2.2 Grids, Nodes, and Elements

The nodes are divided into a "block" set and a "ground" set. The grid for the faces of the block perpendicular to the heaters is the same as that used in thermal-hydrologic simulations of the LBT (Lee 1995a) and in the thermal-mechanical FLAC model simulations mentioned above. The grid for the ground does not extend as far as the previous models, because those results showed that effects of the heating are of limited extent into the ground. The thermal elements (DC3D8) and mechanical elements (C3D8R) are paired for thermomechanical problems, in which the temperature field is first computed at different times before solving for mechanical equilibrium.

3.5.3.2.2.3 Material Properties

ABAQUS™ requires many of the same material properties as FLAC, and for the simulations conducted in this study the mechanical and thermal properties input to ABAQUS™ were identical to

those used in the FLAC elastic model and are given in Table 3-7. In the ABAQUS™ modeling, an elastic model was used to simulate the large block, and no viscoelastic properties or fracture zones were used.

3.5.3.2.2.4 Initial and Boundary Conditions

The initial temperature is 20°C for both the thermal and mechanical models. Thermal stresses arise as a result of thermal expansion relative to this reference state. The default condition for the temperature problem is that boundaries are adiabatic. In the model, all boundaries are insulated except the ground surface, which is maintained at 20°C. The default condition for the mechanical problem is that boundaries are at zero stress. In the model, all boundaries are stress-free except the symmetry planes and the bottom of the model. The load for the thermal problem is the constant temperature heaters. (Modeling the heaters as constant power heat sources requires a FORTRAN subroutine HETVAL that was not available for this study.) The load for the mechanical problem is the thermal stresses arising from the nonuniform temperature field at different times.

3.5.3.2.2.5 Output

The nodal temperatures were placed in a special results file for use by the mechanical model. Also, temperatures along the side of the block parallel to the heaters were specified to be included in the *.dat ASCII file with other results normally produced by ABAQUS™. In the mechanical model, displacements on the outer face parallel to the heaters were specified to be included in the .dat file.

3.5.3.3 Results

3.5.3.3.1 FLAC Modeling Results

Four different 2-D FLAC models were run to model the LBT. The first model assumed the large block was a homogeneous elastic solid having the elastic moduli values listed in Table 3-7. The second model assumed a homogeneous elastic large block, but the values of the bulk and shear moduli were reduced by an order of magnitude to simulate the effect of many fractures in an elastic medium. In the third model, two fractures were simulated in the block by modeling the block as an elastic medium containing one set of vertical grid elements and one set of horizontal grid elements having elastic moduli reduced by one order of magnitude. The fourth model simulated these two fractures by using the ubiquitous joint model within these sets of horizontal and vertical grid elements and representing the rest of the block as a homogeneous elastic medium.

Each of these four models was first brought to initial mechanical equilibrium. The initial maximum unbalanced force had a magnitude of about 10^6 N/m as a result of the maximum stress in the initial mechanical model, 10^5 Pa, acting on the largest grid element, having 16-m sides. This initial unbalanced force was reduced by about four orders of magnitude after 9000 steps, requiring about four minutes of computer time on a Sun Sparc10 workstation.

3.5.3.3.1.1 FLAC Thermal Results

For each of the four models, after mechanical equilibrium was attained, FLAC was run in the thermal mode to simulate heating for 75 days. Since the temperature field is not affected by mechanical properties, all of the four models had identical temperatures for any given number of days. Figure 3-28(a-e) shows the temperatures contours in a vertical cross section after 1 day, 10 days, 25 days, 50 days, and 75 days of heating, respectively. Figure 3-29a shows the temperature profile for the top of the block, and Figure 3-29b shows the profile for the grid element representing the central heater. Lee (1995a) shows a similar temperature profile for the heaters (see Figure 3-30), except that the temperatures in Lee's model are slightly lower at a given time, because he does not use an adiabatic boundary condition at the top of the block.

The figures show that the base of the block and the top 1 m of the block remain at the ambient temperature of about 20°C for the first 10 days of heating, at which time the heaters are at about 70°C. The isotherms are horizontal and are symmetrical above and below the heater plane for the first 10 days of heating.

By the 25th day of heating, the top of the block has reached a temperature of about 35°C and the heaters are at about 95°C. The isotherms are horizontal except for within about 30 cm of the heaters and the region near the bottom corner of the block where the adiabatic boundary condition for the side of the block meets the isothermal boundary condition for the ground surface. If the ground surface within about a meter of the block was adiabatic, these contours at the base of the block would be made more horizontal. After 25 days of heating, the temperature gradient is somewhat steeper below the heaters than above the heaters, because there is no heat flow out the top of the block. The base of the block is about 30–50°C at this time. No dryout zone forms in the first 25 days of heating, except for right in the plane of the heaters.

Note that the temperature change in the heater zone is very high for the first 10 days of heating, about 50°C as the heaters go from 20°C to 70°C, and is only half as much for the next 15 days of heating as the heaters go up to about 95°C on the 25th day of heating. This suggests that stresses due to thermal expansion of the rock will be developed fairly early in the 75 days of heating.

According to FLAC, the top of the block reaches 60°C at about the 45th day of heating, assuming the top is adiabatic. This is probably about 20–30 days earlier than observed in the LBT, and some future modeling with a different boundary condition will be done to better simulate the top of the block. Lee (1995a) used an isothermal top boundary set at 60°C, but this results in heat flow downward from the top of the block for the first 30 days in his hydrothermal modeling.

After 50 days of heating, the isotherms are horizontal above the heater zone, and slightly distorted and closer together below the heater zone. The base of the block is about 40–60°C, the top of the block is slightly above 60°C, and the heaters are at about 125°C. Temperatures above the boiling point of water are found extending to about 50 cm above and 30 cm below the heaters, suggesting that a dryout zone nearly 1 m wide could form in the large block at this time. Between the 25th and the 50th day of heating, temperatures at the base of the block have only changed about 10–20°C, while temperatures of the heaters and the top of the block change by about 30°C. The stresses and displacements due to the thermal loading are expected to be higher

above the heaters compared to the region below the heaters. Note that the temperatures beyond about 1 m below the base of the block remain low even after 50 days of heating in the block.

The heaters reach a temperature of about 140°C after 75 days of heating. The temperature 1 m below the base of the block is about 40°C, and temperatures of regions more than about 0.5 m away from the block remain at the original temperature of 20°C. Temperatures remain at about 20°C for regions more than about 2 m below the block. Lee (1995a) shows a similar temperature field in his hydrothermal modeling. The similarity of the temperature fields for the TM and TH modeling assures that appropriate parameters for simulating the LBT were used in the FLAC modeling, and suggests that results of Lee's modeling could be used as input for future FLAC modeling in order to model coupled thermal-hydrological-mechanical processes.

3.5.3.3.1.2 FLAC Mechanical Results

Once the temperature field was determined for different heating times, FLAC was run in the mechanical mode to determine what stresses and displacements developed in each of the four different mechanical models. Each of these runs required about 7000 steps and less than 10 minutes of computer time on the Sun Sparc10. The stresses and displacements differ for different heating times; this section concentrates on results from 75 days of heating.

Figure 3-31(a-e) shows the horizontal (x) displacements, vertical (y) displacements, σ_{xx}, σ_{yy}, and σ_{xy} stresses respectively, after 75 days of heating for the first FLAC model in which the large block was represented as a homogeneous elastic medium having a bulk modulus of 27 GPa and a shear modulus of 14 GPa. This model shows that the maximum horizontal displacement occurs in the heater plane, at the outside edge of the model, and has a magnitude of about 2 mm. Vertical displacement is highest near the top of the block with a magnitude of about 5 mm, decreasing to about 0.5 mm at the base of the block. Vertical displacement contours are approximately horizontal. Both the σ_{xx} and the σ_{yy} plots show that the region around the central heater develops compressive stresses with magnitudes up to about 8 MPa. The σ_{xx} plot also shows compressive stresses of this magnitude developing at the bottom corner of the block, while the σ_{yy} plot shows tensile stresses having magnitudes up to 10 MPa developing at the outer edge of the model in the plane of the heaters. This is significant because this stress level is of the order of the tensile strength of the welded tuff, which is about 6 MPa (see Table 3-7), and much greater than the tensile strength of any fractures in the block, which is estimated to be less than 1 MPa (see Table 3-7). The σ_{xy} plot for this elastic model shows that shear stresses having magnitudes up to about 4 MPa may develop in the plane of the heaters. Plots of stresses for 25 days of heating the elastic model (not shown) are essentially the same as the plots for 75 days. The displacements are slightly lower, with a maximum of 1 mm horizontal displacement after 25 days of heating and a maximum of about 2.2 mm vertical displacement. The displacement contours are similar in shape for 25 days of heating compared to 75 days of heating, except that the very top of the block is slightly less disturbed. It is important to note that the displacements and stresses develop comparatively early in the heating, because the rates of temperature changes are higher early in the 75 days of heating.

The second FLAC mechanical model represented the large block as a homogeneous elastic medium having the same coefficient of thermal expansion but lower elastic moduli than the first model. A value of 2.7 GPa was used for the bulk modulus, and a value of 1.4 GPa was used for

the shear modulus. Initial results of mechanical measurements made in the laboratory for 1 1-m blocks of tuff from Fran Ridge suggest that these values may be appropriate for representing the highly fractured mass of rock that issuch as the large block. Horizontal and vertical displacements (not shown in the figure) found after 75 days of heating for this second model were identical to those found for the first model; this indicates that the thermal expansion coefficient controls displacements. For linear elasticity, it is expected that stresses for this second model should simply be reduced by an order of magnitude from those found for the first elastic model. Results of this modeling (not shown in the figure) found no significant compressive stresses or shear stresses developing anywhere in the model, and very small tensile stresses (<2 MPa) developing in the heater plane at the outer edge of the model. In this second model, the block is so compliant that it cannot build up significant stresses. An important implication of these results is that the presence of many fractures in the large block prevents stress from building to the high levels predicted for a homogeneous, elastic block.

To simulate the effect of discrete fractures on the thermomechanical behavior, the third and fourth mechanical models represented the large block as an elastic medium containing one horizontal set of grid elements and one vertical set of grid elements in which the properties were changed to simulate a horizontal and a vertical fracture. In the third model, these sets of grid elements were represented as elastic media with bulk and shear moduli lowered by one order of magnitude with respect to the rest of the block. The fourth model used the ubiquitous joint model for these elements. Figure 3-32 shows these elements that represent fractures, located in a horizontal line about 0.5 m below the top of the block and a vertical line about 1 m from the center of the block.

Stress and displacement results for the third model, for 75 days of heating, are shown in Figure 3-33(a-e). The σ_{xx} plot is nearly the same as that for the original elastic model. Most of the compressive stress near the central heater (4–6 MPa) and most of the tensile stress at the outer edge of the model in the heater plane (>8 MPa) are already present after one day of heating (not shown). The σ_{yy} plot is almost the same as that for the first elastic model, except that the stress field is slightly distorted by the vertical fracture zone. The σ_{xy} plot shows that shear stresses are very low, below 2 MPa, for this model. The horizontal displacements are nearly the same as those found in the first elastic model, but the vertical displacements show contours that are offset slightly along the vertical fracture. Magnitudes of maximum displacements are the same for this model and the first elastic model.

The fourth model, which used the ubiquitous joint model to represent the horizontal and vertical fractures, had displacement results (not shown in the figure) that were nearly the same as those found usingin the third mechanical model—i.e., horizontal displacements the same as in the original elastic model and vertical displacements offset a small amount along the vertical fracture. The σ_{xy} results (not shown) were about the same for the third and fourth models. Figure 3-34(a,b) shows However, the σ_{xx} plot and the σ_{yy} plot for the fourth model. These differ from results for the third model, as shown in Figure 3-34(a,b). Stresses are lower but are more affected by the presence of the vertical fracture. These results imply that the presence of fractures in the block has a strong affect effect on the distribution as well as the magnitudes of stresses.

3.5.3.3.2 ABAQUS™ Modeling Results

This section presents temperatures, normal stresses, and normal displacements for 3-D ABAQUS™ simulations at 10, 20, and 60 days. The results are presented graphically as perspective diagrams of the large block. The diagrams show the perspective of looking at the outside of the block from the point (1,2,2). Only one-quarter of the block is displayed, and the two back surfaces are symmetry planes. Note that the back surface perpendicular to the long axis of the heaters corresponds to the 2-D cross-section modeled using FLAC. The figures showing the 3-D views are grouped into two sets. Figure 3-35 (a-c) shows predicted contours of temperature, and normal stresses at 10, 20, and 60 days, respectively. In these figures, normal stresses on the faces perpendicular to the 1, 2, and 3 axes are denoted by σ_{11}, σ_{22}, and σ_{33}, respectively.

These results show that the predicted temperature field is approximately one-dimensional due to the insulated boundaries along the sides. The top of the block, which is also an insulated boundary in the model, reaches a temperature of about 65°C after 60 days. An alternative boundary condition for the top of the block would be a boundary in which the heat flux out of the top of the block would be proportional to the difference between the block and ambient air temperature (nominally, 20°C).

The largest of the normal stresses is the vertical stress, σ_{33}, at the outside corner of the block near the heater plane. The largest value shown is about 14 Mpa, and it occurs at 10 days. This is consistent with the 2-D analysis that shows that the higher stresses occur early in the test. The maximum stress decreases to about 10 MPa at 60 days because the thermal gradients decrease as the block becomes more uniformly heated. The horizontal stresses parallel and perpendicular to the heaters are almost an order of magnitude smaller than the vertical stress.

The second set of figures shows displacements that are predicted for the block at 10, 20, and 60 days (Figures 3-36, a-c). In each of these figures the wire net diagrams in the upper left corner presents total displacements that have been exaggerated for purposes of clarity. Displacements in the 1, 2, and 3 directions are given by U1, U2 and U3, respectively. The wire-net diagrams show how the block bulges in all directions, with the largest horizontal displacements normal to the vertical side in the heater plane. The horizontal displacements show at early times an approximate cylindrical shape about a horizontal axis orthogonal to the displacement component, but they become more planar at longer times. Similar patterns are seen in the 2-D FLAC analysis for the purely elastic case (Figure 3-31, a,b).

3.5.3.4 Discussion

The elastic model in 2-D and 3-D produced the highest stress levels, and these occurred during the first 10 days of heating. Tensile stress levels that approach the tensile strength of Topopah Spring tuff were predicted in the plane of the heaters and in the vertical direction in both the 2-D and 3-D cases for a homogeneous elastic block.

These simulations assumed nominally stress-free boundaries on the exposed faces of the block, and as a result the displacements (and strains) are dominated by the thermal expansion of the rock mass. The predicted temperature fields agree well with those predicted by Lee (1995a)

using a code that incorporates a more sophisticated TH model. It is important to note that the LBT design incorporated a retention frame that surrounded the sides of the block and applied a nominal confining stress between 0.2 and 0.3 MPa on the block. This retention frame also applied a shear stress on the sides of the block that opposed the tension generated in the vertical direction and reduced the level of tensile stress in the block in this direction, but the amount of reduction is difficult to estimate.

Two simulations were conducted in which discrete fractures present in the large block were simulated, and lower levels of stress were predicted in these simulations, indicating that the presence of compliant fractures may reduce the stress levels.

3.5.3.4.1 Comparison of 2-D and 3-D Simulations

The 2-D, plane strain, FLAC model was constructed in a plane orthogonal to the heater holes. The thermal predictions made with this code show a 2-D temperature field near the heaters at early times. At later times, the code predicts a temperature field that is nearly one-dimensional because all the walls are adiabatic. The temperature fields in the 3-D model were generated using 100°C constant-temperature heaters. This approach produced very similar temperature fields to those predicted by the 300-W constant-power heaters used in the 2-D FLAC model. For example, the temperature at the top of the block is approximately 65°C after 60 days in the 3-D model and approximately 70°C after 55 days (not shown in the figure) in the 2-D model.

The differences are greater between the 2-D and 3-D mechanical models. The plane strain approximation used in the 2-D model assumes that the length of the heater direction is long compared with the height and width of the block. Further, the plane strain model does not incorporate the stress-free boundary faces parallel to the model plane. The plane strain model generates a large, compressive normal stress in the heater direction to suppress the thermal expansion in that direction.

Despite these caveats and the differences in the thermal models, the plane strain results and those from the mid-plane perpendicular to the heaters of the 3-D model are very similar because this plane is a symmetry plane on which the normal displacement is zero in both the 3-D and 2-D models. Additional analysis not included here shows that in this plane the 3-D model predicts that both σ_{11} and σ_{33} are compressive near the center of the block, just as they are in the 2-D model. In fact, the detailed contour patterns and approximate magnitudes for this plane in the 3-D model match those of the 2-D plane strain model rather closely. However, the patterns do not project to the outer surfaces of the block.

3.5.3.4.2 Conclusions

The main results of the modeling can be summarized as follows:

The thermal-mechanical FLAC and ABAQUS™ modeling produced temperature fields similar to that the TH model of Lee (1995a). who used a code which contains a more sophisticated thermal-hydrologic model. This suggests that the FLAC and ABAQUS™ codes could be used with a TH model to better investigate coupled processes.

- Most of the thermal stress develops in the first 10 days of heating, when the rate of temperature change is highest.

- Stress levels are highest in the heater plane and at the bottom outside edge of the block. Tensile stresses are highest at the surface of the block in the plane of the heaters, are oriented in the vertical direction, and may be capable of causing tensile fracture. However, results show that the presence of fractures in the large block may reduce the levels of stress in the block below those predicted for a purely elastic continuum. High tensile stresses may still occur locally in the plane of the heaters.

- Displacements are highest at the top of the block and at the outside edge of the block in the heater plane, with magnitudes on the order of a few millimeters for both horizontal and vertical directions.

The 2-D and 3-D modeling is complementary. Results agree for the elastic constitutive model in the symmetry plane at the center of the block. The 2-D modeling was faster and was useful for exploring effects of different constitutive models, but was unable to simulate the outside face of the large block where stresses are highest. This is because the plane strain assumption is equivalent to assuming that the 2-D model lies at the center of the block. Note that most of the instrumentation in the LBT will be located on the outside surface of the block. The 3-D modeling required an order of magnitude more in computer time but was able to estimate maximum stresses and displacements everywhere in the block's volume.

3.5.4 Post-test Characterization

Post-test characterization activities included drilling and coring and analyzing the post-test cores. The main purpose of the post-test analyses was to assess the effect of the test on the changes in mineralogy of the block. The results of the post-test mechanical analysis are presented in Section 7. The results of the post-test mineralogical analyses are presented in Section 8.

3.5.4.1 Boreholes for Post-test Characterization

Nineteen HQ-sized, core-drilled boreholes and one 10-in overcore of an existing heater borehole were dry-drilled to provide samples for post-test characterization of the LBT. The characteristics of each borehole are listed in Table 3-8. Most of these boreholes were drilled in two vertical fans. One fan of holes was drilled from the west side of the block and the other from the north side. The layouts of these boreholes are shown in Figure 3-37 and Figure 3-38.

Prior to drilling the boreholes, all the collar locations (except the overcore) were located and marked; the overcore is located concentrically with the heater hole EH-4, which served as a pilot hole for the drilling.

Of the 10 holes drilled into the west face of the block, nine were drilled in a fan-like pattern in a vertical plane that intersected borehole LBL-1. This borehole was intersected to provide core samples that might contain microbes placed in LBL-1 prior to the start of heating.

The tenth borehole drilled from the west side of the block (PTC-10) was oriented in the horiztontal plane and approximately 16° clockwise from the vertical fan. This borehole was

designed to intersect borehole LBL-2 and to obtain core in the horizontal plane at the level above the heaters in the block.

Nine boreholes were also drilled into the north face of the block. Eight of these were oriented north–south and in a fan-shape pattern in a vertical plane aligned with vertical borehole TN-3. Aligning these holes with borehole TN-3 was done to obtain samples of grout used in the borehole that had been involved with rock/water interaction so that the effect of the THC environment on the grout could be determined. The ninth borehole on the north side was drilled at 16° to the east of north and in the horizontal plane to penetrate borehole TM-2.

All core boreholes extended through the block so that edge effects, if any, could be observed. As-built surveys of the boreholes and video logging of each borehole were completed.

Table 3-8. The xyz Coordinates (with Respect to the Southwestern Corner on Top of the Block) of the Collar, and Other Characteristics of the Post-test Holes

Borehole ID #	X (m)	Y (m)	Z (m)	Face	Orientation	Angle	Length (m)
UE25-FR-PTC-1	1.22	3.05	-2.29	N	N	0°	3.05
UE25-FR-PTC-2	1.22	3.05	-2.02	N	N	+10°	3.1
UE25-FR-PTC-3	1.22	3.05	-2.55	N	N	–10°	3.1
UE25-FR-PTC-4	1.22	3.05	-1.73	N	N	+20°	3.2
UE25-FR-PTC-5	1.22	3.05	-2.84	N	N	–20°	3.2
UE25-FR-PTC-6	1.22	3.05	-1.41	N	N	+30°	2.82
UE25-FR-PTC-7	1.22	3.05	-3.76	N	N	–44°	4.27
UE25-FR-PTC-8	1.22	3.05	-1.01	N	N	+40°	1.57
UE25-FR-PTC-9	1.22	3.05	-2.29	N	N16W	0°	3.32
UE25-FR-PTC-10	0	1.83	-1.10	W	W	+38°	1.78
UE25-FR-PTC-11	0	1.83	-1.30	W	W	+33°	1.39
UE25-FR-PTC-12	0	1.83	-1.51	W	W	+27°	3.33
UE25-FR-PTC-13	0	1.83	-1.73	W	W	+20°	3.25
UE25-FR-PTC-14	0	1.83	-1.91	W	W	+14°	3.14
UE25-FR-PTC-15	0	1.83	-2.26	W	W	+1°	3.05
UE25-FR-PTC-16	0	1.83	-2.55	W	W	–10°	3.1
UE25-FR-PTC-17	0	1.83	-2.84	W	W	–20°	3.25
UE25-FR-PTC-18	0	1.83	-3.35	W	W	–35°	3.73
UE25-FR-PTC-19	0	1.83	-2.18	W	W	+4°	3.06
UE25-FR-PTC-19a	0	1.83	-2.29	W	E16S	0°	3.32
UE25-FR-PTC-OC-1	3.05	2.13	-2.74	E	W	0°	3.05

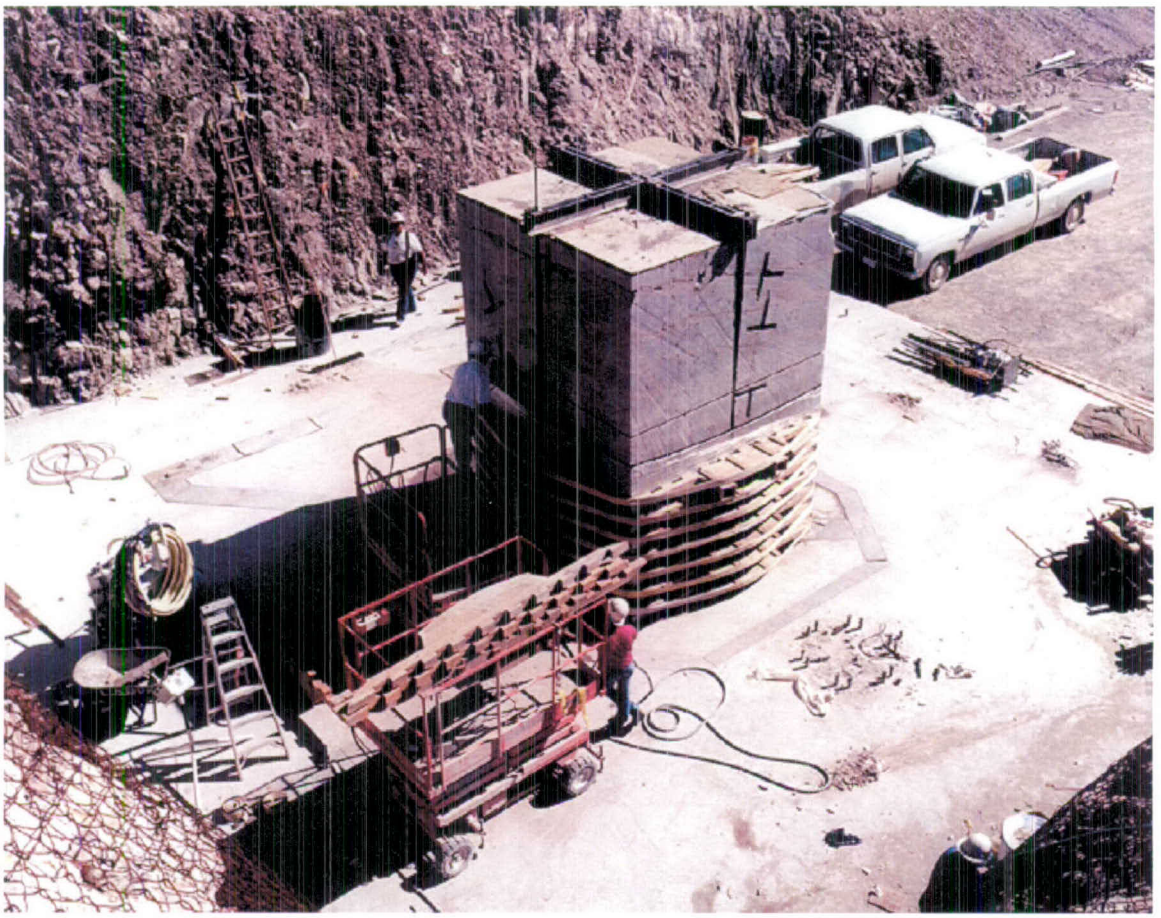

Figure 3-1. The Topopah Spring Tuff Block of the LBT

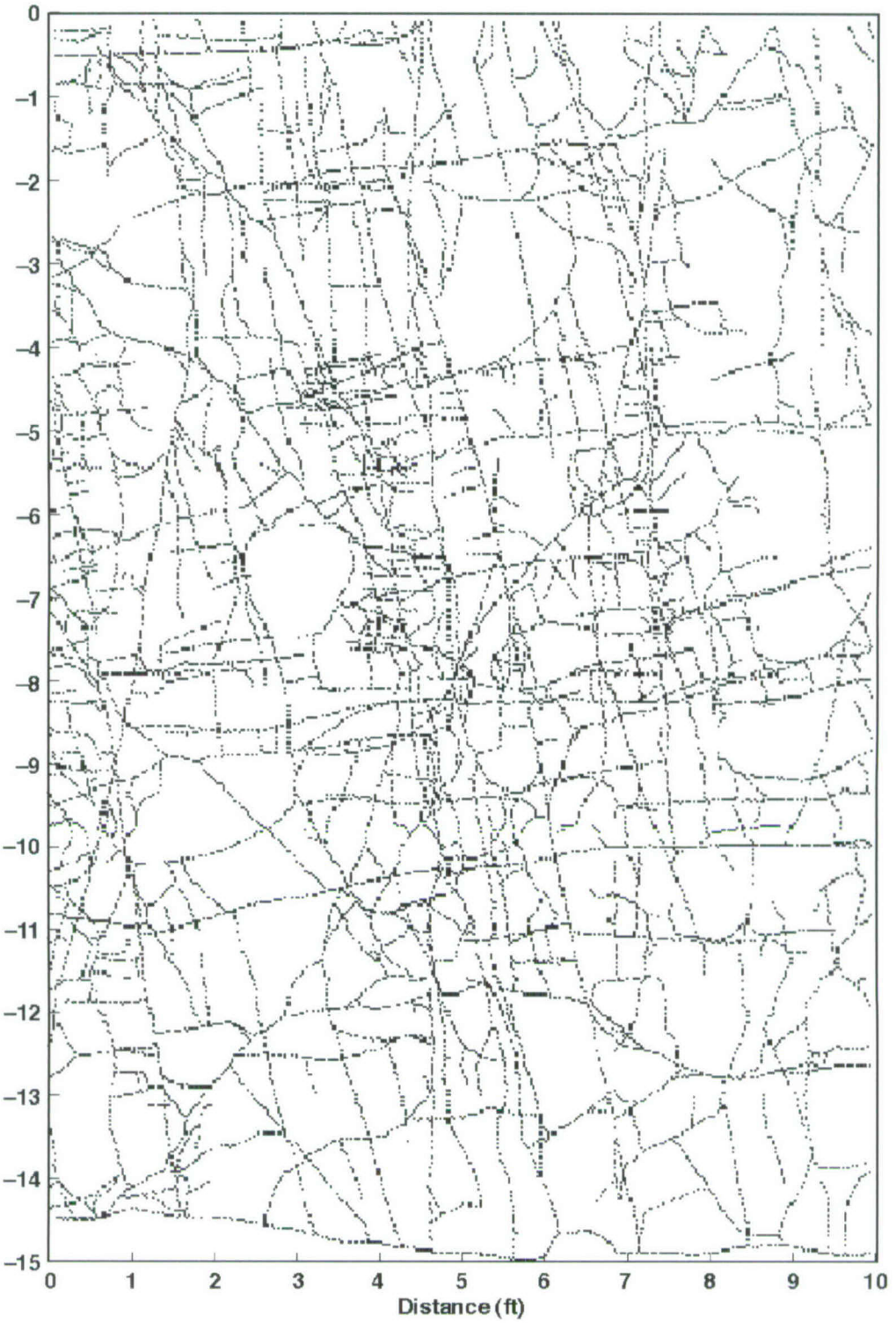

Figure 3-2. Fractures on the North Face of the Block

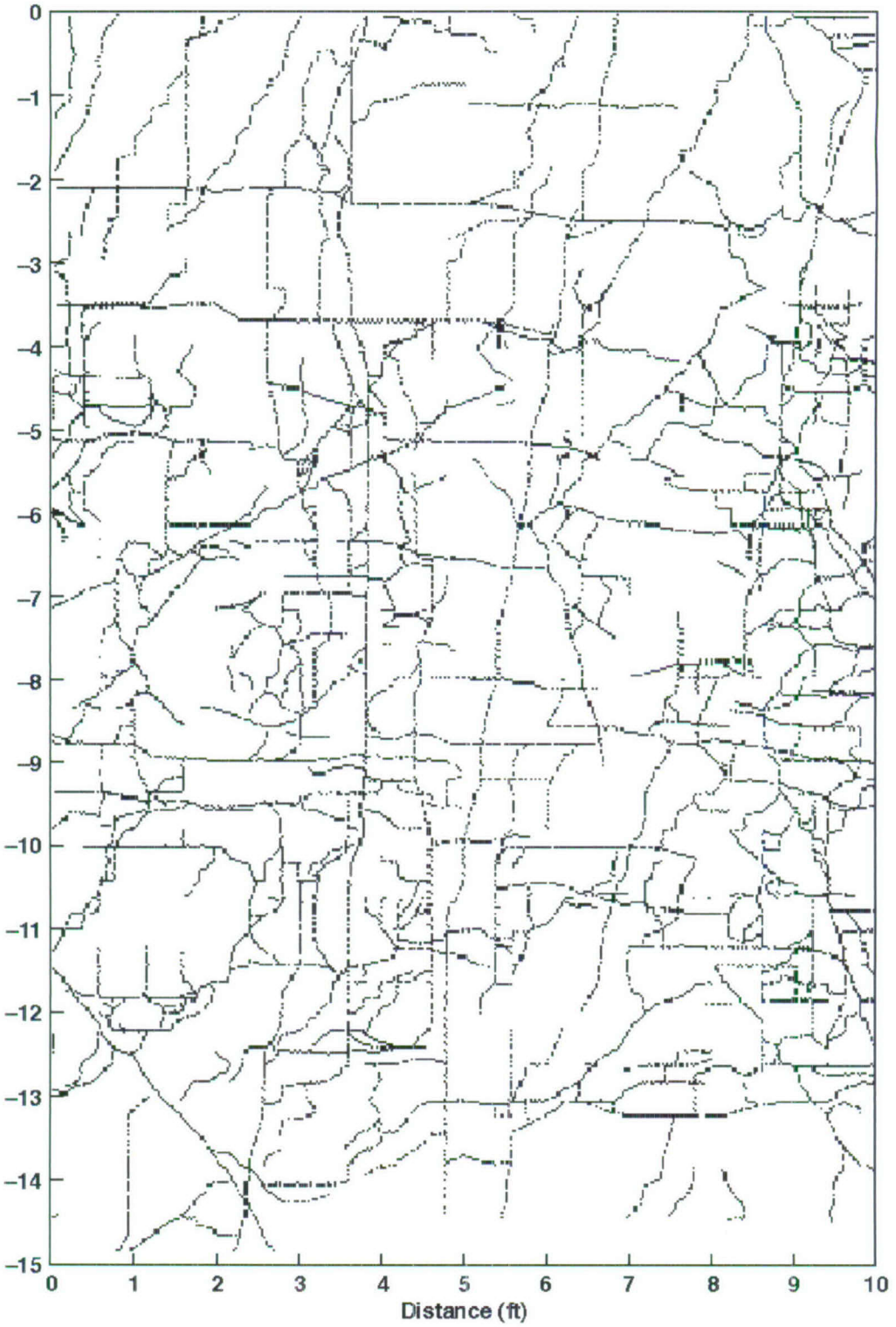

Figure 3-3. Fractures on the East Face of the Block

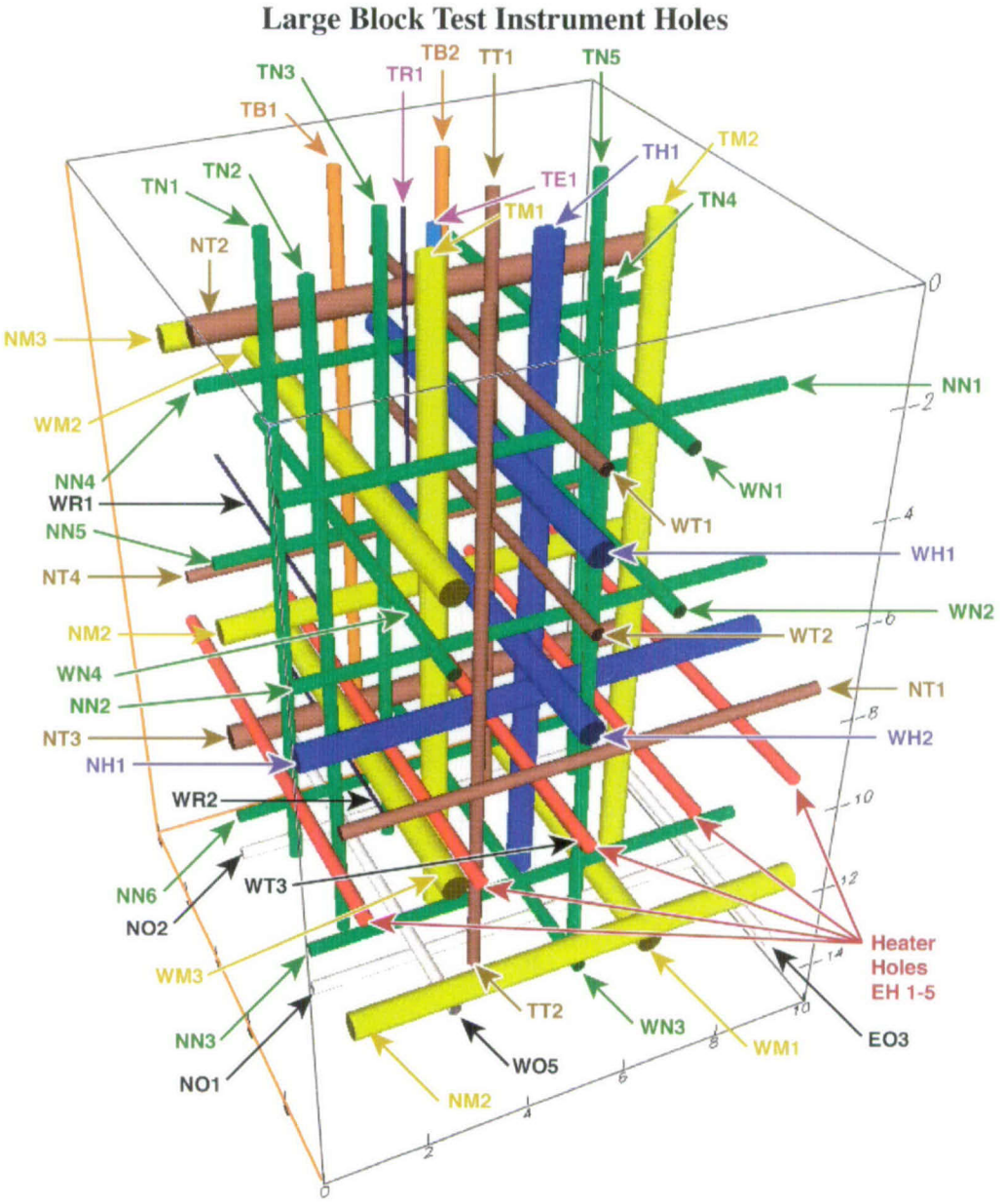

Figure 3-4. A Diagram Showing All Holes in the Block of the Large Block Test

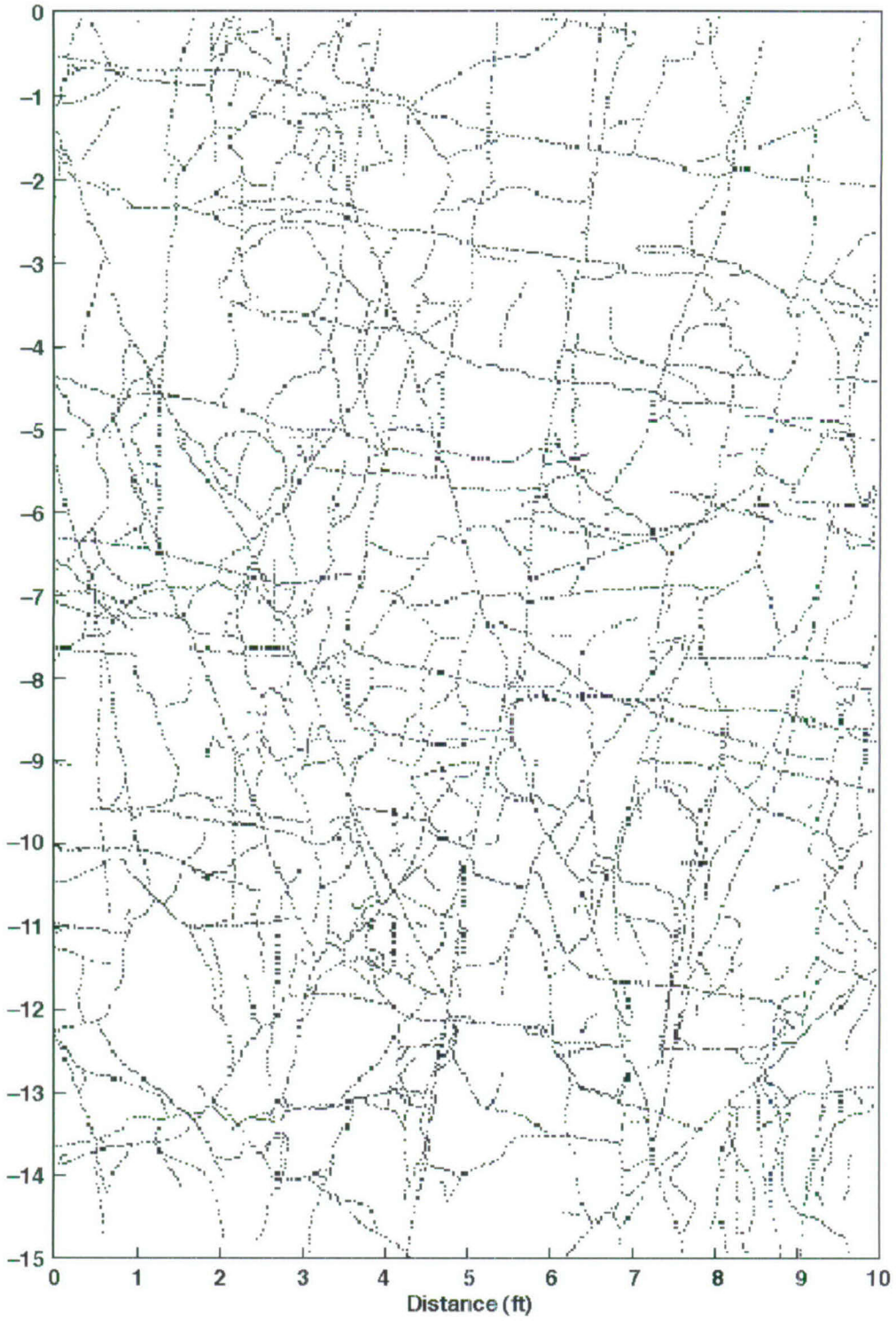

Figure 3-5. Fractures on the South Face of the Block

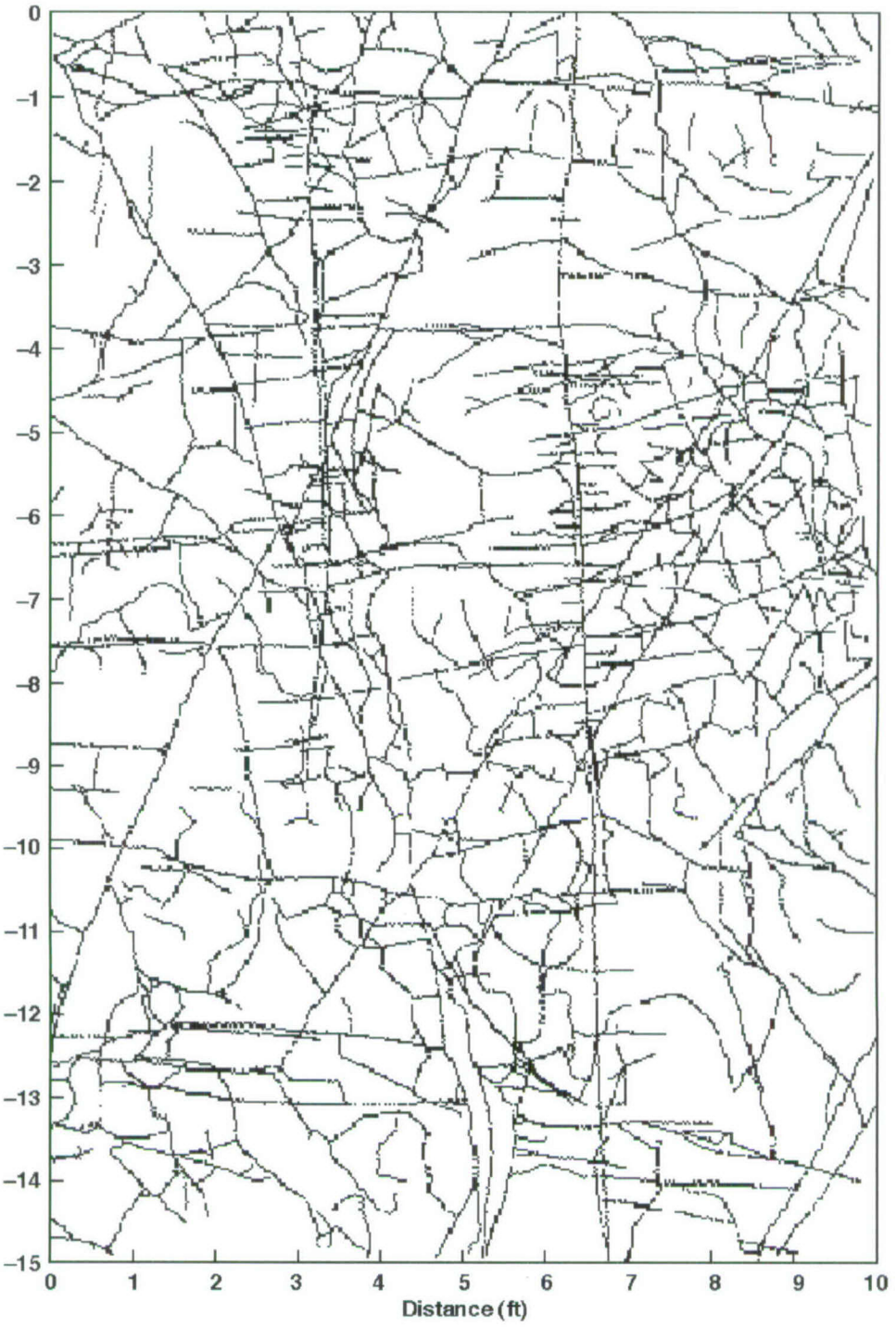

Figure 3-6. Fractures on the West Face of the Block

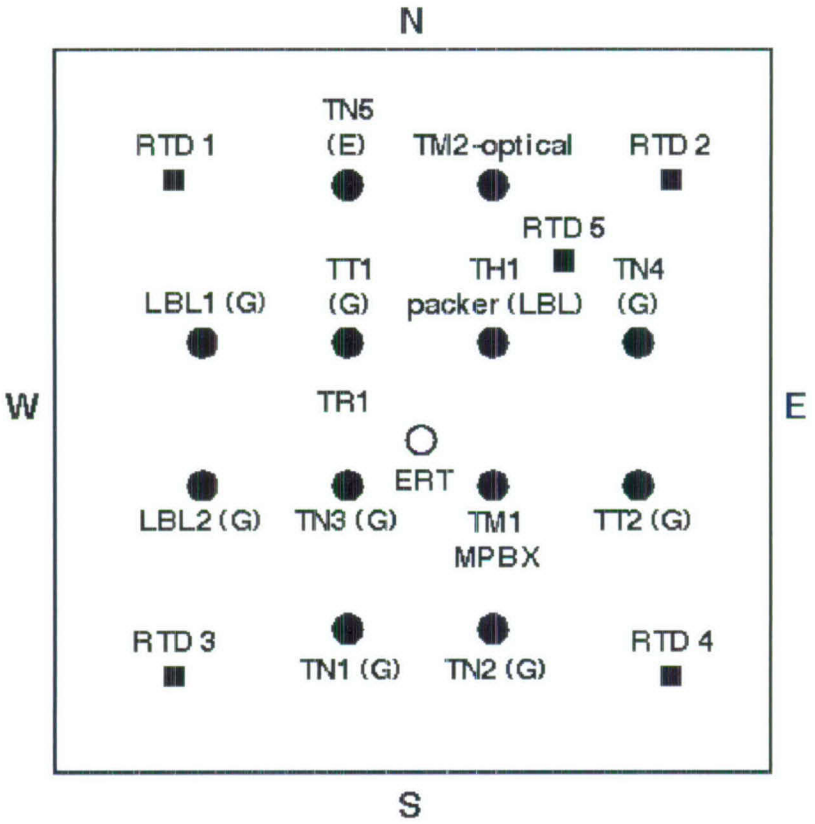

TT# – Temperature measurements – borehole
RTD#– Temperature – Surface mounted RTD
LBL# – Open holes to be used by LBL for air and then grouted
TN# – Neutron holes to be lined and grouted
TR1 – REKA probe – to be grouted
TM# – Mechanical – MPBX borehole

Figure 3-7. Instrument Holes on Top of the Block

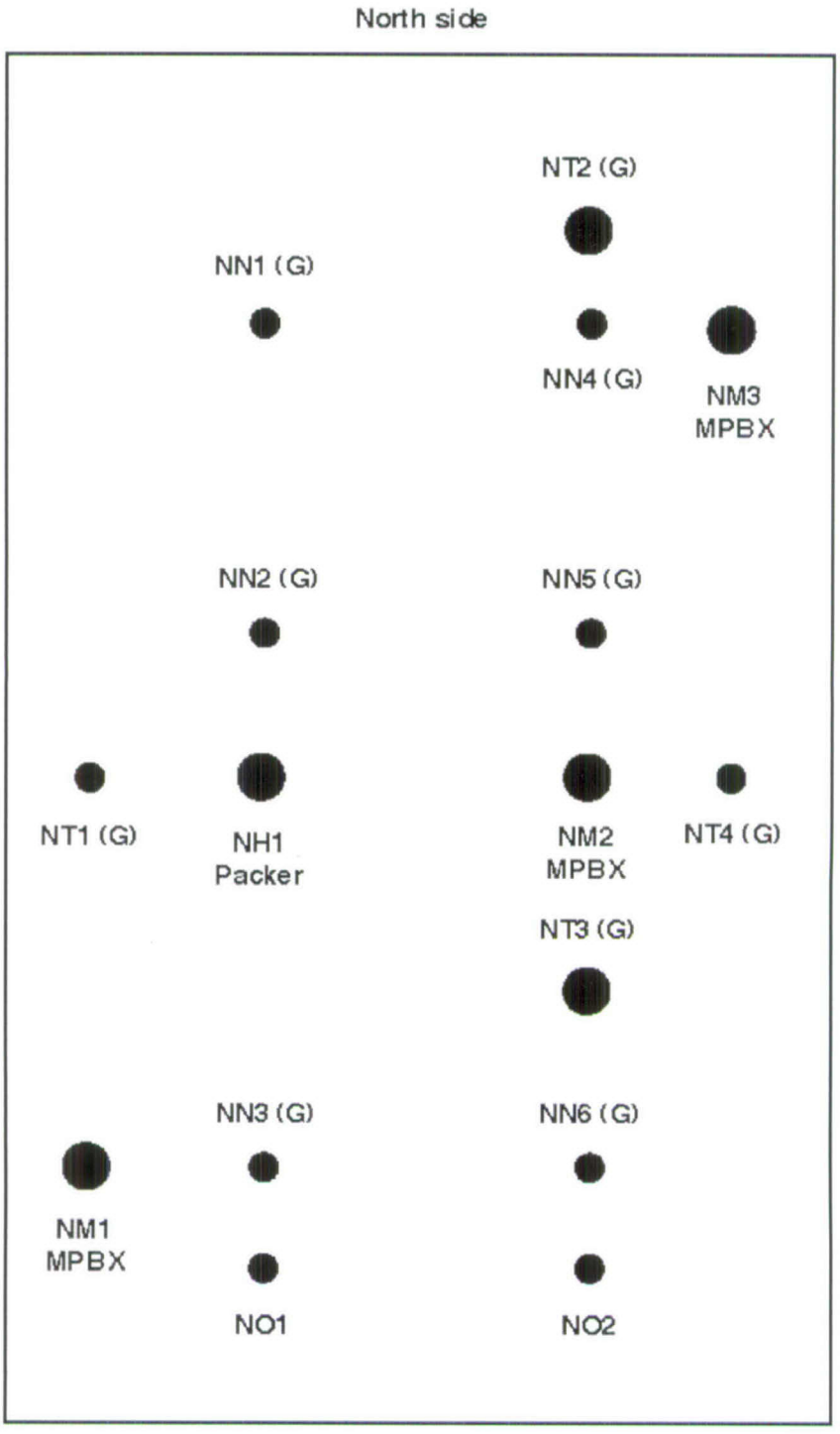

NN# – North side neutron hole – to be lined and grouted
NT# – North side temperature (RTD bundle) all to be grouted
NM# – North side mechanical
NO# – North side observation hole
NH# – North side hydrology – packer assembly to be installed

Figure 3-8. Instrument Holes on the North Face of the Block

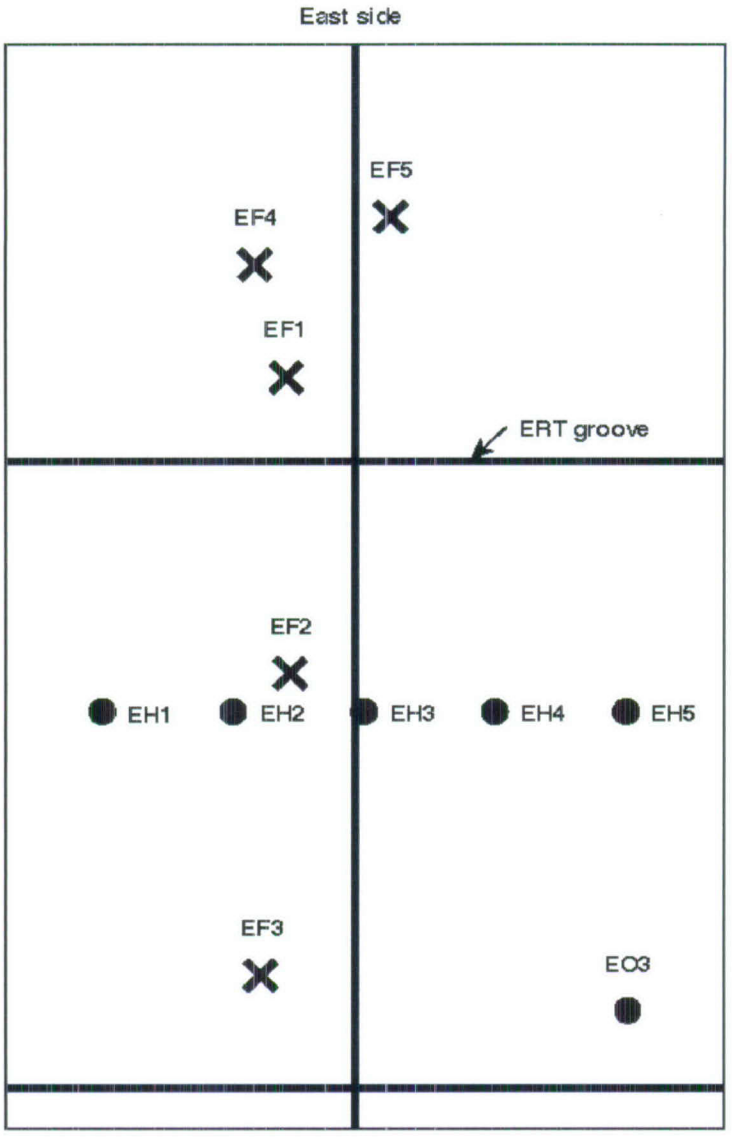

EH# – East heater hole (heater assembly w/ERT)
EO – East observation
EF# – Fracture monitors

Figure 3-9. Instrument Holes on the East Face of the Block

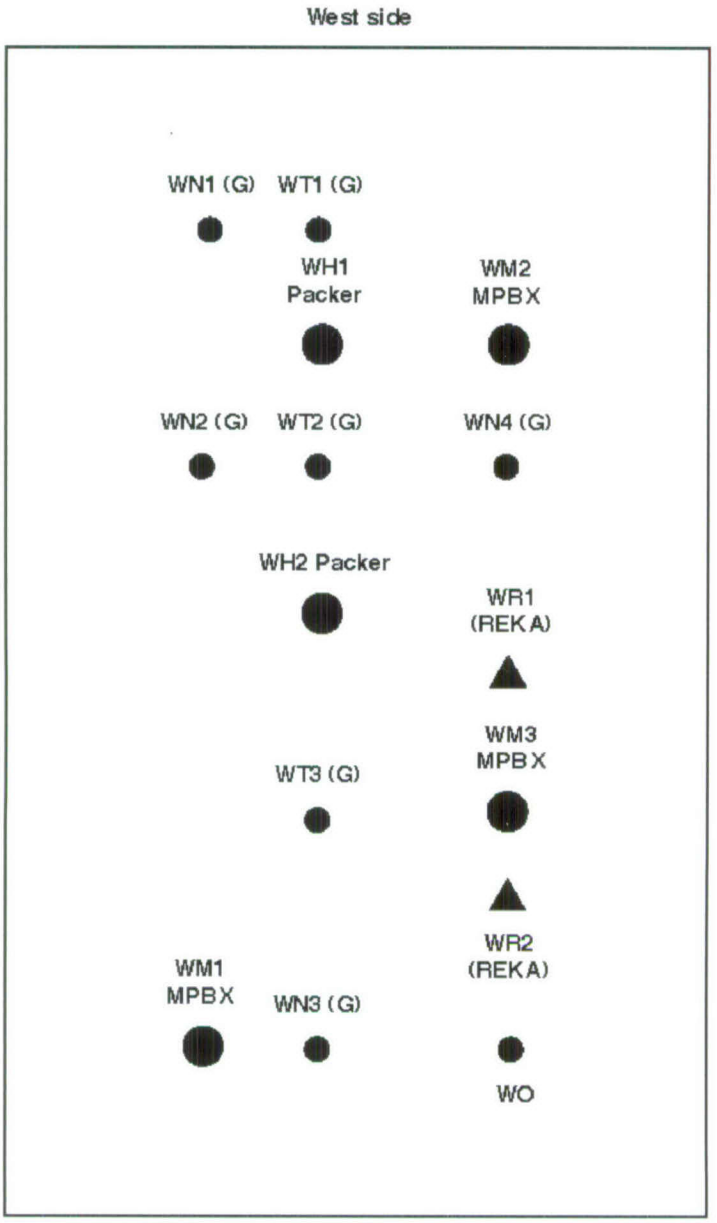

WN# – West side neutron hole – to be lined and grouted
WT# – West side thermal (RTD bundle) to be grouted
WH# – West side horizontal – packer assembly to be installed
WM# – West side mechanical (MPBX) hole – to be grouted
WO# – West side observation hole

Figure 3-10. Instrument Holes on the West Face of the Block

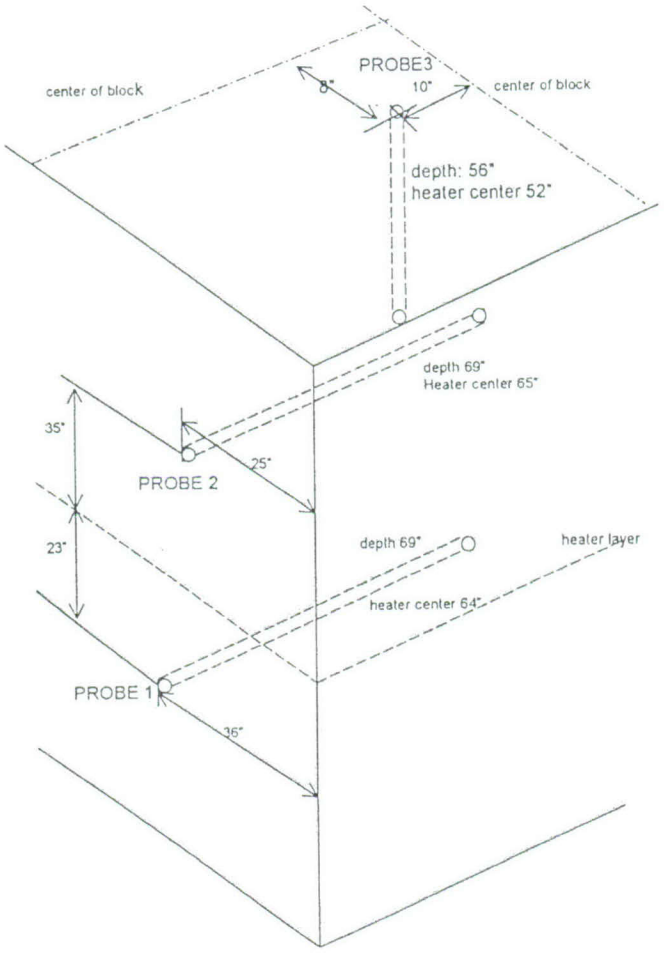

Figure 3-11. Three REKA Probe Locations in the Large Heated Block

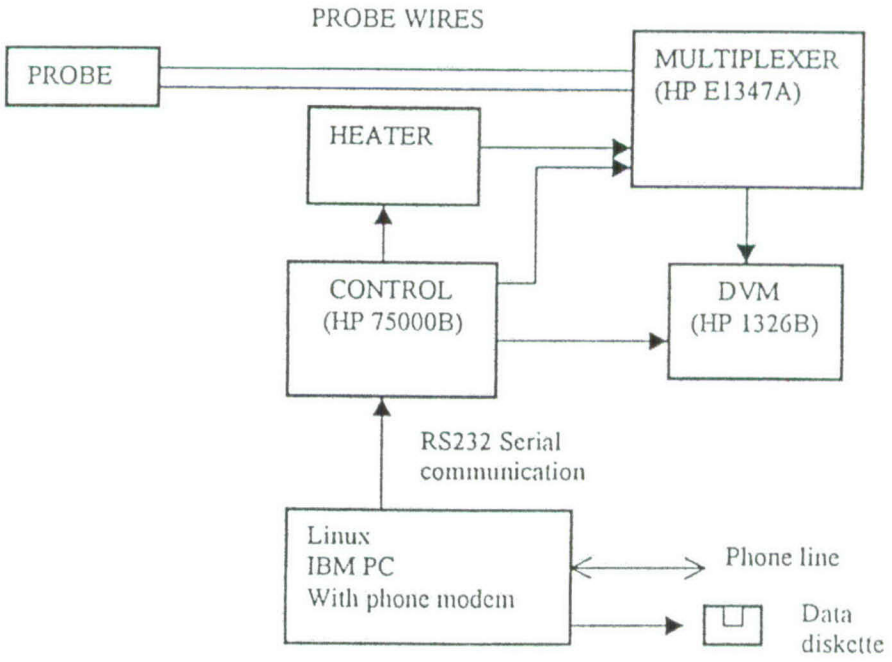

Figure 3-12. Measurement Flow Chart for One Probe

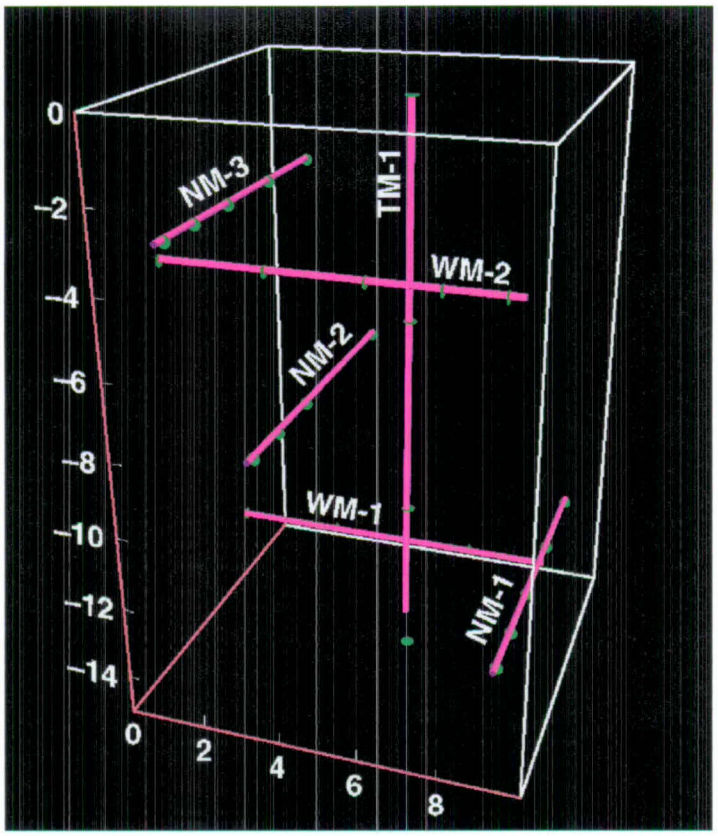

NOTE: Anchors are shown as discs in each hole.

Figure 3-13. The MPBX Holes in the LBT

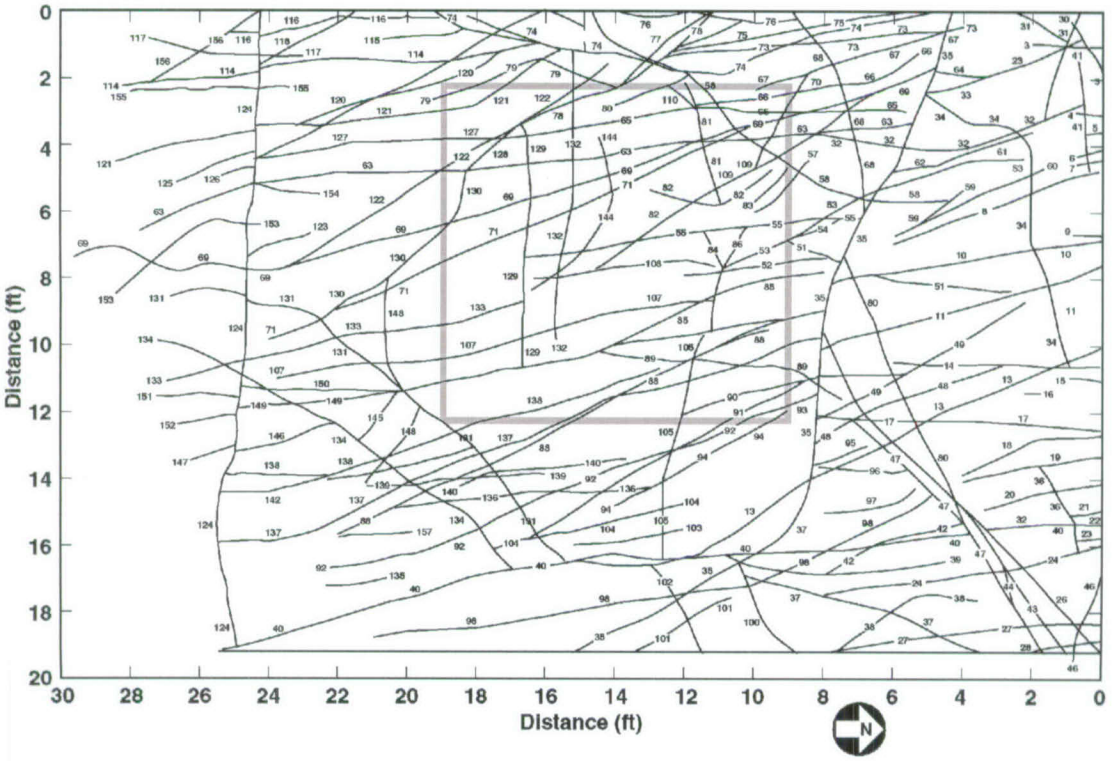

Figure 3-14. Initial Fracture Mapping at Fran Ridge

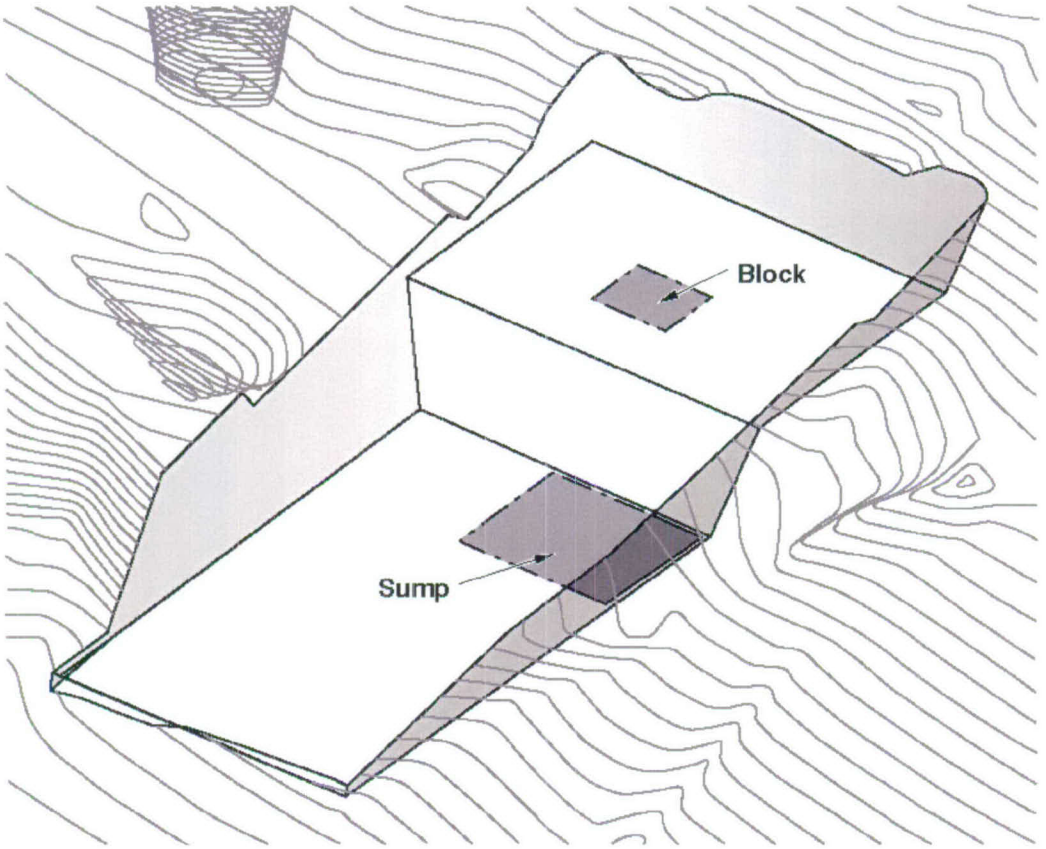

Figure 3-15. Excavation of Level Surface

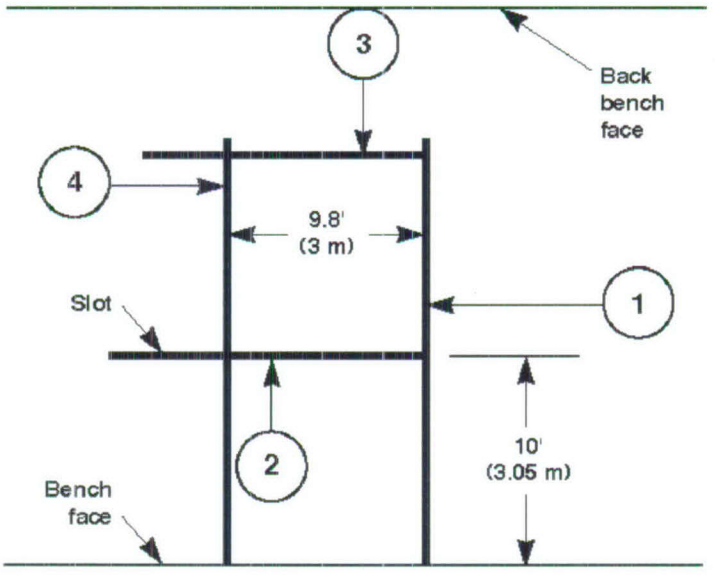

Figure 3-16. Slots for Block Isolation

Figure 3-17. Partial Excavation of the Block

Figure 3-18. Drilling Rig Mounted on a Steel Platform to Drill Horizontal Boreholes

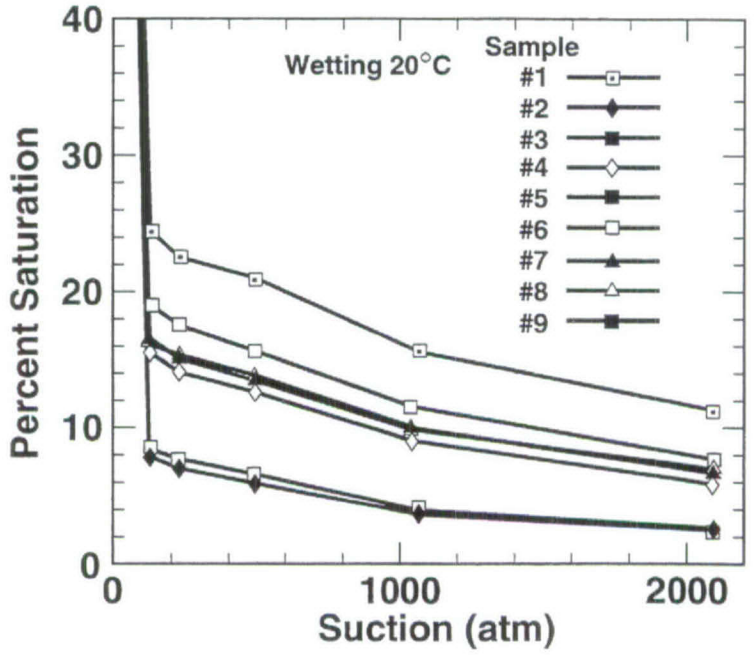

NOTE: Samples 1-3 were taken from USW H-1 core; samples 4-9 were taken from Fran Ridge outcrop.

Figure 3-19. Percent Saturation as a Function of Suction Potential at 20°C for Nine Topopah Spring Tuff Samples During Wetting Phase

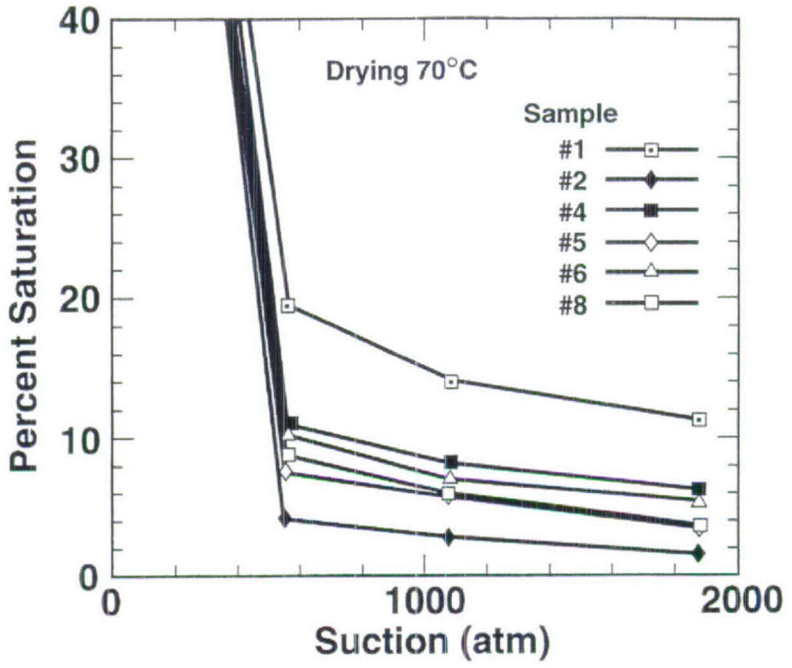

NOTE: Samples 1-2 were taken from USW H-1 core; samples 4-8 were taken from Fran Ridge outcrop.

Figure 3-20. Percent Saturation as a Function of Suction Potential at 70°C for Six Topopah Spring Tuff Samples During Drying Phase

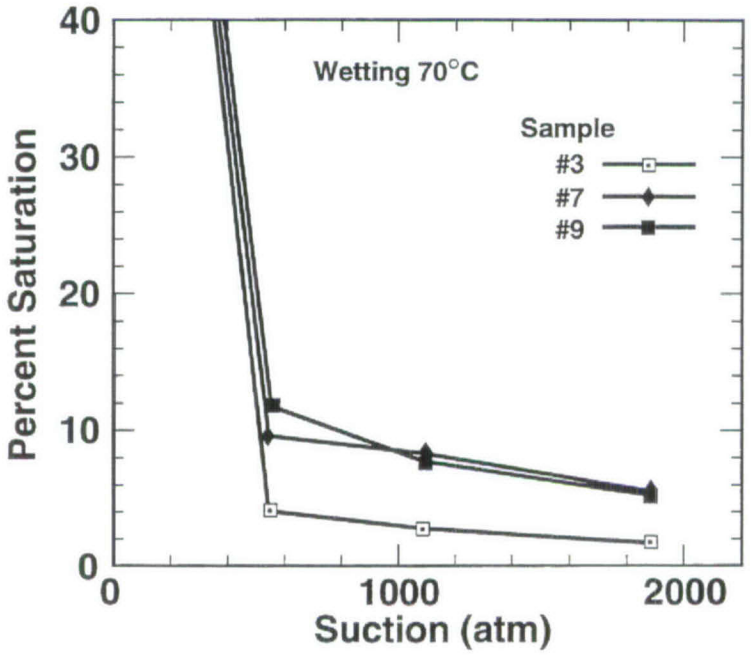

NOTE: Sample 3 was taken from USW H-1 core; samples 7 and 9 were taken from Fran Ridge outcrop.

Figure 3-21. Percent Saturation as a Function of Suction Potential at 70°C for Three Topopah Spring Tuff Samples During Wetting Phase

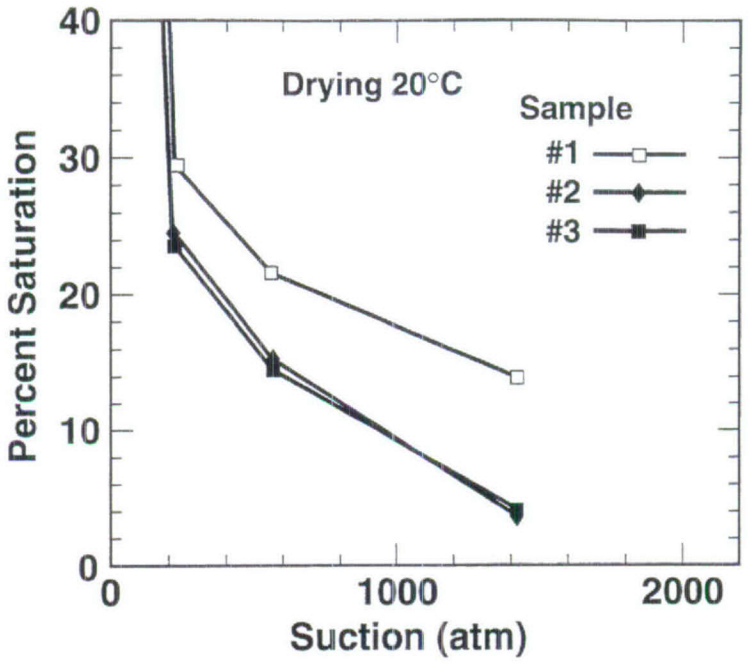

Figure 3-22. Percent Saturation as a Function of Suction Potential at 20°C for Three Topopah Spring Tuff Samples During Drying Phase

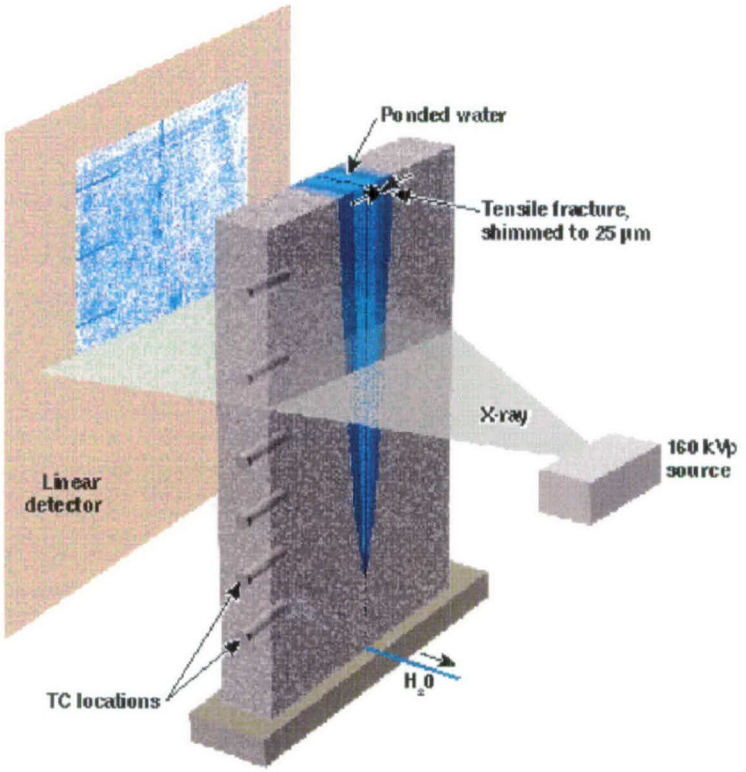

Figure 3-23. Schematic Diagram Showing the Set-up of Using X-ray Radiography to Investigate Fracture Flow and Matrix Imbibition

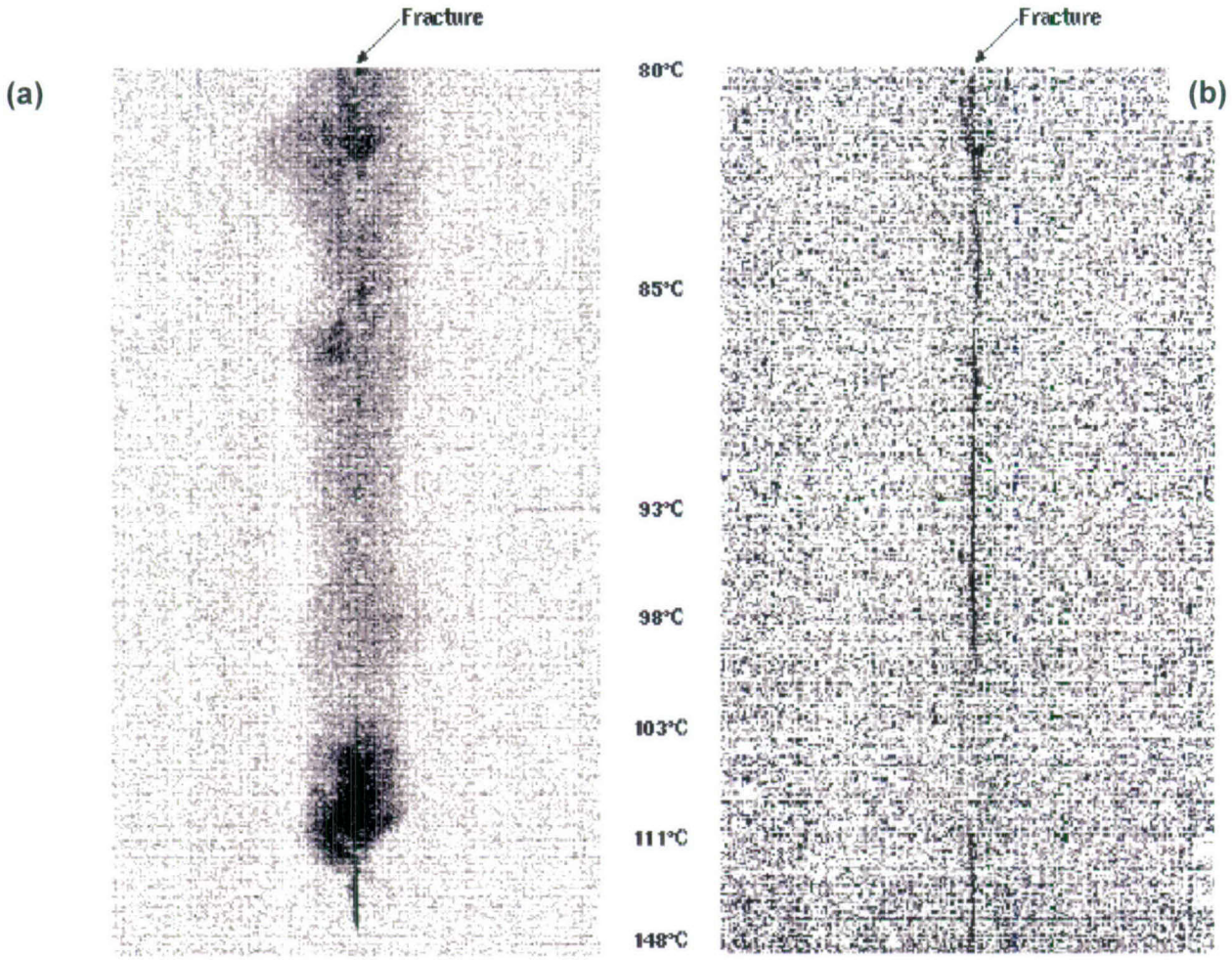

NOTE: Thermal gradient is indicated between the images. The difference between these two experiments was the height of the water column, 0.26 and 0.46 m for (a) and (b) respectively. The difference in the water head was enough to force flow through the boiling zone without causing much imbibition in (b).

Figure 3-24. Difference Images of Experiment 5 (a) and 6 (b) at 7.2 and 0.67 Hours Respectively After Flow Was Initiated

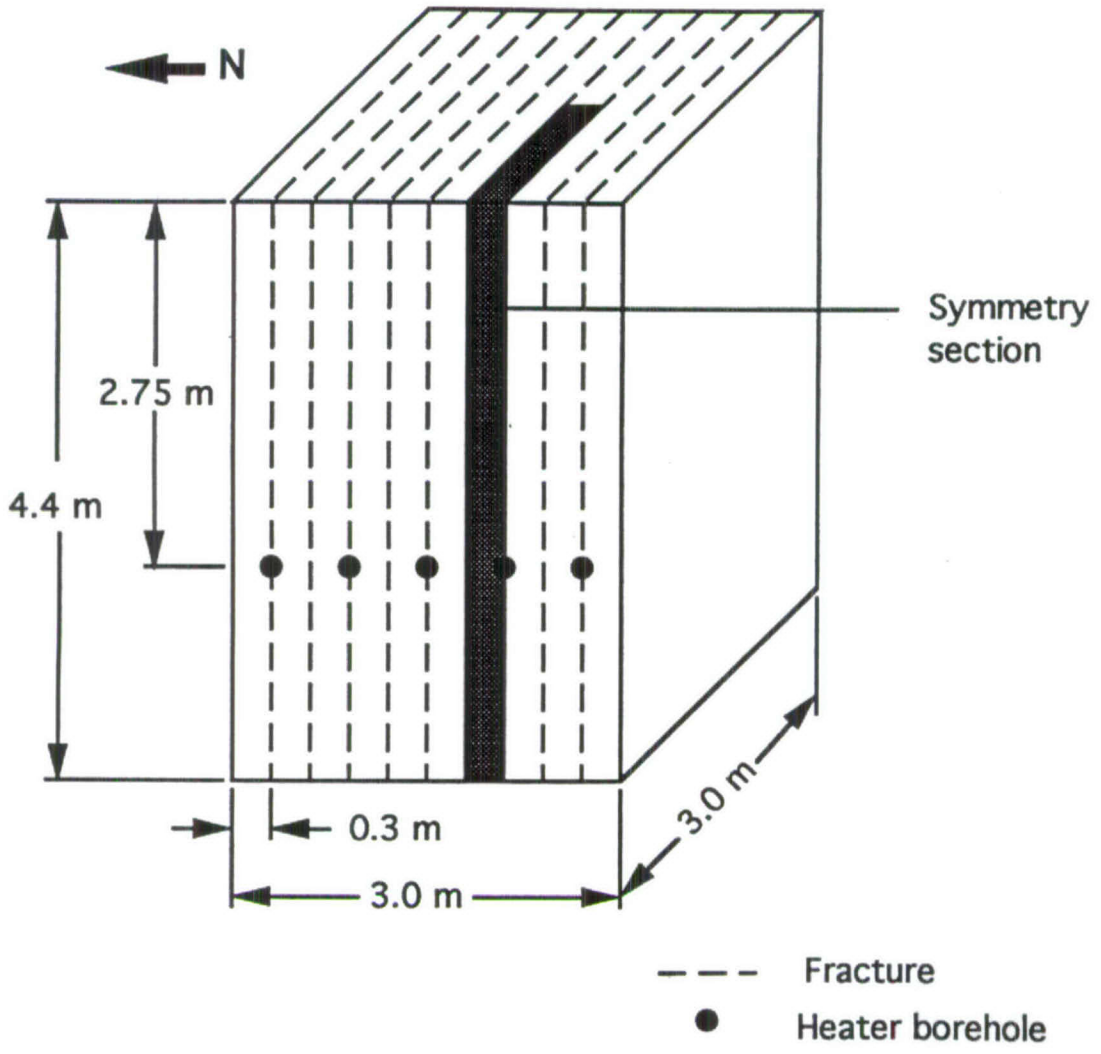

NOTE: The shaded area is the 1/20 symmetry section modeled.

Figure 3-25. Schematic of Large Block Showing Locations of Fractures and Heater Boreholes

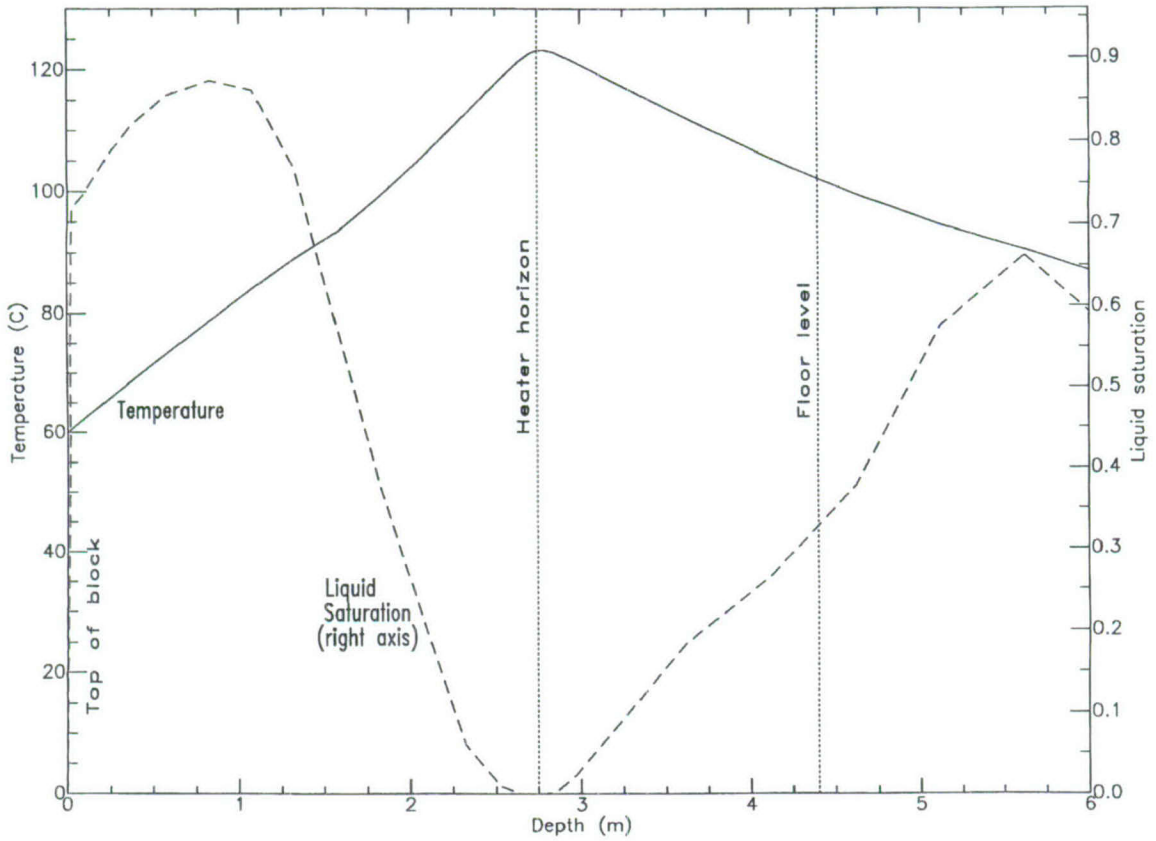

Figure 3-26. Predicted Temperature and Water Saturation Profiles Along a Vertical Line Through the Matrix at One-year Heating

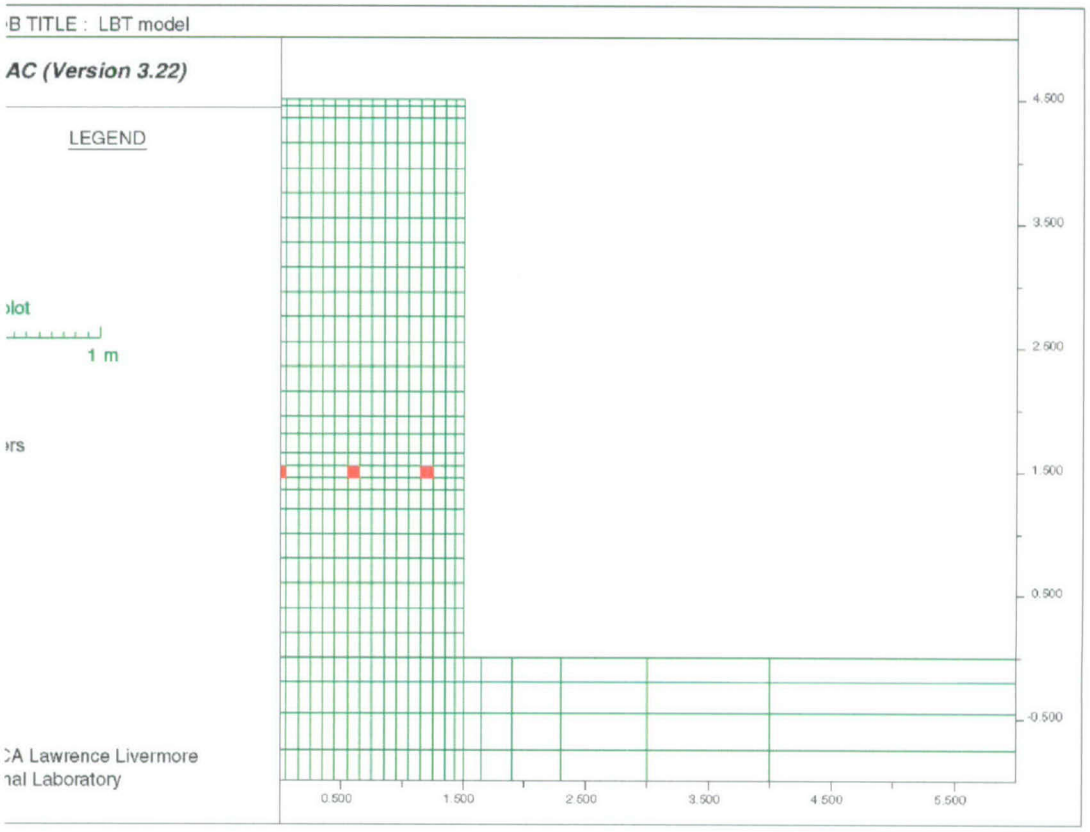

Figure 3-27. Grid of the FLAC LBT Model

(a)

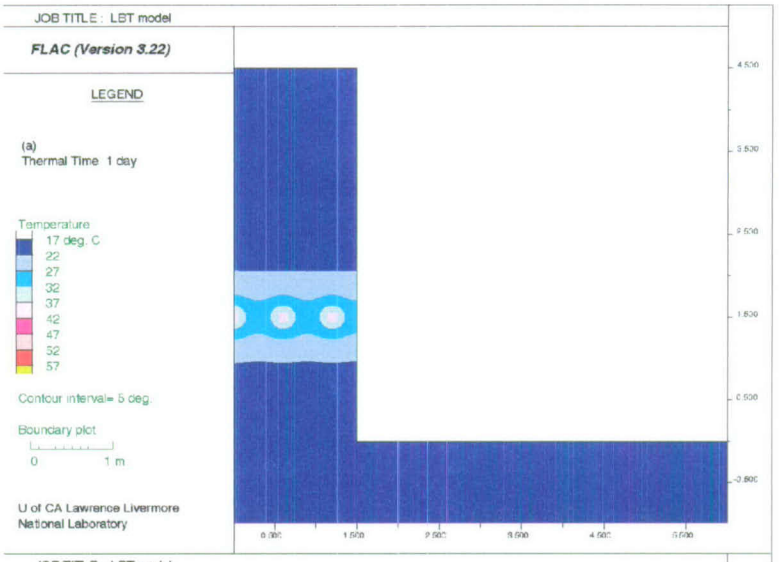
JOB TITLE : LBT model
FLAC (Version 3.22)
LEGEND
(a)
Thermal Time 1 day
Temperature
17 deg. C
22
27
32
37
42
47
52
57
Contour interval= 5 deg.
Boundary plot
0
1 m
U of CA Lawrence Livermore
National Laboratory

(b)

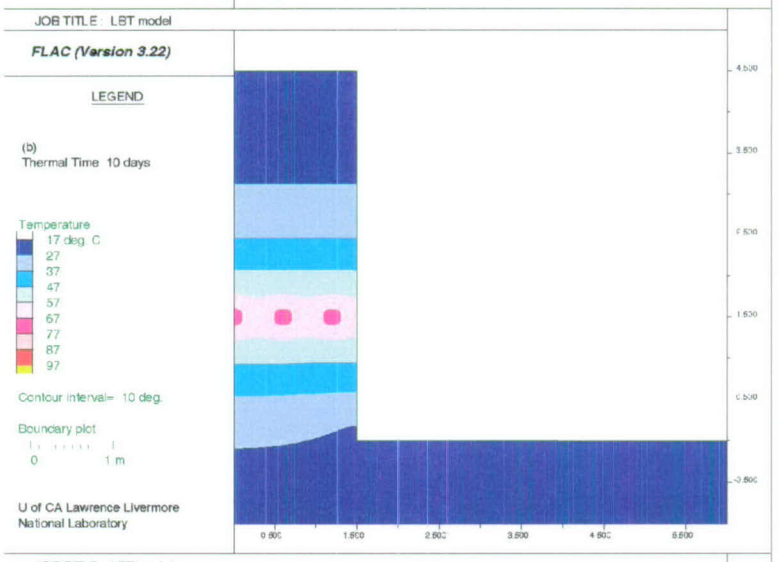
JOB TITLE : LBT model
FLAC (Version 3.22)
LEGEND
(b)
Thermal Time 10 days
Temperature
17 deg. C
27
37
47
57
67
77
87
97
Contour interval= 10 deg.
Boundary plot
0
1 m
U of CA Lawrence Livermore
National Laboratory

(c)

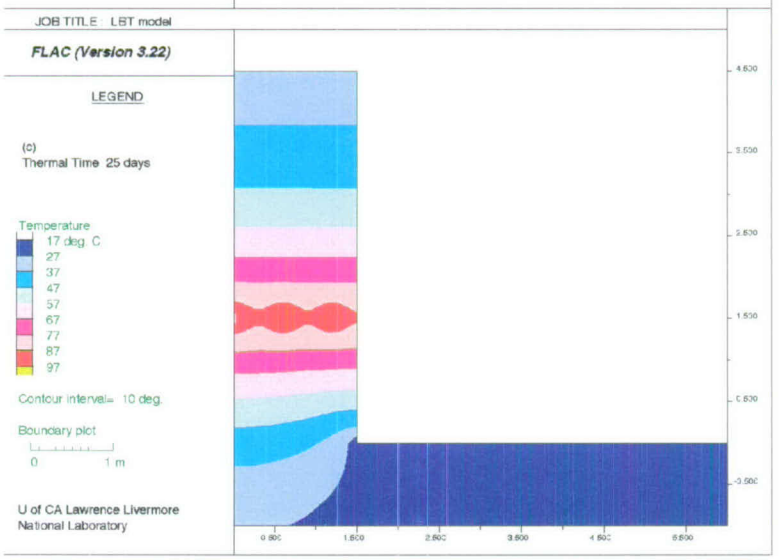
JOB TITLE : LBT model
FLAC (Version 3.22)
LEGEND
(c)
Thermal Time 25 days
Temperature
17 deg. C
27
37
47
57
67
77
87
97
Contour interval= 10 deg.
Boundary plot
0
1 m
U of CA Lawrence Livermore
National Laboratory

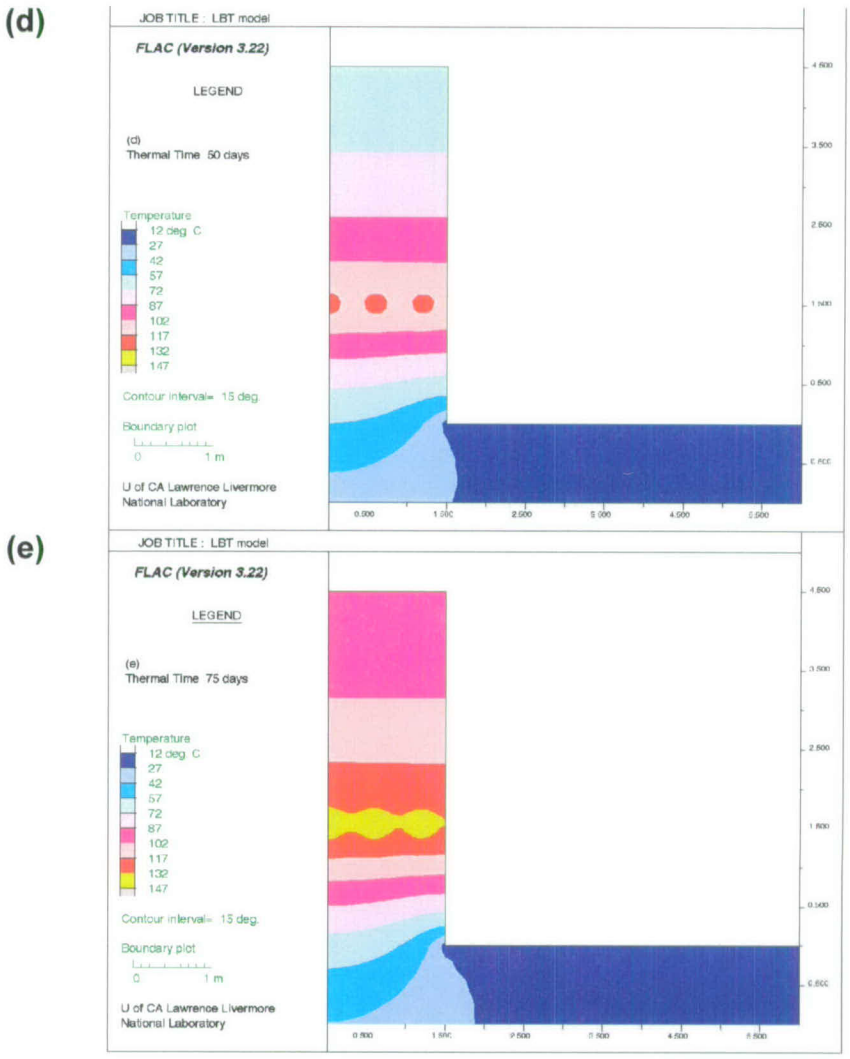

Figure 3-28. Temperature Contours in a Vertical Cross Section of the LBT After (a) 1 Day, (b) 10 Days, (c) 25 Days, (d) 50 Days, and (e) 75 Days of Heating, Calculated by FLAC Model

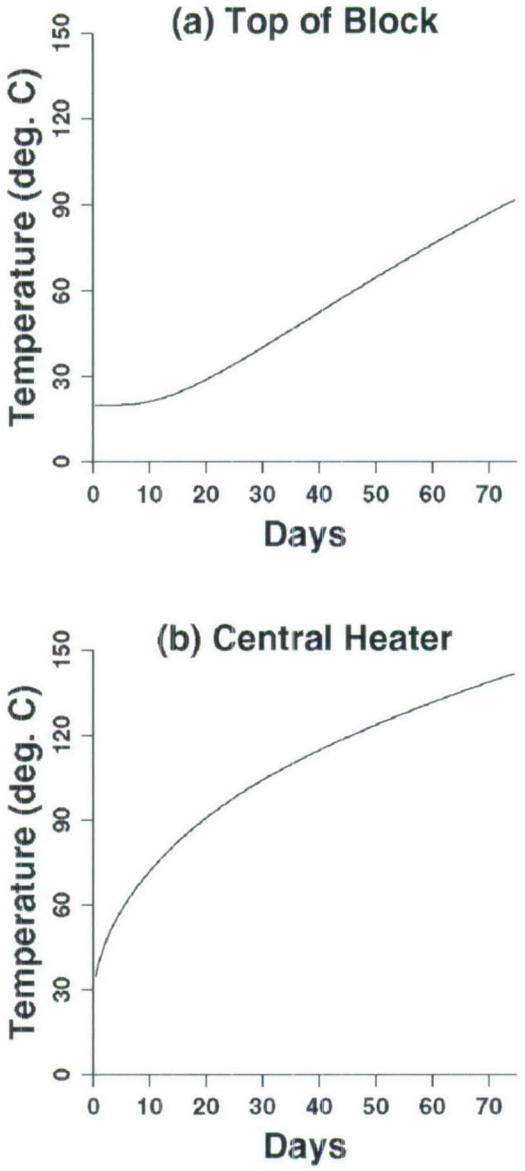

Figure 3-29. Temperature Profiles for (a) the Top and (b) Heater of the LBT, Calculated by FLAC Model

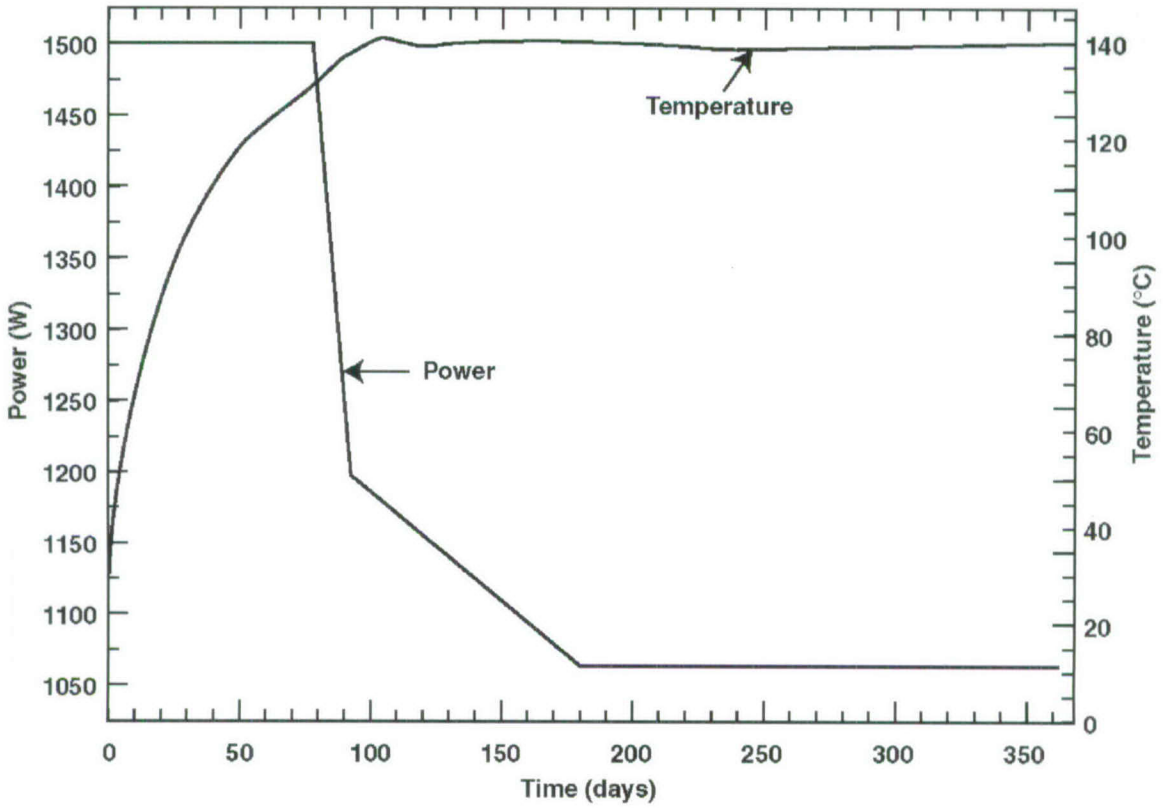

Figure 3-30. Temperature Near the Heater Horizon of the LBT Calculated by V-TOUGH Continuum Model (Lee 1995a)

(a)

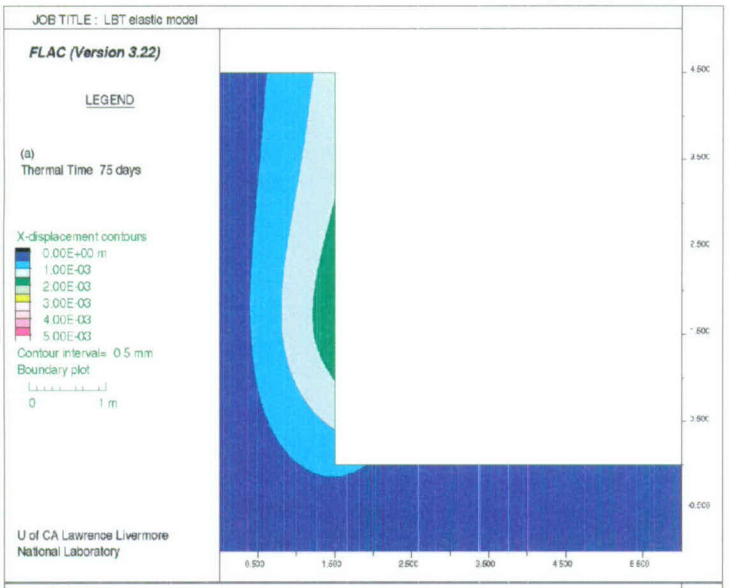
JOB TITLE : LBT elastic model
FLAC (Version 3.22)
LEGEND
(a)
Thermal Time 75 days
X-displacement contours
0.00E+00 m
1.00E-03
2.00E-03
3.00E-03
4.00E-03
5.00E-03
Contour interval= 0.5 mm
Boundary plot
0
1 m
U of CA Lawrence Livermore
National Laboratory

(b)

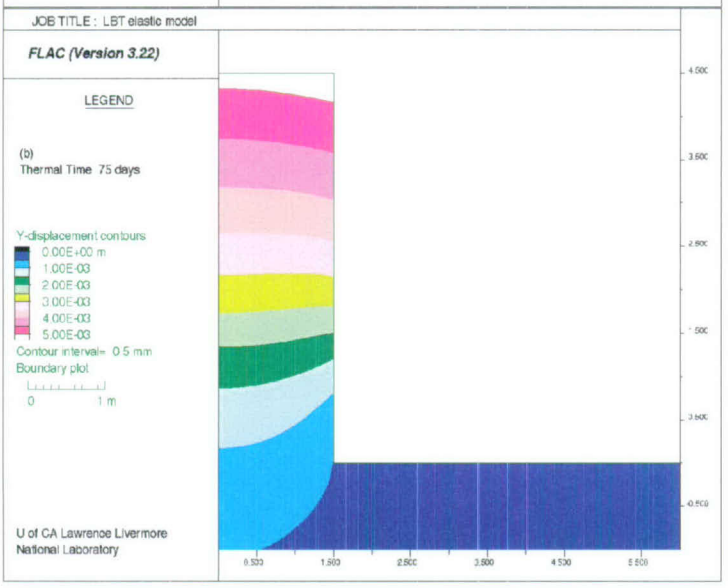
JOB TITLE : LBT elastic model
FLAC (Version 3.22)
LEGEND
(b)
Thermal Time 75 days
Y-displacement contours
0.00E+00 m
1.00E-03
2.00E-03
3.00E-03
4.00E-03
5.00E-03
Contour interval= 0.5 mm
Boundary plot
0
1 m
U of CA Lawrence Livermore
National Laboratory

(c)

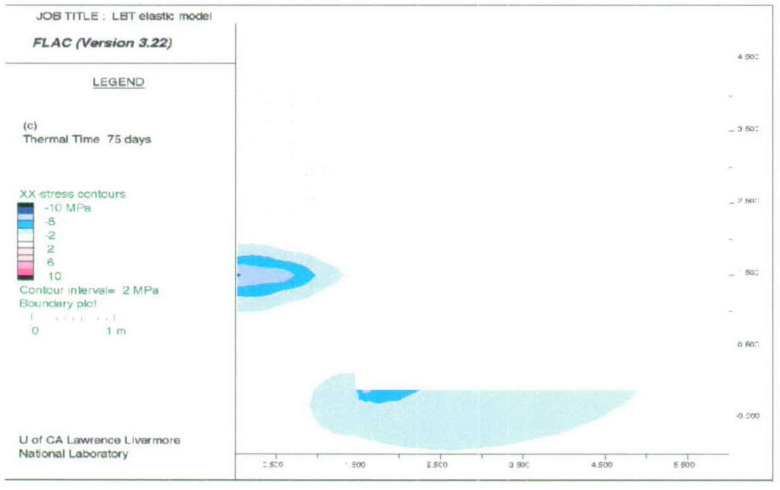
JOB TITLE : LBT elastic model
FLAC (Version 3.22)
LEGEND
(c)
Thermal Time 75 days
XX-stress contours
-10 MPa
-6
-2
2
6
10
Contour interval= 2 MPa
Boundary plot
0
1 m
U of CA Lawrence Livermore
National Laboratory

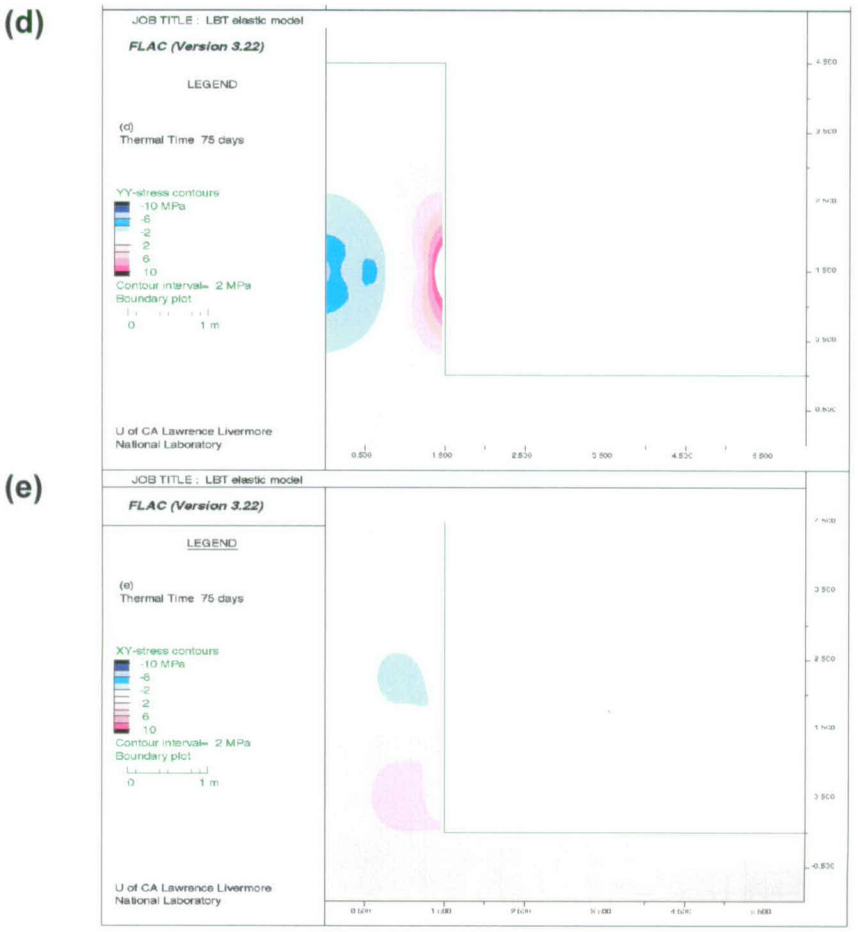

Figure 3-31. Displacements and Stresses Predicted by the First FLAC Model at 75 Days of Heating, for (a) Horizontal, x, Displacement; (b) Vertical, y, Displacement; (c) σ_{xx} Stress; (d) σ_{yy} Stress; and (e) σ_{xy} Stress

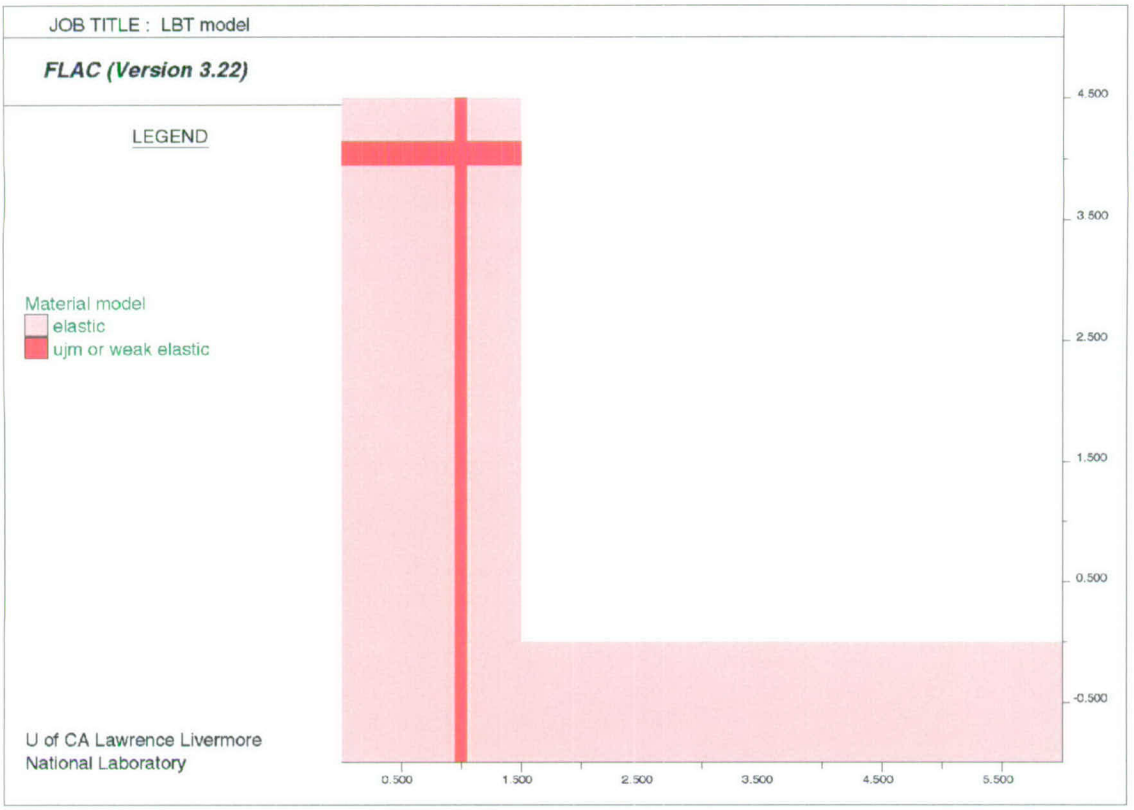

Figure 3-32. Model Configuration of the Third FLAC Model with One Horizontal Fracture and One Vertical Fracture

(a)

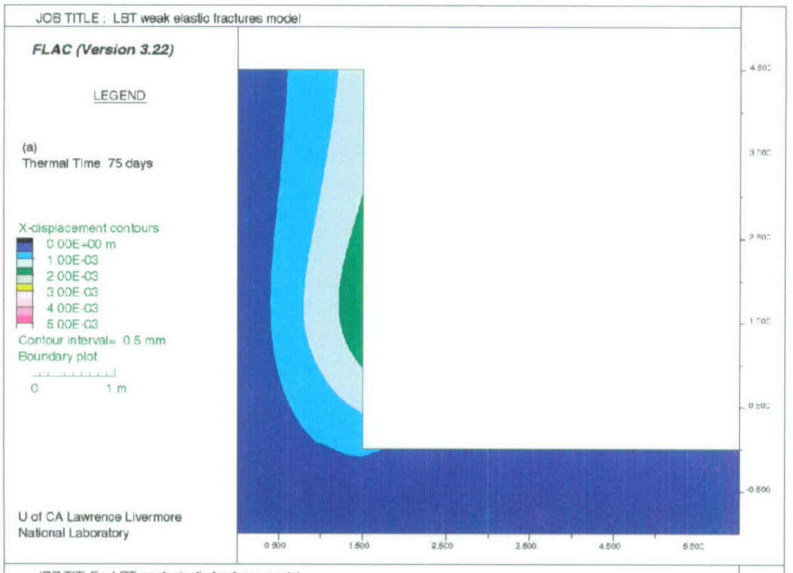
JOB TITLE : LBT weak elastic fractures model
FLAC (Version 3.22)
LEGEND
(a)
Thermal Time 75 days
X-displacement contours
0.00E+00 m
1.00E-03
2.00E-03
3.00E-03
4.00E-03
5.00E-03
Contour interval= 0.5 mm
Boundary plot
0
1 m
U of CA Lawrence Livermore
National Laboratory

(b)

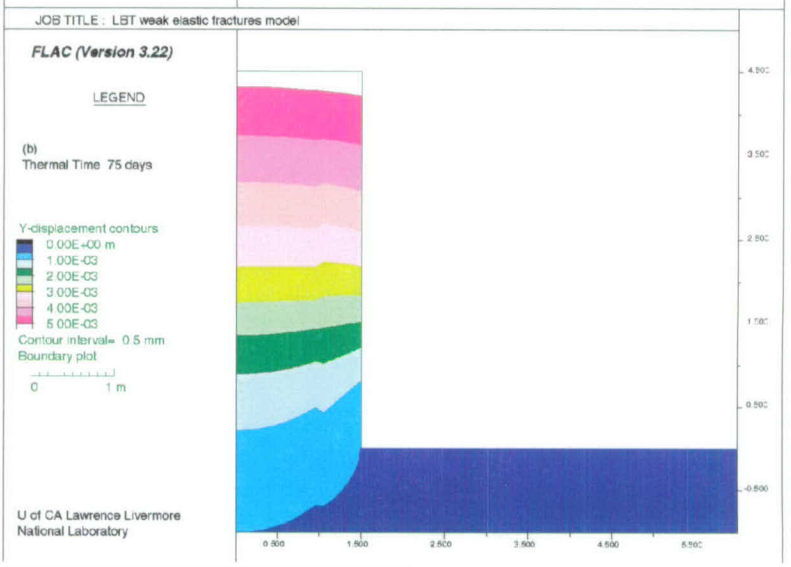
JOB TITLE : LBT weak elastic fractures model
FLAC (Version 3.22)
LEGEND
(b)
Thermal Time 75 days
Y-displacement contours
0.00E+00 m
1.00E-03
2.00E-03
3.00E-03
4.00E-03
5.00E-03
Contour interval= 0.5 mm
Boundary plot
0
1 m
U of CA Lawrence Livermore
National Laboratory

(c)

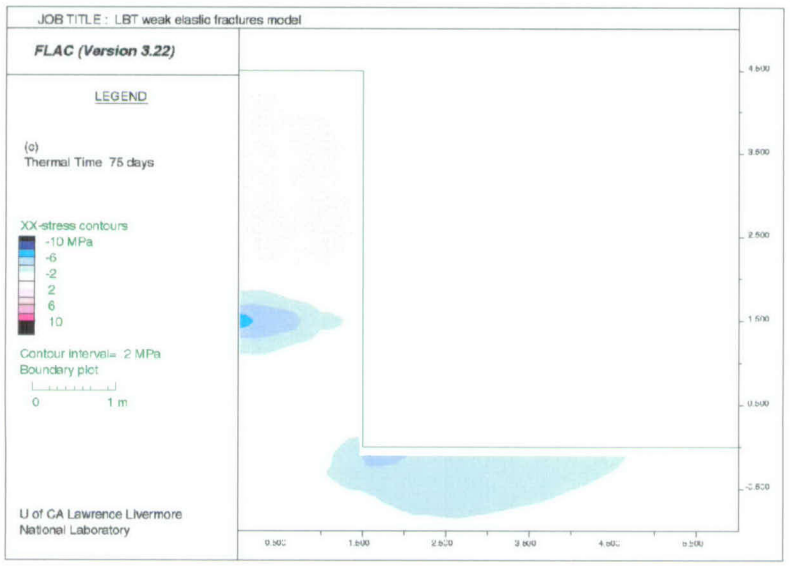
JOB TITLE : LBT weak elastic fractures model
FLAC (Version 3.22)
LEGEND
(c)
Thermal Time 75 days
XX-stress contours
-10 MPa
-6
-2
2
6
10
Contour interval= 2 MPa
Boundary plot
0
1 m
U of CA Lawrence Livermore
National Laboratory

(d)

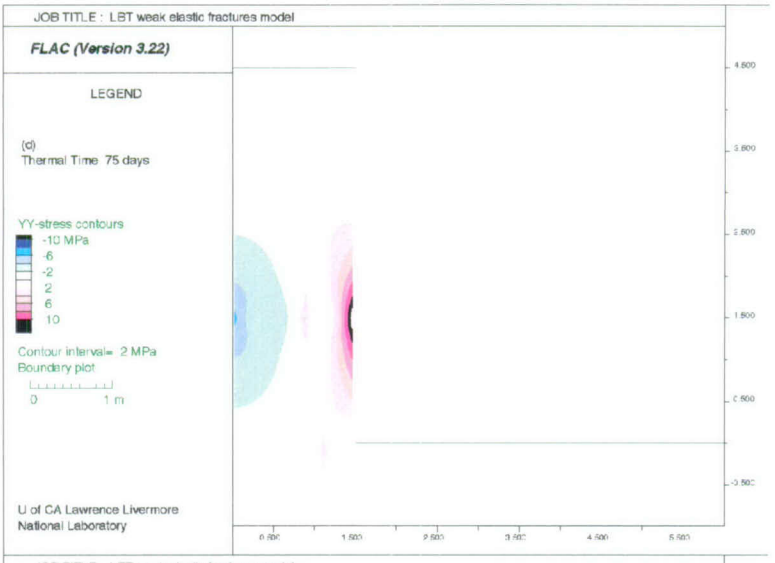

(e)

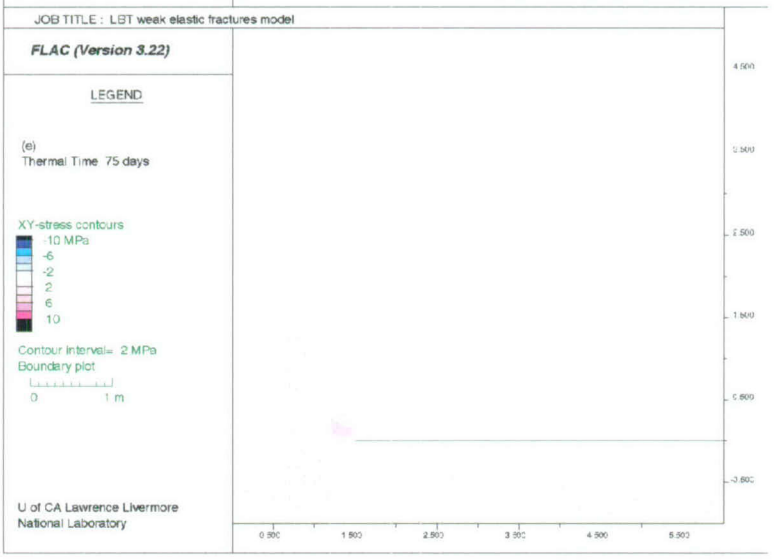

Figure 3-33. Displacements and Stresses Predicted by the Third FLAC Model of the LBT at 75 Days of Heating, (a) Horizontal, x, Displacement; (b) Vertical, y, Displacement; (c) σ_{xx} Stress; (d) σ_{yy} Stress; and (e) σ_{xy} Stress.

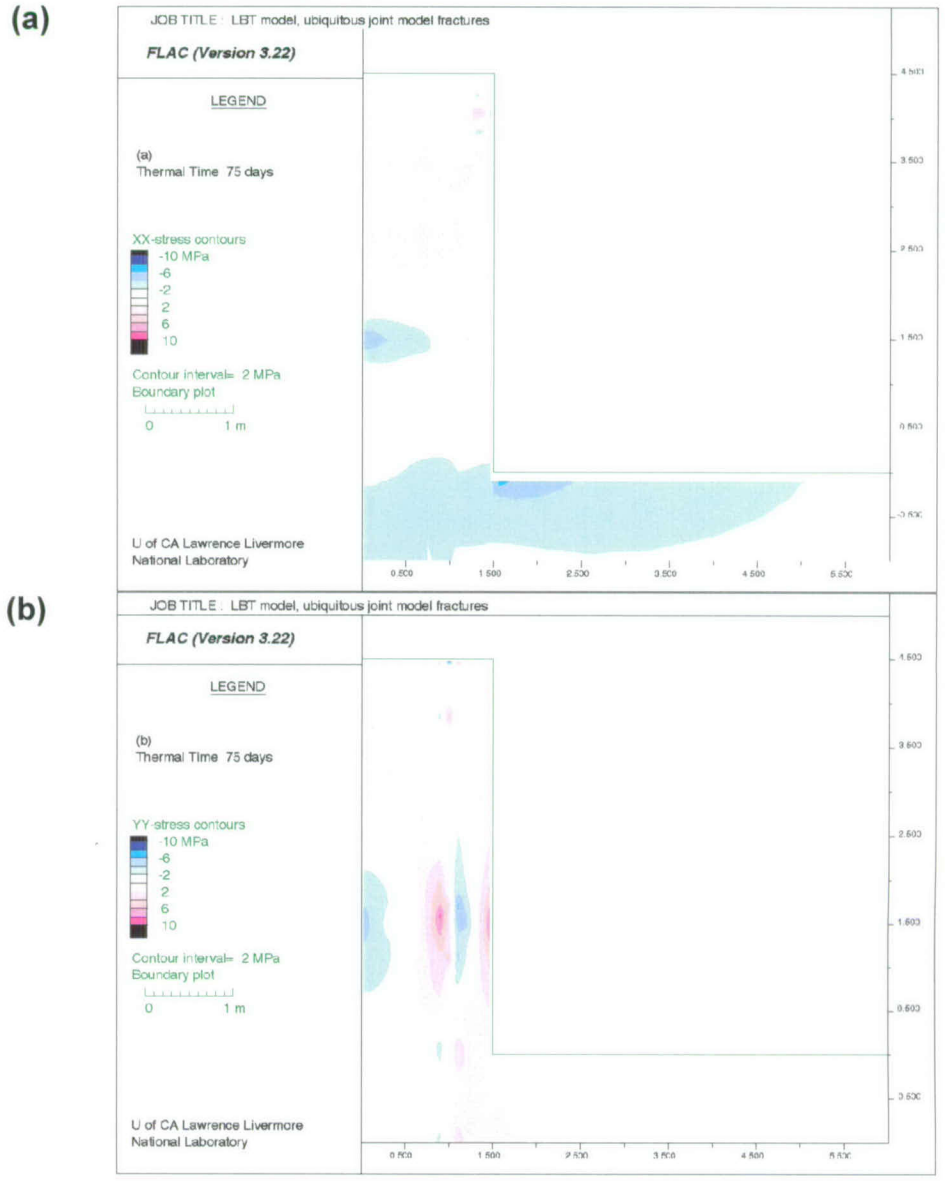

Figure 3-34. The (a) σ_{XX} and (b) σ_{YY} Contours in the LBT Predicted by the Fourth FLAC Model at 75 Days of Heating

(a)

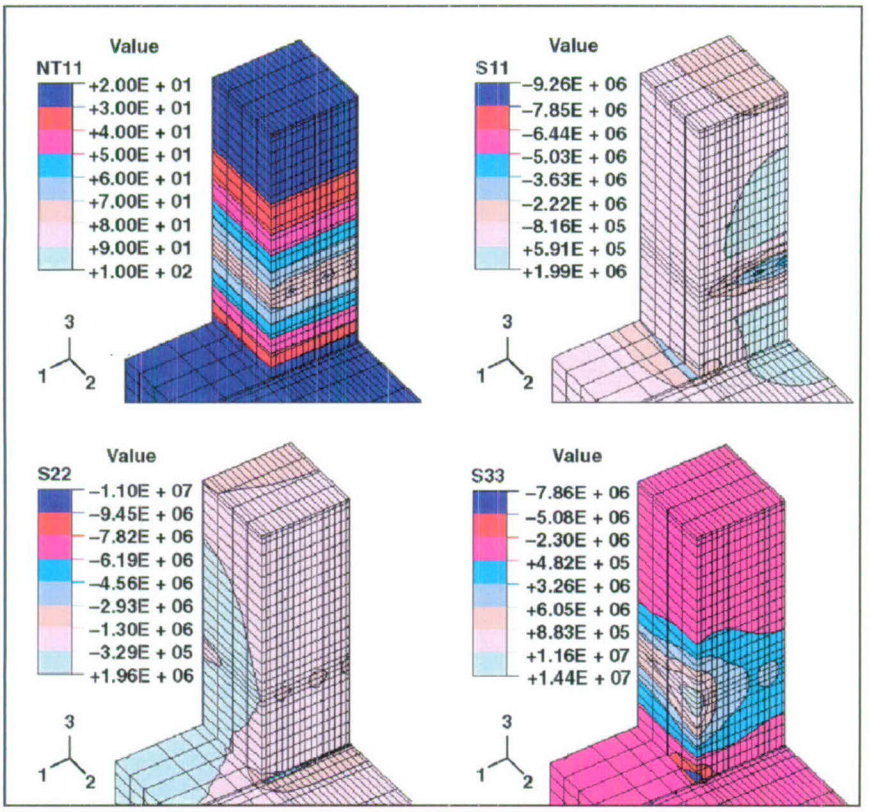
Value
NT11
+2.00E + 01
+3.00E + 01
+4.00E + 01
+5.00E + 01
+6.00E + 01
+7.00E + 01
+8.00E + 01
+9.00E + 01
+1.00E + 02
Value
S11
−9.26E + 06
−7.85E + 06
−6.44E + 06
−5.03E + 06
−3.63E + 06
−2.22E + 06
−8.16E + 05
+5.91E + 05
+1.99E + 06
Value
S22
−1.10E + 07
−9.45E + 06
−7.82E + 06
−6.19E + 06
−4.56E + 06
−2.93E + 06
−1.30E + 06
−3.29E + 05
+1.96E + 06
Value
S33
−7.86E + 06
−5.08E + 06
−2.30E + 06
+4.82E + 05
+3.26E + 06
+6.05E + 06
+8.83E + 05
+1.16E + 07
+1.44E + 07

(b)

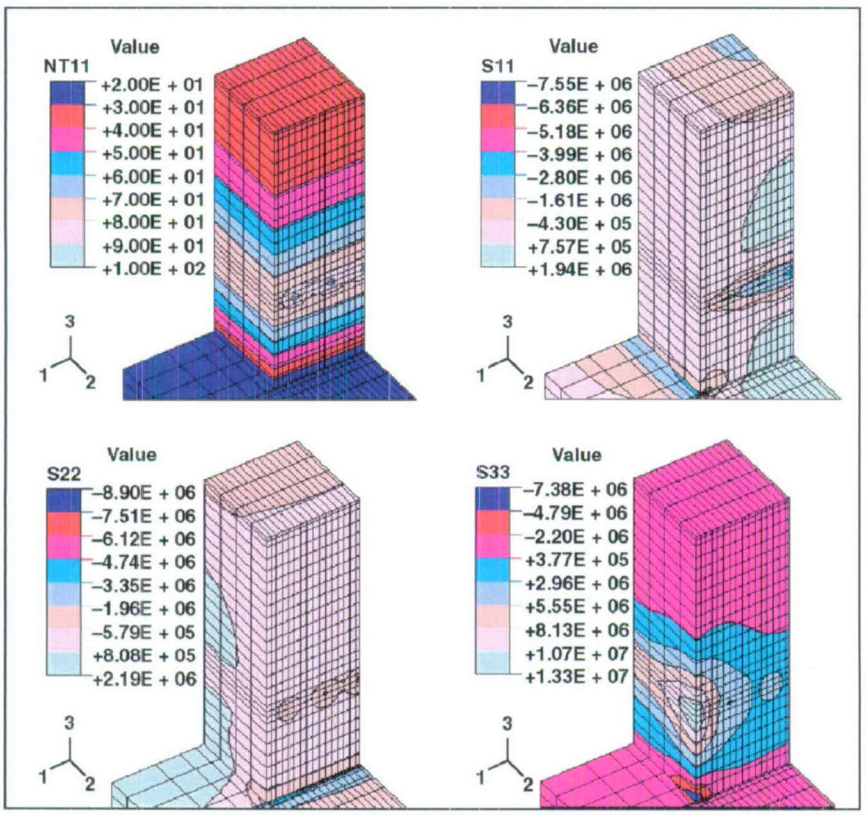
Value
NT11
+2.00E + 01
+3.00E + 01
+4.00E + 01
+5.00E + 01
+6.00E + 01
+7.00E + 01
+8.00E + 01
+9.00E + 01
+1.00E + 02
Value
S11
−7.55E + 06
−6.36E + 06
−5.18E + 06
−3.99E + 06
−2.80E + 06
−1.61E + 06
−4.30E + 05
+7.57E + 05
+1.94E + 06
Value
S22
−8.90E + 06
−7.51E + 06
−6.12E + 06
−4.74E + 06
−3.35E + 06
−1.96E + 06
−5.79E + 05
+8.08E + 05
+2.19E + 06
Value
S33
−7.38E + 06
−4.79E + 06
−2.20E + 06
+3.77E + 05
+2.96E + 06
+5.55E + 06
+8.13E + 06
+1.07E + 07
+1.33E + 07

(c)

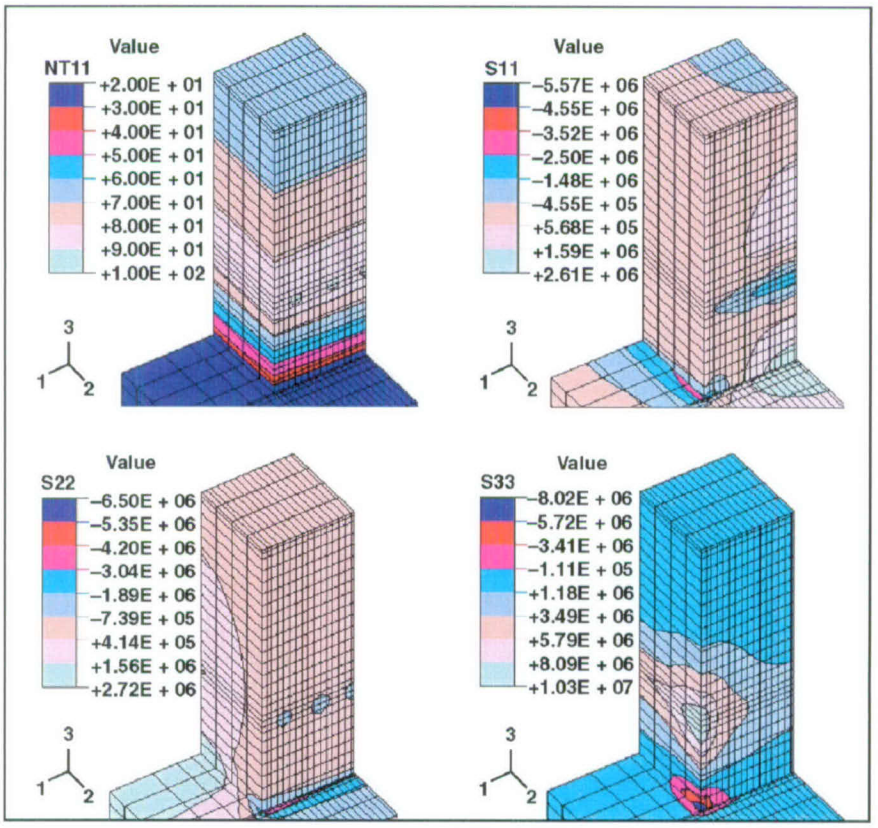

Figure 3-35. Temperature and Normal Stress Contours Predicted by ABAQUS Model at (a) 10, (b) 20, and (c) 60 Days of Heating

(a)

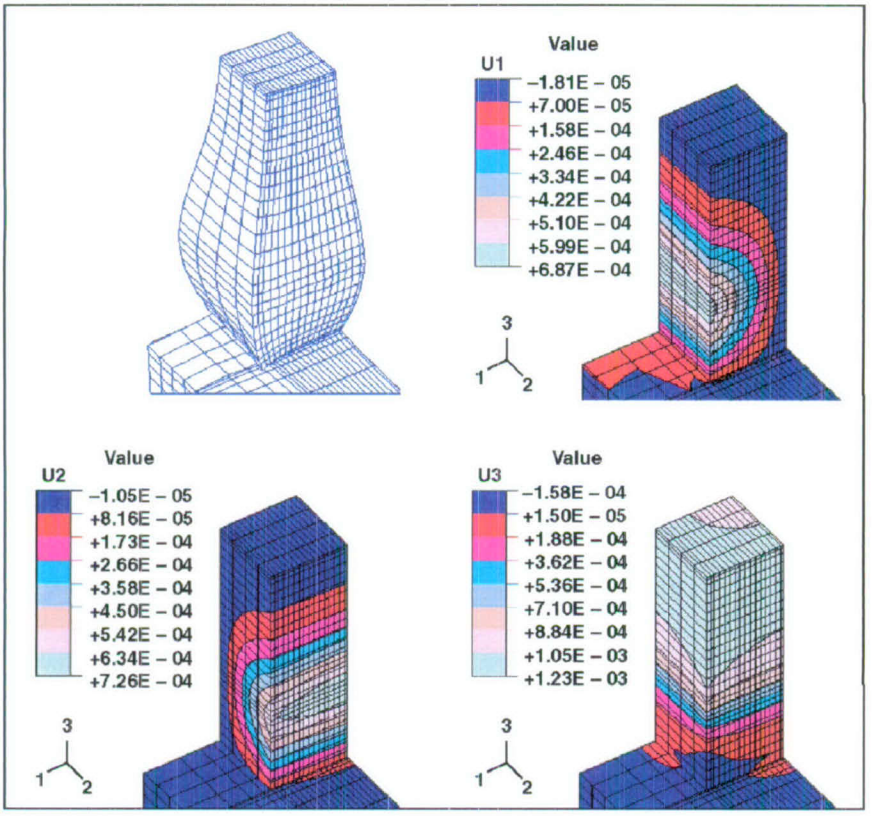
Value
U1
−1.81E − 05
+7.00E − 05
+1.58E − 04
+2.46E − 04
+3.34E − 04
+4.22E − 04
+5.10E − 04
+5.99E − 04
+6.87E − 04
3
1
2
Value
U2
−1.05E − 05
+8.16E − 05
+1.73E − 04
+2.66E − 04
+3.58E − 04
+4.50E − 04
+5.42E − 04
+6.34E − 04
+7.26E − 04
3
1
2
Value
U3
−1.58E − 04
+1.50E − 05
+1.88E − 04
+3.62E − 04
+5.36E − 04
+7.10E − 04
+8.84E − 04
+1.05E − 03
+1.23E − 03
3
1
2

(b)

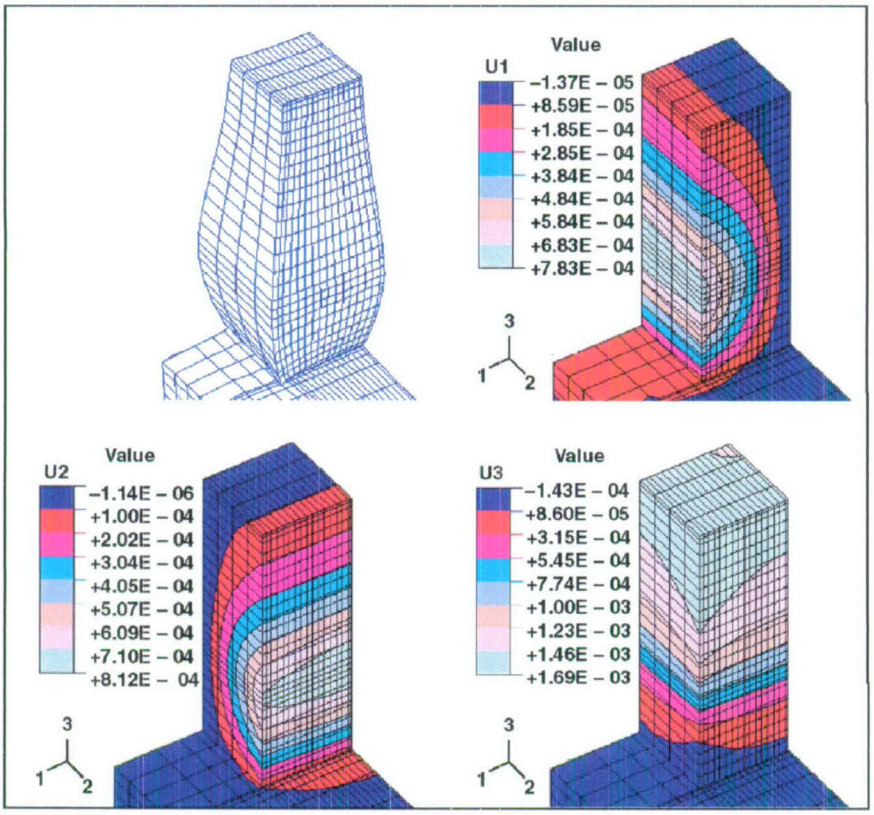
Value
U1
−1.37E − 05
+8.59E − 05
+1.85E − 04
+2.85E − 04
+3.84E − 04
+4.84E − 04
+5.84E − 04
+6.83E − 04
+7.83E − 04
3
1
2
Value
U2
−1.14E − 06
+1.00E − 04
+2.02E − 04
+3.04E − 04
+4.05E − 04
+5.07E − 04
+6.09E − 04
+7.10E − 04
+8.12E − 04
3
1
2
Value
U3
−1.43E − 04
+8.60E − 05
+3.15E − 04
+5.45E − 04
+7.74E − 04
+1.00E − 03
+1.23E − 03
+1.46E − 03
+1.69E − 03
3
1
2

(c)

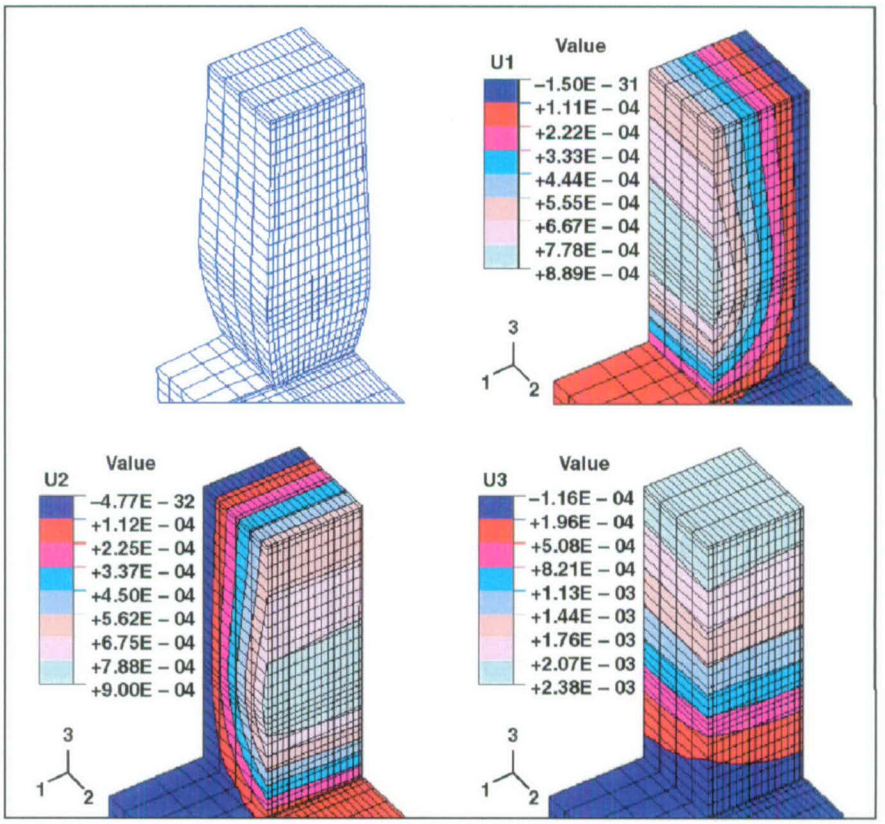

Figure 3-36. Displacements in the LBT Predicted by the ABAQUS Model at (a) 10, (b) 20, and (c) 60 Days of Heating

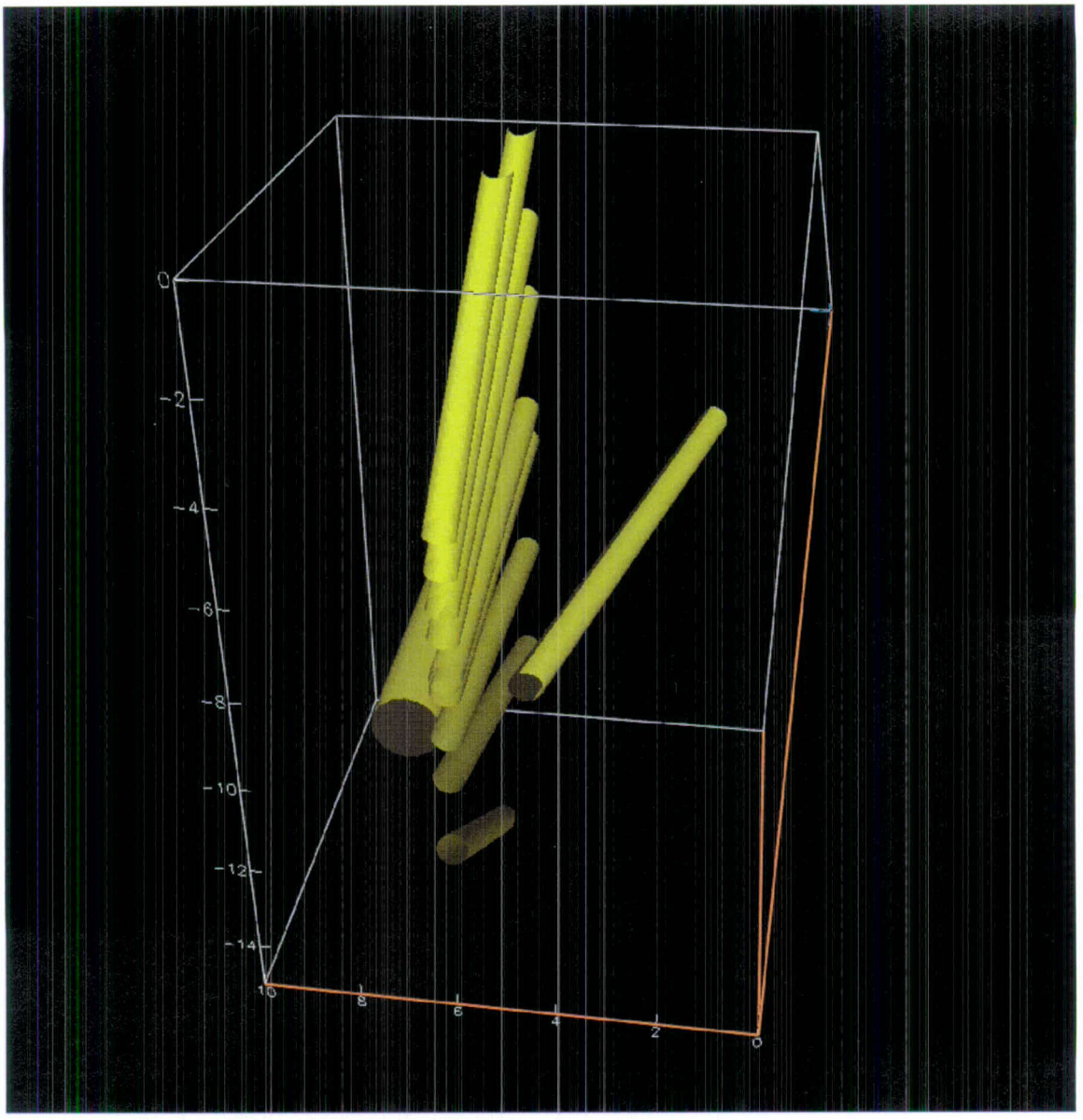

Figure 3-37. Post-test Coring Holes Drilled from the West Face of the Block

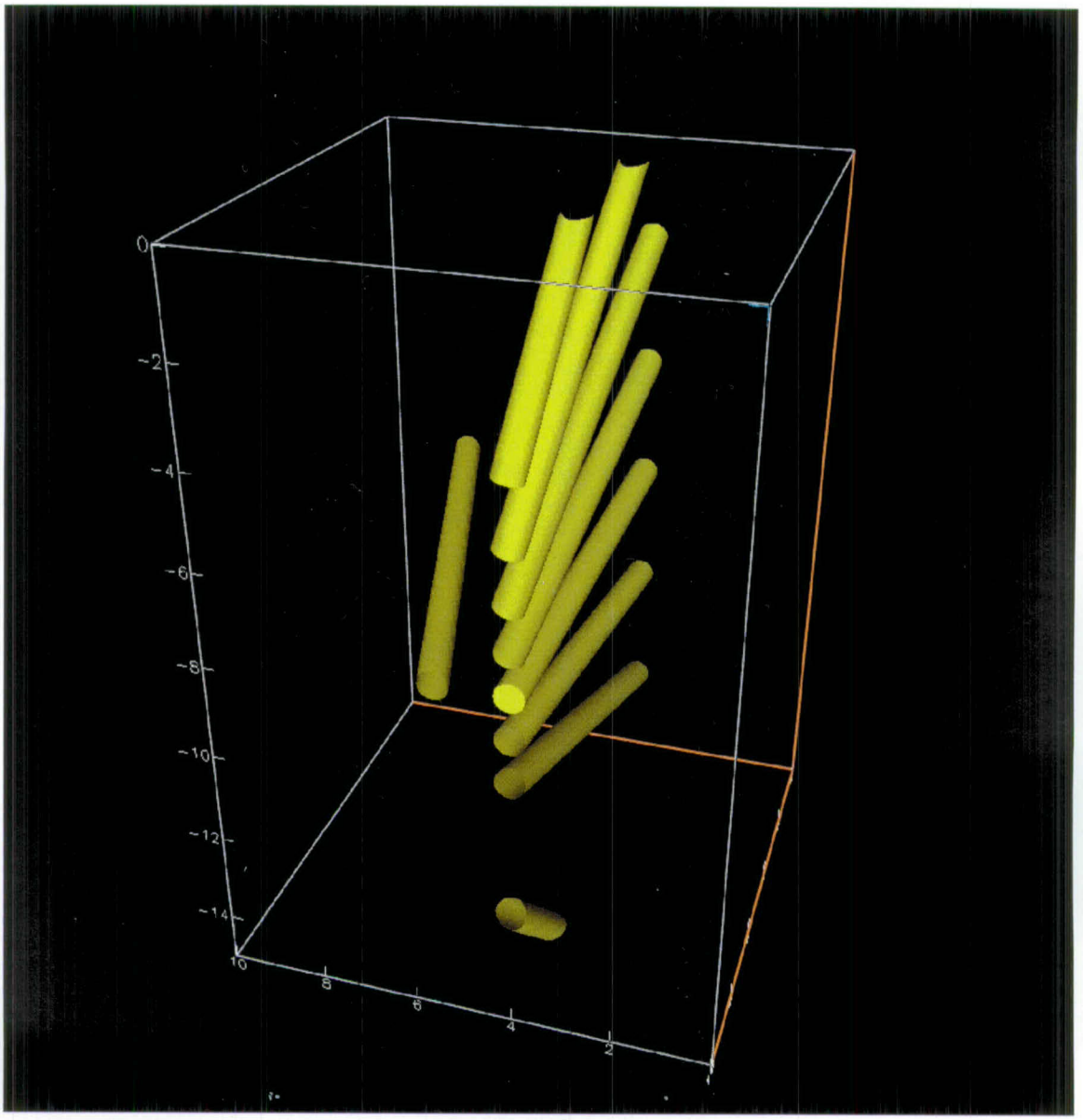

Figure 3-38. Post-test Coring Holes Drilled from the North Face of the Block